M2LW-18OR0402026

Light Water Reactor Sustainability Program

Stress Corrosion Crack Initiation and Propagation under Different Corrosion Environments and the Role of Post-Irradiation Annealing on Irradiation Assisted Stress Corrosion Crack Mitigation

August 2018

U.S. Department of Energy

Office of Nuclear Energy

Stress Corrosion Crack Initiation and Propagation under Different Corrosion Environments and the Role of Post-Irradiation Annealing on Irradiation Assisted Stress Corrosion Crack Mitigation

September 2018

Prepared for the Light Water Reactor Sustainability Program
Materials Research Pathway
Milestone Number, M2LW-18OR0402026

University of Michigan
2355 Bonisteel Blvd.
Ann Arbor, MI 48109

Gary S. Was (Principal Investigator)

Wenjun Kuang

Rajan Bhambroo

Justin Hesterberg

CONTENTS

Executive Summary

The program consists of two major tasks; determination of the factors affecting crack initiation in neutron irradiated alloys strained in high temperature water, and utilization of post-irradiation annealing as both a mitigation technique for IASCC and to identify microstructure features controlling IASCC initiation. The first task focused on improving the capability to detect crack initiation and identifying the factors affecting it. This included development of the four-point bend test to determine the stress at initiation and the role of dislocation channels in the initiation process. It also includes the assessment of alloys and environments on IASCC initiation. The second task involved the use of post-irradiation annealing to identify the microstructure features responsible for IASCC initiation. By isolating the PIA conditions that mark the disappearance of IASCC, a comparison of microstructures may provide insight as to what change is responsible for the elimination of IASCC susceptibility, and, conversely, the introduction of which features under irradiation cause the introduction of IASCC susceptibility. The outcome of this program is a firmer understanding of parameters and microstructures governing IASCC, a prescription for post-irradiation annealing to mitigate IASCC, and a foundation for development of predictive models of IASCC.

KEY FINDINGS

- The increase in the corrosion potential of the environment results in an increase in the cracking susceptibility of 304 stainless steel. At high potentials, the cracking susceptibility was determined by crack propagation since very few cracks nucleate and the nucleated cracks grew rapidly to failure. At low potentials, cracking was predominantly controlled by crack initiation resulting in high crack density but minimal crack growth.
- Depending on the fluence (dpa), dislocation channels form at stresses as low as 40% of the bulk yield stress. Cracks always nucleated at dislocation channel-grain boundary intersections either with the formation of the channel or after it. MnS inclusion on the grain boundary were often the site of crack nucleation and their dissolution in NWC is likely a key factor in producing an environment that is conducive to cracking. It was also found that increasing dpa resulted in a lower stress to both initiate dislocation channels and cracks.
- Post-irradiation annealing was found to mitigate the crack initiation susceptibility in 304L irradiated in the Barsebäck 1 BWR. With one exception, higher degrees of annealing (longer times and/or higher temperatures) resulted in a decrease in SCC susceptibility. All measures of IGSCC susceptibility (max stress, uniform strain, total strain, %IG) changed monotonically with longer times and/or temperatures.
- Hydrogen water chemistry can significantly mitigate the SCC propagation in irradiated stainless steels. The mitigating effect of HWC increases after annealing treatment, indicating that it is dependent on the inherent SCC susceptibility of material. The post-irradiation treatment has a significant mitigating effect on the SCC propagation of this material with a larger effect in HWC. It seems that the annealing treatments have larger mitigating effects on crack initiation than on crack growth in NWC. The reduced SCC susceptibility of the annealed sample is consistent with the recovery of the irradiated microstructure (dislocation loop, solute cluster and grain boundary segregation).

1 INTRODUCTION

Objectives and scope

This program addresses the cause of IASCC in LWR core internals in BWR normal water chemistry, hydrogen water chemistry and PWR primary water, with the objective of providing a foundation for materials performance models and mitigation strategies by determining the key factors controlling the process. Irradiation assisted stress corrosion cracking (IASCC) continues to cause failures in key components of both PWRs and BWRs in the US and in international reactor fleets. Identified in the 1960s, IASCC is generic in that all water reactors have exhibited susceptibility over a wide range of alloys and components. The problem will gain increasing importance in the coming years due to two factors; 1) the need for life extension to 60 years and perhaps to 80 years for the existing reactor fleet, and 2) the introduction of advanced reactors that will be subjected to the same types of environments.

The program consists of two major tasks; determination of the factors affecting crack initiation in irradiated alloys strained in high temperature water, and utilizing post-irradiation annealing as a mitigation technique for IASCC and as a means to identify microstructure features controlling IASCC initiation. The first task focused on improving the capability to detect crack initiation and identifying the factors affecting it. This included development of the four-point bend test to determine the stress at initiation and the role of dislocation channels in the initiation process. It also included the assessment of alloy and environment on IASCC initiation. The second part involved the use of post-irradiation annealing to narrow in on the microstructure features responsible for IASCC initiation. By isolating the PIA condition that marks the disappearance of IASCC, a comparison of microstructures may provide some insight as to what change is responsible for the elimination of IASCC susceptibility. The outcome of this program is a firmer understanding of parameters and microstructures governing IASCC and a prescription for post-irradiation annealing that mitigates IASCC.

It is challenging to establish the capability of testing neutron-irradiated samples (especially for crack growth rate (CGR) tests) under laboratory conditions. A procedure for loading and spot welding round compact tension (RCT) sample in hot cell has been established prior to the commencement of this program was further improved. A new test system (IM5) equipped with a AT5 based direct current potential drop (DCPD) system was developed at UM for testing neutron-irradiated samples in a hot cell. In order to test the capability to measure crack growth rates in a hot cell, a CGR test on cold worked stainless steel (SS) was performed according to the procedures for irradiated sample testing. At the same time, another sample from the same heat was tested with an in-house DCPD system based on LabView software to benchmark against the AT5 system. The benchmarking effort was successful in that nearly identical results were produced in the two comparison experiments.

The role of various alloying elements and microstructural features on the crack initiation in austenitic stainless steels in reactor environment under the presence of radiation is not properly understood. To address this issue, a four-point bend test setup was used to evaluate the role of various microstructural features. The system configuration was modified to improve the reliability of the system by aligning the loading fixture with the central loading axis of the system. This modification produced an improvement in the stability of the cross-head, providing more reliable sample displacement results based on the crosshead LVDT deflections. The correlation between the strain and the plastic deflection induced in the material during straining was then established.

2 EXPERIMENT

2.1 *Materials and specimens*

2.1.1 304L from the Barsebäck 1 BWR

The neutron-irradiated samples were machined from control rod #1690 which was used in the operation of the Barsebäck 1 BWR in Sweden and withdrawn from the core for the entirety of its use. The control rod was manufactured by ASEA-ATOM (now Westinghouse Electric Sweden AB) from 304L SS supplied by Vereinigte Edelstahlwerke AG. The control rod was delivered to the plant with the stainless steel in the nominally solution-annealed condition. No other heat treatments were performed during the fabrication of the control rod. The chemical composition of the material (in wt.%) was determined both by ladle analysis of the un-irradiated material during fabrication [1] and by an APT characterization of the irradiated material [2], as shown in Table 2-1. The two chemical compositions are quite comparable with the exception of impurity traces of both Al and Cu as seen in APT.

Table 2-1: Chemical compositions of the 304L SS in both un-irradiated and irradiated conditions.

Method	C	Si	Mn	Cr	Co	N	Ni	P	S	B	Al	Cu	Fe
Ladle Analysis (Unirradiated)	0.025	0.30	1.09	18.35	0.029	0.024	10.57	0.013	0.003	<0.0005	-	-	Bal.
APT (Irradiated)	0.035	0.40	1.13	18.34	0.15	-	11.6	0.02	0.001	ND	0.02	0.12	68.01

The mechanical properties of the un-irradiated material had been determined previously [1] via tensile experiments at both room temperature and 300°C. Several tests were completed at each temperature for which the results are shown in Table 2-2.

Table 2-2: Results of tensile tests performed on un-irradiated 304L SS at both room temperature and 300 °C [1].

Tensile Test Number	Room Temperature				300°C			
	YS (MPa)	UTS (MPa)	ε_{tot} (%)	Z (1) (%)	YS (MPa)	UTS (MPa)	ε_{tot} (%)	Z (1) (%)
191	215	509	65	80	-	-	-	-
360	215	509	65	82	179	380	35	75
361	208	502	65	82	159	380	49	75
362	209	502	70	82	-	-	-	-
Mean	212	506	66	82	169	380	42	75

(1) Reduction of area.

A summary of the irradiation history of the control rod is shown in Table 2-3 [1]. As it was withdrawn from the core for the entirety of its use, it was exposed to a lower neutron irradiation flux than would be expected for a control rod that had been used in service. The total damage accumulated is 5.9 dpa [1].

Table 2-3: Summary of the irradiation damage for control rod #1690 [1].

Control Rod ID#.	Time (hrs.)	Flux (n/cm^2s) (E> 1 MeV)	Fluence (n/cm^2) (E> 1 MeV)	Dose (dpa)
1690	95608	1.2×10^{13}	4.16×10^{21}	5.9

Two tensile samples machined from this control rod had been previously tensile tested in air at 288 °C [1]. The results from the tensile tests are summarized in Table 2-4. The results showed significant radiation hardening in comparison to the results from the un-irradiated samples (Table 2-2).

Table 2-4: Results of tensile tests performed in air at 288 °C on the irradiated material from control rod# 1690 [1].

Test #	YS (MPa)	UTS (MPa)	ε_{tot} (%)	ε_u (%)
1	662	662	11.3	0.04
2	683	683	11.2	0.03
Mean	672	672	11.2	0.03

2.1.1.1 Inventory of tensile bars and RCT samples

Studsvik Nuclear AB provided documentation detailing the fabrication of the irradiated specimens. A total of 5 RCT and 12 tensile samples were delivered, as well as an additional 18 smaller blanks which were left over from the fabrication of the other specimens. The samples were machined from the control rod blade as shown in Figure 2-1 [3]. The dimensions, shown in Figure 2-2a, were checked for every sample and are listed in Table 2-5 [3]. RCT1 has a small notch at the back due to the limited source material and the machining of sample T3. However, this defect was not expected to affect the stress intensity at the crack tip, thus the sample was still considered useable. The tensile samples were machined in accordance with the initial design, shown in Figure 2-2b and the measured dimensions are listed in Table 2-6. Although 10 tensile samples were originally ordered, 12 were included in the shipment, as T-1 and T-3 were machined incorrectly, i.e. they had misaligned flats along the gauge sections. It was also noticed that three samples had different sized flats, resulting from improper centering of the specimen during machining. T-5 was machined such that it only had a single large flat and it was also found to be slightly bent. In summary, of twelve tensile samples that were shipped, six were machined per specifications, three had flats which were not properly centered, two had misaligned flats, and one was slightly bent.

Prior to the annealing treatment of the designated tensile specimens, it was necessary to complete several cutting operations on the heads of the tensile specimens. The goal of these cutting operations was two-fold: first, the cutting removes ~50% of the specimen mass, thereby reducing the total dose rate; second, the cutting operation creates several small specimen slices that can be used to analyze the pre- and post-annealed hardness of the tensile specimens.

Annealing treatments were conducted in an air furnace at varying times and temperatures: 450 – 600^{o}C for 1- 20 hrs. A total of twelve unique annealing conditions were performed, as well as two repeated conditions: 500^{o}C:1hr and 600^{o}C:5hr, to verify the consistency of the annealing treatment. The furnace used for the annealing treatments demonstrated a high temperature stability and there was a good agreement between the built-in and secondary thermocouples. The specimens were all removed from the furnace at ±2 min of their target annealing times. Tables 2-5 and 2-6 outline the entire list of irradiated specimens that were utilized for this project as well as their applied annealing treatments. Note that tensile specimen T-2 was not shipped as it was damaged during the production of the specimen, while T-3 was irreparably damaged during cutting the tensile heads from the specimens. Specimen T-8 remains as a back-up specimen in case a problem develops with one of the selected specimens.

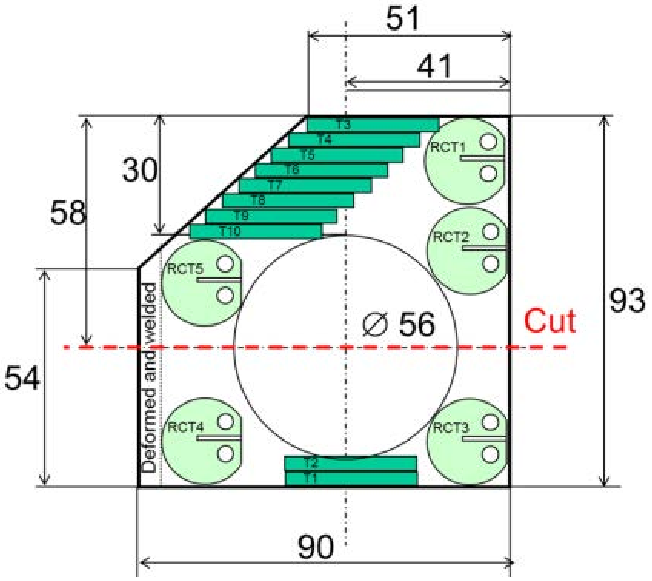

Figure 2-1: Schematic showing the locations of various samples in the control rod blade [3].

Table 2-5: Annealing conditions and dimensions of the RCT samples [3].

Sample ID	Annealing condition	W	C	a	B	B_n	b_1 b_2	D_1 D_2	h_1 h_2	H_1 H_2	H_3 H_4
RCT-1	500°C 1 h	16.30	19.89	6.83	8.08	7.19	0.47 0.35	4.04 4.01	4.51 4.27	10.87 10.81	10.78 10.90
RCT-2	As-irradiated	16.14	20.03	6.43	8.05	7.36	0.43 0.32	4.06 4.13	4.43 4.38	11.19 10.45	11.23 10.42
RCT-3	550°C 20 h	16.10	19.99	6.52	8.06	7.30	0.26 0.55	4.09 4.15	4.39 4.27	10.82 10.79	10.72 10.90
RCT-4	550°C 5 h	16.03	20.02	6.33	8.05	7.31	0.37 0.40	4.15 4.04	4.33 4.47	10.75 10.92	10.72 10.97
RCT-5	550°C 1 h	16.00	19.96	6.44	8.10	7.24	0.55 0.27	4.04 4.15	4.59 4.29	10.74 10.84	10.73 10.85

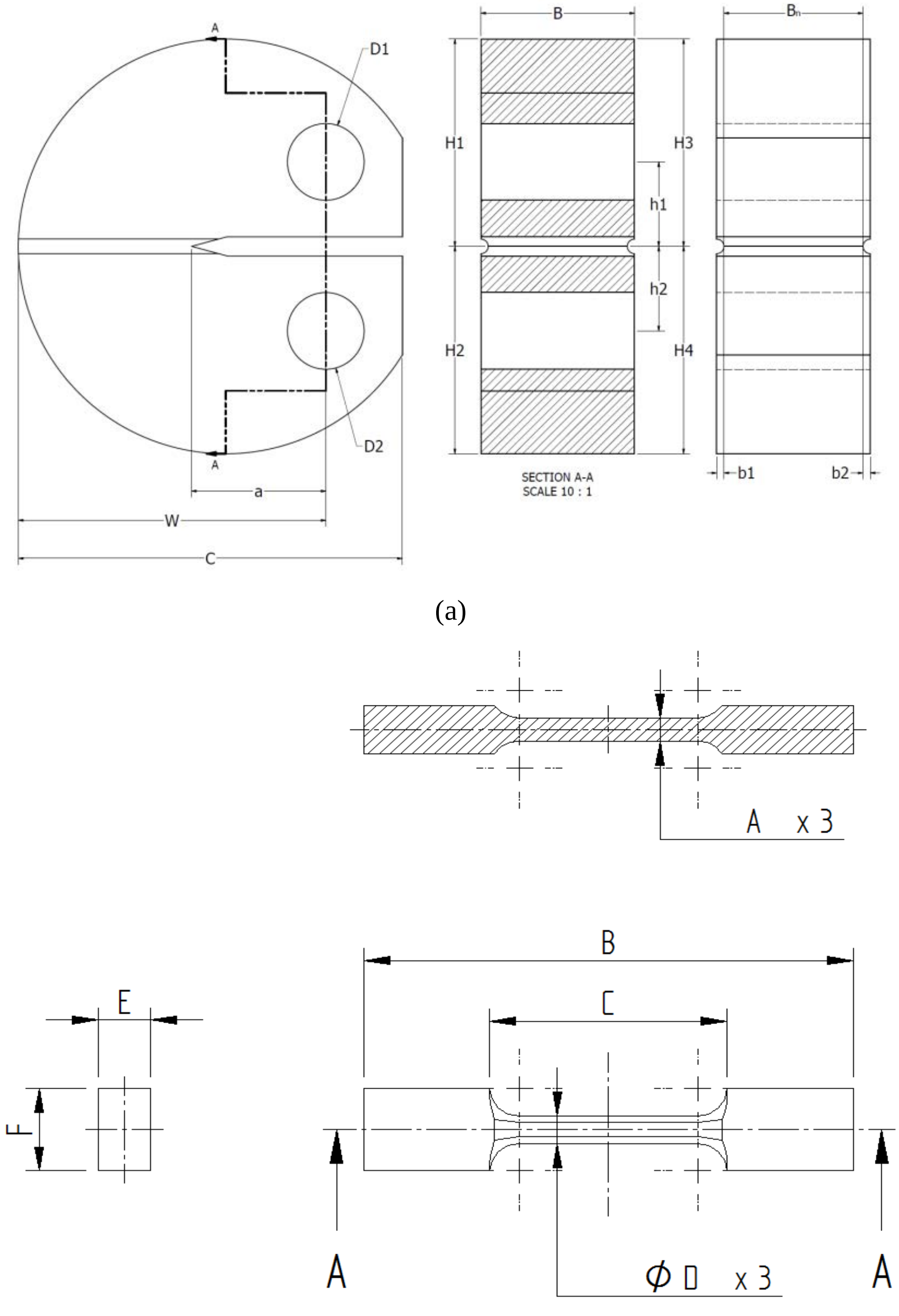

(a)

(b)

Figure 2-2: Schematic showing the dimensions checked on (a) the RCT sample and (b) the tensile bar [3].

Table 2-6: Annealing conditions and measured dimensions of the tensile bars and sample blanks [3].

<table>
<tr><td colspan="8">Tensile bars and dimensions</td></tr>
<tr><td>Sample ID</td><td>Annealing condition</td><td>A</td><td>B</td><td>C</td><td>D</td><td>E</td><td>F</td></tr>
<tr><td>T1</td><td>500^{o}C 1 h</td><td>1.63</td><td>33.07</td><td>16.16</td><td>2.00</td><td>3.51</td><td>5.96</td></tr>
<tr><td>T3</td><td>Unusable</td><td>1.44</td><td>33.06</td><td>16.11</td><td>1.90</td><td>3.47</td><td>6.01</td></tr>
<tr><td>T4</td><td>As-Irradiated</td><td>1.68</td><td>33.03</td><td>15.97</td><td>2.02</td><td>3.49</td><td>5.99</td></tr>
<tr><td>T5</td><td>500^{o}C: 1hr</td><td>1.66</td><td>33.06</td><td>16.08</td><td>1.99</td><td>3.49</td><td>6.00</td></tr>
<tr><td>T6</td><td>As-Irradiated</td><td>1.70</td><td>33.16</td><td>16.03</td><td>2.03</td><td>3.49</td><td>6.02</td></tr>
<tr><td>T7</td><td>550^{o}C: 5hr</td><td>1.69</td><td>33.16</td><td>16.03</td><td>2.0</td><td>3.51</td><td>6.01</td></tr>
<tr><td>T8</td><td>As-Irradiated</td><td>1.69</td><td>33.19</td><td>16.08</td><td>1.93</td><td>3.49</td><td>6.01</td></tr>
<tr><td>T9</td><td>550^{o}C: 20hr</td><td>1.71</td><td>33.18</td><td>16.4</td><td>1.93</td><td>3.50</td><td>5.99</td></tr>
<tr><td>T10</td><td>550^{o}C: 5hr</td><td>1.69</td><td>33.26</td><td>16.06</td><td>1.94</td><td>3.49</td><td>5.99</td></tr>
<tr><td>T11</td><td>550^{o}C: 1hr</td><td>1.71</td><td>33.03</td><td>16.11</td><td>1.92</td><td>3.56</td><td>5.96</td></tr>
<tr><td>T12</td><td>550^{o}C: 20hr</td><td>1.72</td><td>33.07</td><td>16.09</td><td>1.93</td><td>3.49</td><td>5.99</td></tr>
<tr><td>T13</td><td>550^{o}C: 1hr</td><td>1.71</td><td>33.05</td><td>16.07</td><td>1.93</td><td>3.45</td><td>6.01</td></tr>
<tr><td colspan="8">Sample blanks (various shapes and sizes)</td></tr>
<tr><td>5</td><td colspan="7">500^{o}C: 1hr</td></tr>
<tr><td>5A</td><td colspan="7">450^{o}C: 20hr</td></tr>
<tr><td>9</td><td colspan="7">450^{o}C: 5hr</td></tr>
<tr><td>9A</td><td colspan="7">450^{o}C: 1hr</td></tr>
<tr><td>11</td><td colspan="7">550^{o}C: 1hr</td></tr>
<tr><td>11A</td><td colspan="7">600^{o}C: 20hr</td></tr>
<tr><td>15</td><td colspan="7">550^{o}C: 5hr</td></tr>
<tr><td>15A</td><td colspan="7">550^{o}C: 20hr</td></tr>
<tr><td>16</td><td colspan="7">500^{o}C: 20hr</td></tr>
<tr><td>16A</td><td colspan="7">600^{o}C: 5hr</td></tr>
<tr><td>17</td><td colspan="7">600^{o}C: 1hr</td></tr>
<tr><td>17A</td><td colspan="7">600^{o}C: 5hr</td></tr>
<tr><td>18</td><td colspan="7">500^{o}C: 1hr</td></tr>
<tr><td>18A</td><td colspan="7">500^{o}C: 5hr</td></tr>
</table>

2.1.1.2 Specimen Details for Cooperative IASCC Research (CIR) Tensile Bars

The specimens for the tensile bars obtained from the EPRI CIR Program materials were in the dog bone type tensile bar specimen geometry shown in Figure 2-3 below. Specimens were part of the batch of materials fabricated at Pacific Northwest National Laboratory (PNNL) prior to irradiation in the BOR-60 reactor at Dimitrovgrad, Russia. Each sample has a cylindrical gage section with a 2 mm diameter and 12 mm gage length. All the specimens were shoulder loaded during the CERT experiments so the pin hole of 3.1 mm diameter was inconsequential to the testing of the specimen. Shoulder loading was done to avoid premature IASCC crack initiation in the vicinity of these pin holes.

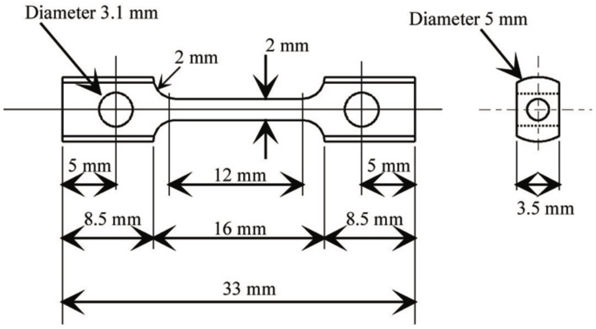

Figure 2-3: Tensile bar sample geometry and dimensions.

Irradiations were performed in liquid sodium fast reactor (BOR-60) at a temperature of 320 °C and were completed between 2001 and 2004. A neutron flux of ~1.8×10^{15} n/cm^{2}s (E>0.1 MeV), which corresponds to a damage rate of 9.4×10^{-7} dpa/s using the NRT model was used for the irradiations [4]. Total irradiation doses for the different alloying elements were between 4.4 and 47.5 dpa. Specimen designations along with the damage in the material are shown in Table 2-7 below along with the environment they were CERT tested in the laboratory. Subsequent to the irradiations, the tensile bars were shipped to Oak Ridge National Laboratory (ORNL) where the subsequent specimen preparation was performed.

Each sample was both mechanically and electrochemically polished at the ORNL Low Activity Materials Development and Analysis (LAMDA) Laboratory. Mechanical polishing was performed manually using 320 grit SiC sandpaper to remove sodium and surface contaminants left by the reactor coolant during irradiation. Each sample was then electropolished using the A2 solution supplied by Struers™ (percentages by volume: 73% ethanol, 10% ethylene glycol monobutyl ether, 9% distilled water, and 8% perchloric acid), cooled to below 20°C in an ice-bath. A potential of 30 V was applied for four 15 second periods per sample to achieve a mirror finish. The finished tensile bars were then shipped to University of Michigan (UM) for crack initiation testing using the CERT systems.

Table 2-7: Irradiated tensile bar doses and test environments.

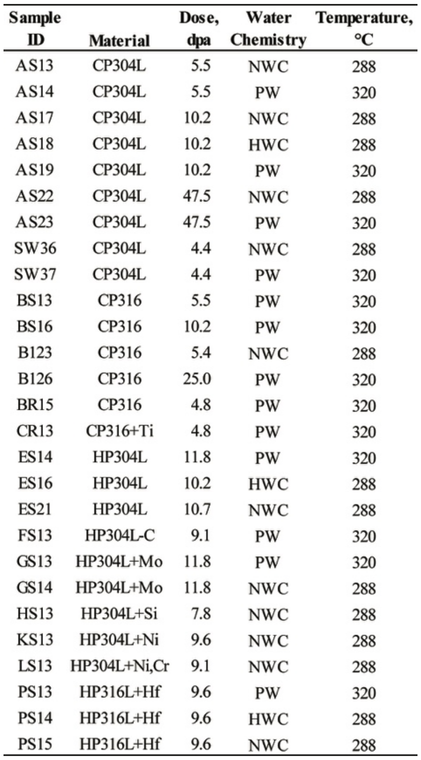

Sample ID	Material	Dose, dpa	Water Chemistry	Temperature, °C
AS13	CP304L	5.5	NWC	288
AS14	CP304L	5.5	PW	320
AS17	CP304L	10.2	NWC	288
AS18	CP304L	10.2	HWC	288
AS19	CP304L	10.2	PW	320
AS22	CP304L	47.5	NWC	288
AS23	CP304L	47.5	PW	320
SW36	CP304L	4.4	NWC	288
SW37	CP304L	4.4	PW	320
BS13	CP316	5.5	PW	320
BS16	CP316	10.2	PW	320
B123	CP316	5.4	NWC	288
B126	CP316	25.0	PW	320
BR15	CP316	4.8	PW	320
CR13	CP316+Ti	4.8	PW	320
ES14	HP304L	11.8	PW	320
ES16	HP304L	10.2	HWC	288
ES21	HP304L	10.7	NWC	288
FS13	HP304L-C	9.1	PW	320
GS13	HP304L+Mo	11.8	PW	320
GS14	HP304L+Mo	11.8	NWC	288
HS13	HP304L+Si	7.8	NWC	288
KS13	HP304L+Ni	9.6	NWC	288
LS13	HP304L+Ni,Cr	9.1	NWC	288
PS13	HP316L+Hf	9.6	PW	320
PS14	HP316L+Hf	9.6	HWC	288
PS15	HP316L+Hf	9.6	NWC	288

2.1.2 Neutron irradiated tensile bars from CIR project

In addition to the material mentioned previously, crack initiation studies have also been carried out on the materials shown in Table 2-8 below. A total of eleven different stainless steel alloys were obtained in neutron irradiated condition. Among these alloys four alloys are in commercial purity (CP) standard while seven different alloys were fabricated from high purity (HP) 304L stainless steel alloy with minor modification to the minor alloying elements.

Table 2-8: Chemical compositions of tested alloys in wt %. Designations FS-PS have the solute addition element indicated in bold.

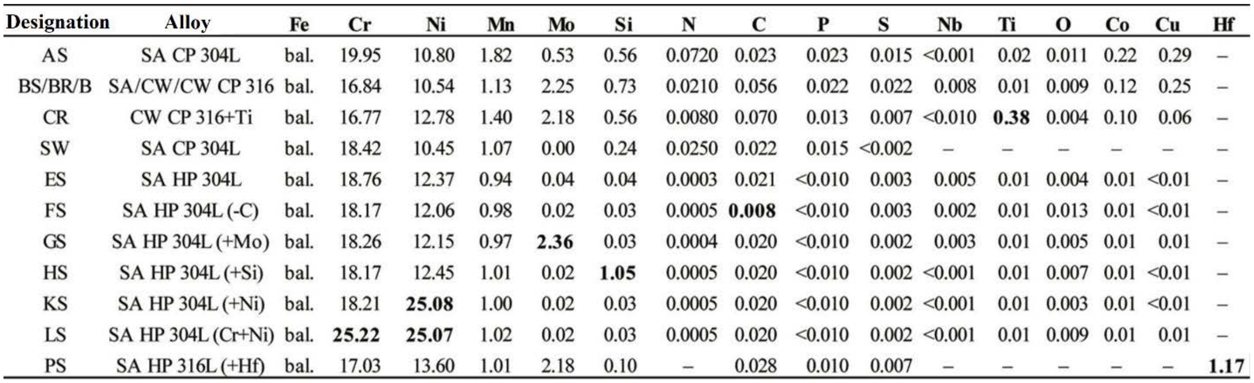

Designation	Alloy	Fe	Cr	Ni	Mn	Mo	Si	N	C	P	S	Nb	Ti	O	Co	Cu	Hf
AS	SA CP 304L	bal.	19.95	10.80	1.82	0.53	0.56	0.0720	0.023	0.023	0.015	<0.001	0.02	0.011	0.22	0.29	–
BS/BR/B	SA/CW/CW CP 316	bal.	16.84	10.54	1.13	2.25	0.73	0.0210	0.056	0.022	0.022	0.008	0.01	0.009	0.12	0.25	–
CR	CW CP 316+Ti	bal.	16.77	12.78	1.40	2.18	0.56	0.0080	0.070	0.013	0.007	<0.010	**0.38**	0.004	0.10	0.06	–
SW	SA CP 304L	bal.	18.42	10.45	1.07	0.00	0.24	0.0250	0.022	0.015	<0.002	–	–	–	–	–	–
ES	SA HP 304L	bal.	18.76	12.37	0.94	0.04	0.04	0.0003	0.021	<0.010	0.003	0.005	0.01	0.004	0.01	<0.01	–
FS	SA HP 304L (-C)	bal.	18.17	12.06	0.98	0.02	0.03	0.0005	**0.008**	<0.010	0.003	0.002	0.01	0.013	0.01	<0.01	–
GS	SA HP 304L (+Mo)	bal.	18.26	12.15	0.97	**2.36**	0.03	0.0004	0.020	<0.010	0.002	0.003	0.01	0.005	0.01	0.01	–
HS	SA HP 304L (+Si)	bal.	18.17	12.45	1.01	0.02	**1.05**	0.0005	0.020	<0.010	0.002	<0.001	0.01	0.007	0.01	<0.01	–
KS	SA HP 304L (+Ni)	bal.	18.21	**25.08**	1.00	0.02	0.03	0.0005	0.020	<0.010	0.002	<0.001	0.01	0.003	0.01	<0.01	–
LS	SA HP 304L (Cr+Ni)	bal.	**25.22**	**25.07**	1.02	0.02	0.03	0.0005	0.020	<0.010	0.002	<0.001	0.01	0.009	0.01	0.01	–
PS	SA HP 316L (+Hf)	bal.	17.03	13.60	1.01	2.18	0.10	–	0.028	0.010	0.007	–	–	–	–	–	**1.17**

The CP alloys have designations A, B, and C, where the first letter refers to the designation in Table 2-8. Alloy A was a type 304L SS alloy representative of a BWR core shroud material while alloy B was type 316 SS alloy representative of the PWR baffle bolt material. In addition to these materials, alloy C was a modified type 316L+Ti material, and alloy SW was a Swedish heat of type 304L SS alloy, similar to the alloy A. For the alloy designation scheme shown in Table 2-8, the second letter denotes the condition of the material. The designation S refers to the material being in a solution annealed condition with the solution annealing being done at 1050°C for 0.5 h followed by water quenching. The designation R represents the material being in a cold worked condition prior to testing. The amount of cold worked was not reported for these materials [5].

In addition to these commercial purity alloys, seven HP alloys with designations E, F, G, H, K, L and P were used for the crack initiation study. Alloy E was used as the model base alloy for the fabrication of alloys G, H, K and L. Alloys G, H, K and L were remelted for the purpose of solute addition of Mo, Si, Ni and Ni+Cr respectively while alloy F was created from a separate starting material to produce an alloy with low carbon content. Alloy P was produced from a type 316 SS base alloy with hafnium (Hf) as the oversized solute addition. All these alloys were given a cold rolling treatment followed by solution annealing between 900°C and 1200°C for a duration of 0.5 to 1 h in between cold rolling passes in order to get a final ASTM grain size between 6 and 8 for each condition [5].

2.2 *Microstructure Characterization*

This section outlines the preparation procedure and analysis techniques used for the microstructural characterization of the material for this research project, including micro-hardness, TEM, and APT analysis.

2.2.1 Micro-Hardness Measurement

Micro-hardness measurements were made to evaluate the bulk changes in the irradiated microstructure. Prior to the measurements, specimens were mechanically polished with a succession of finer grits, ending with a 3 μm diamond polish. The specimens were then electropolished at room temperature for 15 seconds at 30V using a commercial Struers A2 solution at LAMDA at ORNL. After electropolishing, provided no defects or scratches were observed, the specimens were measured using a Vickers micro-hardness indenter at ORNL. Each specimen was measured at a load of 200 gf, with at least 30 independent indents used to determine the average hardness and standard deviation.

2.2.2 Transmission Electron Microscopy (TEM) Analysis

TEM foils for dislocation loop analysis were prepared by jet thinning using a commercial Struers A2 solution at LAMDA at ORNL. Dislocation loops were examined with rel-rod technique using JEOL 2100 STEM at ORNL. Dislocation loops were imaged at different locations under the [110] zone axis. The number of loops characterized is dependent on the number density and in the as-irradiated condition, 670 loops were characterized.

Radiation induced segregation (RIS) was assessed in the BWR irradiate 304L SS. Energy-dispersive X-ray Spectroscopy (EDS) maps were taken from random high angle boundary using the FEI Talos microscope at the LAMDA laboratory at ORNL using a map size of 1024x1024 pixels with a resolution of ~0.23 nm/pixels with a probe full width half max of ~1.5nm. Each scan had a duration of one hour with more than 100,000 counts/sec with dead times from 1-6%. The Talos microscope has a much higher counting rate compared to typical STEM/EDS by virtue of the use of multiple EDS detectors. Prior to EDS measurement, the grain boundary was tilted to an edge-on position to maximize the spatial resolution of the measurement. Due to the limitation of available grain boundaries for RIS, only one grain boundary was measured, but multiple EDS maps were obtained from different segments of that grain boundary. The x-rays counts were converted to weight percentages using the Bruker Esprit© 1.9 software package, which uses the Cliff-Lorimer calculations for each pixel.

2.2.3 Atom Probe Tomography (APT) Analysis

Precipitates/solute clusters were analyzed using the atom probe tomography. Needle-shaped APT specimens were prepared by the standard lift-out method and focused ion beam milling using Quanta 3D at ORNL. Specimens were prepared from the electropolished 3-mm disk. Prior to the lift-out procedure, Pt was deposited to protect the material from ion beam damage. A final 5 kV clean-up procedure was utilized to minimize the Ga damaged regions and reduce the tip radius to ~50 nm. About 6 APT tips were made for each condition for APT analysis. APT specimens were analyzed using a LEAP-4000XHR microscope at the University of Michigan operated in electrical mode with a voltage pulse fraction of 20%. Specimen temperature was maintained at 50 K and detection rate was kept constant at 0.005 atom/pulse.

Reconstruction of the relative atom positions from the raw data was performed using the commercial software, IVAS 3.6.4 from CAMECA™. Solute clusters were analyzed using the maximum separation method. The nickel-silicon solute clusters were defined by the tenth order spacing of silicon atoms with a suitable d_{max} (the maximum separation of tenth-order silicon atoms) was selected to best separate the clustered and randomized silicon atoms based on the spacing distribution. The aluminum-copper solute clusters were defined by the fourth order spacing of aluminum atoms with a suitable d_{max} (the maximum separation of fourth-order aluminum atoms) was selected to best separate the clustered and randomized aluminum atoms based on the spacing distribution. For both cluster types the value of N_{min}, the minimum accepted cluster size by atom number of selected type (i.e. silicon or aluminum), was chosen to be equal to the maximum cluster size observed for a randomized experimental APT dataset.

2.3 *Test systems and procedures*

2.3.1 Test Systems

The CERT and CGR testing systems, IM1 and IM5 are located in the Irradiated Materials Testing Laboratory (IMTL) at the University of Michigan. Both systems have similar water loops for which a schematic diagram is shown in Figure 2-4. The water loops consist of two sub loops, loop 1 for conditioning the water at room temperature and low pressure, and loop 2 for simulating light water reactor environment at high temperature and high pressure. The environmental parameters such as conductivity and dissolved gas concentration can be well controlled and maintained in loop 1. The water then is pressurized and heated in loop 2, reaching the desired temperature and pressure in the autoclave and recirculates to the primary water column. The conductivity and dissolved oxygen (DO) are monitored at both inlet and outlet of loop 2.

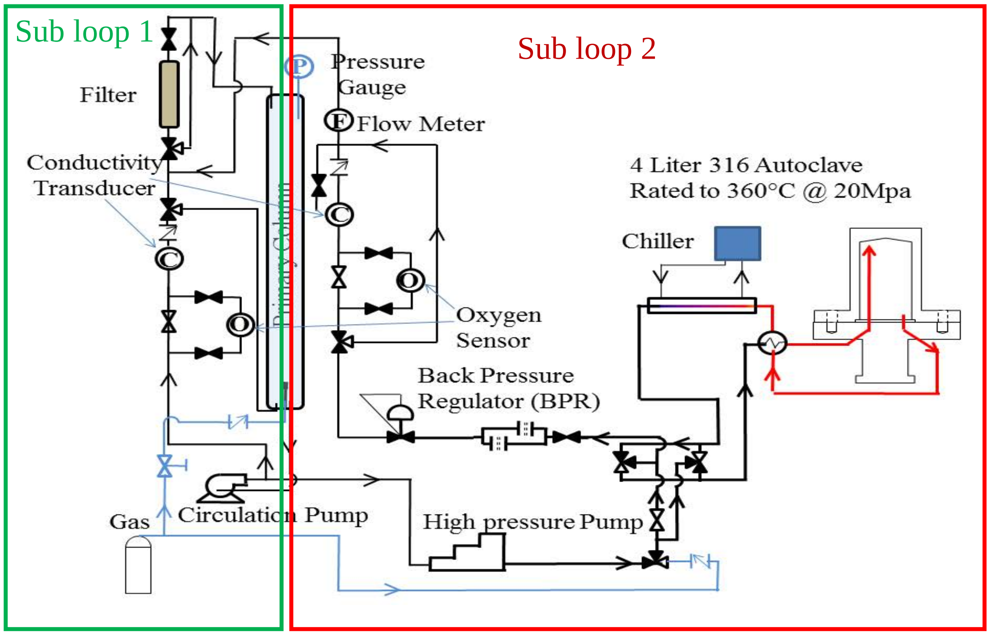

Figure 2-4: Schematic of the water loop used in the IM systems in the Irradiated Materials Testing Laboratory.

The CERT experiments were performed using the IM1 autoclave system. The IM1 loading system can strain up to four tensile bar samples simultaneously, while the application of load is controlled using a 50 kN servo motor. A linear variable differential transformer (LVDT) is mounted on the crosshead to measure displacement. Four pull rods, each containing a load cell, connect each sample to the crosshead. Each of the pull rods are sealed at the feed-through into the autoclave with a self-energizing graphite seal with an internal spring that expands under pressure. Each pull rod is connected to an Inconel 625 sample loading fixture. Electrical insulation is provided by zirconia washers located in the loading fixtures. After loading the specimens, the autoclave body is sealed to the autoclave head, thus preventing any leakage during the experiment.

CGR tests were performed using the IM5 autoclave system. A DCPD system using a program named AT5 (proprietary program written by Peter Andresen not published) was used to control *K* value and monitor the crack growth rate. Due to the planned testing of highly irradiated specimens, IM5 was designed as a mobile system, such that an experiment could be performed in a hot cell, thus significantly reducing the dose to the operator. Wires were spot welded onto the neutron-irradiated RCT sample in hot cell #1 using manipulator arms. Then the whole autoclave containing the RCT sample was moved to hot cell #2 for testing. The water loops and controls remained outside of the hot cell for easy access during the experiment. Figure 2-5 shows the images of test system.

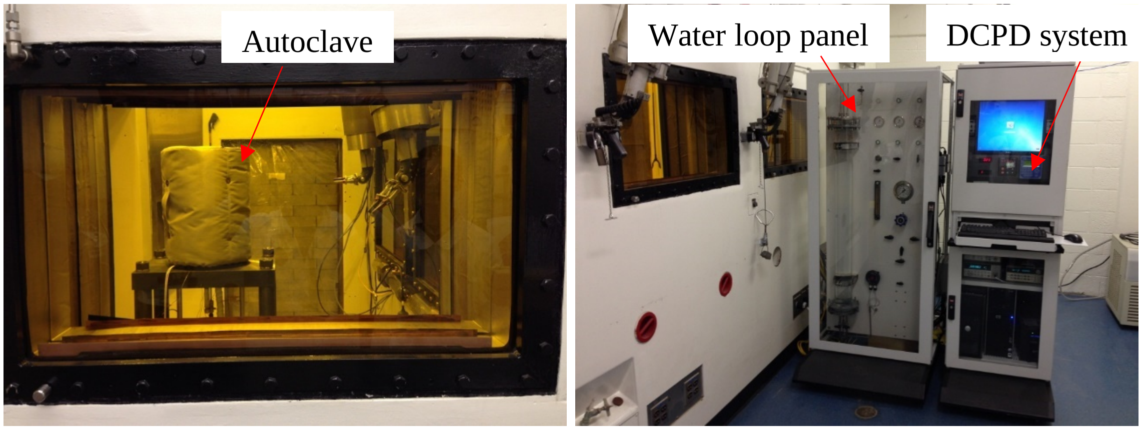

Figure 2-5: Images of CGR test system IM5 in hot cell #2.

Crack growth is measured using the reversed Direct Current Potential Drop (DCPD) technique, which has long been used for crack growth monitoring in high temperature water environments. As shown in Figure 2-6 (a), the DCPD monitoring system consists of a DC power supply, relays, nano-volt meter, data acquisition unit, servomotor and a Skala brand controller. DC power supply provides stable current (2.5 A for 0.5 T RCT) to a specimen. The current is reversed once per second through solid-state relays to correct for thermocouple effects. The current and potential probe leads were spot-welded to the RCT specimen as shown in Figure 2-6 (b). The potential drop resulting from crack propagation in the specimen is measured by a nano-volt meter. Data acquisition and instrument control are all integrated in a DOS program called AT5, which was developed by Dr. Peter Andresen at GE Global Research Center. A data processing program called HIKO, based on DotNetFX2.0 was also used in this study.

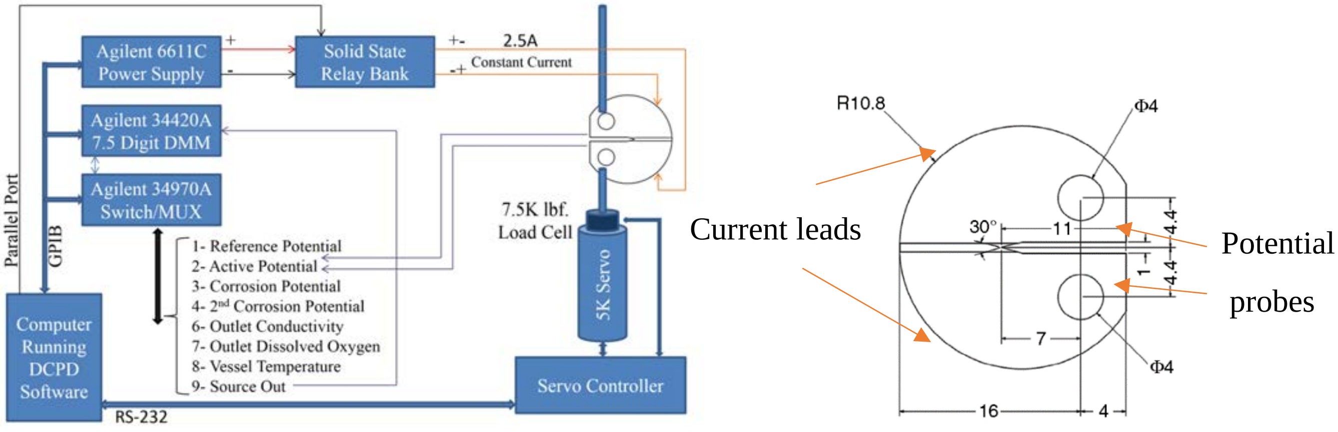

(a)

(b)

Figure 2-6: DCPD monitoring system. (a) a schematic of DCPD instrumentation and circuit diagram, and (b) arrangement of current and potential probe leads on the 0.5T RCT specimen.

2.3.2 Procedures for CERT test

Tensile Bar Annealing and Surface Preparation

During the original machining of the tensile specimens, EDM was used to cut the parallel flats on opposing sides of the gauge section, leaving rounded sides between the parallel flats. EDM leaves a thin, amorphous recast layer that may affect the cracking behavior in a simulated-BWR environment. As such, the gauge section flats were mechanically polished to remove the EDM recast layer. However, due to the high radioactivity of the specimens this procedure was completed in a hot cell facility using manipulators. First both tensile heads were clamped in a small vice, to prevent any possible bending, and a polishing paper was carefully moved across the gauge flats. An 800-grit sandpaper was first utilized to remove the EDM layer, while a 1200 grit paper was utilized to prepare the surface for a later electropolishing. The removal of the EDM layer was monitored by the usage of an in-cell camera. The rounded sides between the EDM flats were left in the as-machined condition prior to the electropolishing procedure.

Electropolishing was completed on the tensile specimens to create a final surface finish satisfactory for CERT testing in both simulated BWR environment and an inert argon environment. The electropolishing operation was completed in the hot cell fume hood. The electropolishing setup was quite simple, consisting of a power supply, a grid cathode, and a beaker of electrolyte. The electropolishing was completed at 30V and consist of four 15 sec polishing increments, between each of which the specimen was flipped. This procedure was expected to remove roughly 20 μm of material based on prior experiments. After electropolishing, each specimen was observed via an optical microscope to verify a good surface quality.

CERT Test: PIA conditions

For these materials, CERT tests were conducted in a simulated boiling water reactor normal water chemistry (BWR-NWC) environment. During each straining, system water pressure was maintained at 9.7 MPa and temperature at 288^{o}C, while the outlet dissolved oxygen and conductivity were maintained at 200 ppb and 0.2 μS/cm, respectively.

After pressurizing and achieving the desired temperature for the intended environment, the system was allowed to stabilize until conductivity had dropped below 0.2 μS/cm. Upon stabilization, dissolved gas was added to the primary water column and the target concentration was achieved by regulating the main column pressure with a back-pressure regulator. Following gas addition, the environment stabilized for an additional period of 12 hr before commencing straining. During this 12 hr period, conductivity control was initiated once the vessel outlet water conductivity again dropped below 0.2 μS/cm. Conductivity was controlled by adding small amounts of dilute H_2SO_4 to the primary water column with the peristaltic pump, which was set to operate whenever conductivity would decrease below the target.

Due to the crosshead arrangement, non-irradiated type 304L SS tensile bar specimens were used to occupy empty loading locations and provide load balance at the system crosshead. These specimens were selected such that they would have a similar yield stress as the irradiated specimen currently being examined.

Prior to straining, a preload of 20 MPa was applied to each specimen. At the end of the 12 hour stabilization period, straining was initiated by moving the crosshead with the servo motor. This displacement was completed at a rate of 1.65 x 10^{-7} in/s for all experiments, which corresponds to a strain rate of 3.0 x 10^{-7} s^{-1}. During the stabilization period and straining, all environmental and stress-strain data were recorded every 30 s using the LabView data acquisition program. Recorded data includes inlet and outlet water pressure, inlet and outlet water conductivity, outlet dissolved oxygen, vessel internal and preheater temperature, LVDT displacement, and load cell readings.

Dislocation Channeling Characterization

As previously discussed, increased localization of deformation has been closely correlated with increasing cracking susceptibility [6], however, the change in localized deformation following PIA treatments has never been measured for a neutron-irradiated material. Furthermore, more recent studies [7-9], have indicated that dislocation channels that terminate at grain boundaries have a higher propensity of crack initiation.

For this study, the straining experiments were completed in small increments, such that we could more precisely identify points of crack initiation and study the development of the localized deformation. After each stress/strain increment the specimen was removed from the autoclave and was examined using a JEOL JSM-6480 SEM. This examination was used to determine the plastic strain through the relative displacement of fiducial markings, as well as recording any sites of crack initiation and changes in the localized deformation.

The dislocation channel characterization focused on the changes in both the total dislocation channel density and the density of channel-grain boundary interaction sites, which were characterized as either continuous or discontinuous, with increasing plastic strain. A continuous channel-grain boundary site refers to a location where a dislocation channel intersects a grain boundary but is then able to transmit slip across said boundary. Contrarily, a discontinuous interaction site is one where the channel terminated at the grain boundary with no evidence of slip transfer across it. By comparing the densities of both continuous and discontinuous interaction sites, one can measure the relative propensity that a condition has for forming continuous channels, and how this may change with both PIA treatments and additional strain.

Following each stress/strain increment both the gage flats were fully imaged at 500x magnification. This magnification allowed for a balance of both image quality and imaging time, while the large-scale imaging also allows for a spatial correlation of images following each additional strain increment.

Post-Failure Fractography

Fractography was performed on each fractured tensile bar following the CERT test using a JEOL JSM-6480 SEM. Low magnification images of the gage surface were taken to identify the locations of IG fracture and secondary cracking, while the edges of the main IG crack and secondary cracks were imaged at higher magnification.

The fracture surfaces of each specimen were also examined in detail to characterize the nature of failure by viewing the fracture surface perpendicular to the tensile axis. Regions of intergranular (IG), transgranular (TG), mixed (IG+TG), and ductile type failure were identified. Higher magnification imaging (>500x) was performed in regions of note.

Reduction of area (RA) was calculated using the total area of the fracture surface viewed perpendicular to the tensile axis. The area of the fracture surface was determined using the Image J™ imaging software program particle analysis feature. The RA is determined by dividing the difference in area between the fractured surface (viewed parallel to the tensile direction) and the original cross-sectional area by the original cross-sectional area.

Regions of IG, mixed IG and TG, and ductile fracture were characterized by area and expressed as an area-based percentage of the total fracture surface. Using the Image J™ program, regions containing each type of fracture were cut from the overall view of the fracture surface and their areas were determined using the particle analysis feature of the software. The area divided by the total fracture surface area yielded the percentage of fracture type.

CERT Testing: BOR-60 Neutron Irradiated Conditions

To evaluate the crack initiation behavior in the four commercial purity (CP) and seven high purity (HP) alloys irradiated in the BOR-60 reactor, CERT tests were performed in the IM1 system with samples pulled to fracture. Specimens were tested in one of three following environmental conditions: Normal water chemistry (NWC), hydrogen water chemistry (HWC) or Primary water chemistry (PWR). Details of the specimen tensile bar and the corresponding testing environment are described in Table 2-8 above. Test conditions and the strain rates were similar to those used in the CIR program previously [10-11]. Environmental conditions were stabilized for durations up to 72 hours prior to start of straining. The water conductivity in the NWC and the HWC environments were maintained by addition of dilute H_2SO_4 solution to the main column water reservoir. The PWR conditions were maintained by addition of Boric acid and lithium hydroxide to the solution. Pressure, dissolved oxygen and water conductivity were monitored at the autoclave inlet and outlet, and the internal autoclave temperature was monitored by thermocouple. The summary of the three different environmental conditions are shown in Table 2-9 below.

The loading system was capable of straining up to 4 samples simultaneously. Load was applied by a computer driven 50 kN servo motor connected to the loading crosshead. Crosshead displacement was measured by a Solartron™ linear voltage displacement transducer (LVDT). Interactive Instruments load cells mounted on each pull rod monitored load on each sample. Load, displacement, and environmental data were collected and recorded by computer data acquisition once every sixty seconds.

Table 2-9: Environmental parameters for CERT tests.

Parameter	NWC	HWC	PW
Temperature	288ºC	288ºC	320ºC
Autoclave Pressure	10.3 MPa	10.3 MPa	12.4 MPa
Conductivity	0.2 μS/cm	0.2 μS/cm	20.5 μS/cm
O_2 concentration	2000 ppb	0 ppb	0 ppb
H_2 concentration	-	100 ppb	3000 ppb
B concentration	-	-	1000 ppm
Li concentration	-	-	2 ppm
ECP (SHE)	215 mV$_{SHE}$	-570 mV$_{SHE}$	-860 mV$_{SHE}$

Data Analysis and Fractography

Plots of stress versus strain were created using load and displacement data, to compare mechanical properties such as the yield stress, max stress, uniform elongation, and total elongation. Before analysis, stress and strain data were adjusted to account for system pressure and pull rod compliance, respectively.

A tare pressure was added to each load cell measurement, by calculating the load due to the autoclave pressure acting on the cross-sectional area of each 3/16” diameter pull rod. Tare pressure on the 2 mm diameter tensile bar samples was 58.6 in NWC and HWC and 70.3 MPa in PW.

To adjust for system compliance, each raw stress-strain curve was plotted to determine the apparent modulus, generally ~10,000 MPa. LVDT displacement values were converted to strain by dividing the change in displacement by the original specimen gage section length (12 mm). The apparent modulus was determined by fitting a linear trend line to the linear elastic region of the curve. A good linear fit (i.e., R^2 value minimum of 0.999) was created by eliminating data points at low stress. The apparent modulus was then divided by the reported modulus for type 304 SS at 300ºC, 166.3 GPa [12]. The resulting ratio was multiplied by the apparent strain up to the yield point to calculate the correct(ed) strain of the gage section for the elastic region of the curve. This method is consistent with the general definition of compliance: the change in length due to compliance is equal to the observed change in length less the force divided by the system stiffness, where stiffness is equal to either: force divided by the change in length, or system modulus multiplied by cross sectional area divided by original length [13]. Plastic strain data was calculated from the data recorded after yielding by subtracting the difference in strain between the original strain and the compliance corrected strain. No compliance correction was made during plastic elongation.

After correcting for system pressure and compliance, several measures were determined from the stress-strain curve. Yield stress (YS) was recorded as the 0.2% offset YS if strain hardening was observed. In the case of strain softening, YS was taken to be the maximum stress. Uniform elongation (UE) was recorded as the strain at which the maximum stress occurred. Total elongation (TE) was recorded as the strain at the point of fracture.

Fractography was performed on each tensile bar following CERT testing using a JEOL JSM-6480 SEM. Gage and fracture surfaces were examined in detail, and the nature of failure was characterized. Samples showed combinations of ductile, intergranular (IG), transgranular (TG), or mixed mode IG/TG type cracking. Reduction of area (RA) was calculated by dividing the difference between the fracture surface area and the original cross-sectional area by the original cross-sectional area. Areas of IG, TG or mixed IG/TG fracture were determined and expressed as an area-based percentage of the total fracture surface.

2.3.3 Procedures for CGR Test

Test steps

RCT-3 (550^{o}C, 20 h) and RCT-2 (as-irradiated) were tested first. The main purpose of the CGR test is to determine the *K* dependence of the CGR rate and the effect of environment change on CGR. The post-irradiation heat treatment of sample RCT-3 was expected to have removed much of the damage due to irradiation in reactor. To compare the SCC susceptibility between different samples, it is desirable to test them at same *K* levels. Meanwhile, the applied *K* values should meet the validity criterion to ensure mainly plane strain conditions at the crack tip:

$$2.5(K/\sigma_{\mathrm{YS}})^2 < W\text{-}a < B_{\mathrm{eff}} \qquad (2\text{-}1)$$

where σ_{YS} is the yield strength of material, W-a is the remaining length of the crack and B_{eff} is the effective width of the sample. For irradiated sample, the effective σ_{YS} is normally taken as:

$$\sigma_{\mathrm{YS}} = \sigma_{\mathrm{YS(unirrad)}} + (\,\sigma_{\mathrm{YS(unirrad)}} - \sigma_{\mathrm{YS(irrad)}})/2 \qquad (2\text{-}2)$$

or

$$\sigma_{\mathrm{YS}} = \sigma_{\mathrm{YS(unirrad)}} + (\,\sigma_{\mathrm{YS(unirrad)}} - \sigma_{\mathrm{YS(irrad)}})/3 \qquad (2\text{-}3)$$

where $\sigma_{\mathrm{YS(irrad)}}$ is the yield strength of the irradiated material and $\sigma_{\mathrm{YS(unirrad)}}$ is the yield strength of its unirradiated counterpart. So far there is no consensus on how to calculate the effective yield strength. For highly irradiated material with little work hardening capability, equation (2-3) is preferred.

As the samples have been annealed at different conditions and possess different work hardening capabilities, different methods for calculating the effective yield strength were used. For samples with limited work hardening such as RCT2 (as-irradiated) and RCT1 (500^{o}C, 1 h), equation (2-3) was used. For RCT4 (550^{o}C, 5 h), equation (2-2) was used. The yield strength of RCT3 (550^{o}C, 20 h) was not adjusted. Based on the *K* validity check for the expected behavior of the as-irradiated (RCT2) and the PIA: 550^{o}C, 20 h specimens (RCT3), three nominal *K* values were selected for CGR testing: 18, 14, 11 MPa.m$^{1/2}$. The test steps are listed in Table 2-10.

Table 2-10: Test steps for RCT tests.

Step	**Water chemistry**	**Stress intensity (MPa.m$^{1/2}$)**	**Waveform**	**Intended crack growth (mm)**
1	BWR NWC	18	Precracking Haversine to Trapezoid	~0.8
2	BWR NWC	18	Constant K	0.09
3	BWR HWC	18	Constant K	0.09
4	BWR NWC	18	Constant K	0.09
5	BWR NWC	18 to 14	K transition Trapezoid	0.128
6	BWR NWC	14	Constant K	0.09
7	BWR NWC	14 to 11	K transition Trapezoid	0.128
8	BWR NWC	11	Constant K	0.09
9	BWR HWC	11	Constant K	0.09

Sample welding

Due the annealing treatment, a slight oxide layer was developed on the RCT specimens that underwent PIA treatments, despite the stainless steel oxygen getter that was utilized. This oxide layer would be detrimental to the later spot welding of the DCPD probes, thus it had to be removed via mechanical polishing. In the hot cells at ORNL the RCT specimens were mounted onto a specially designed apparatus, which slowly rotated the specimens while an 800-grit sandpaper was applied to the specimen; special attention was also given to front flats of the RCT specimens. After completing the annealing and mechanical polishing the RCT specimens were shipped to the University of Michigan.

The current leads and potential probes need to be spot welded onto the RCT sample for DCPD measurement. Due to the radioactivity of neutron-irradiated samples, the welding had to be implemented in hot cell via manipulator. A set of tools and welding procedure have been successfully developed in this lab and were described in ref. [14]. Figure 2-7 shows the RCT sample after spot welding.

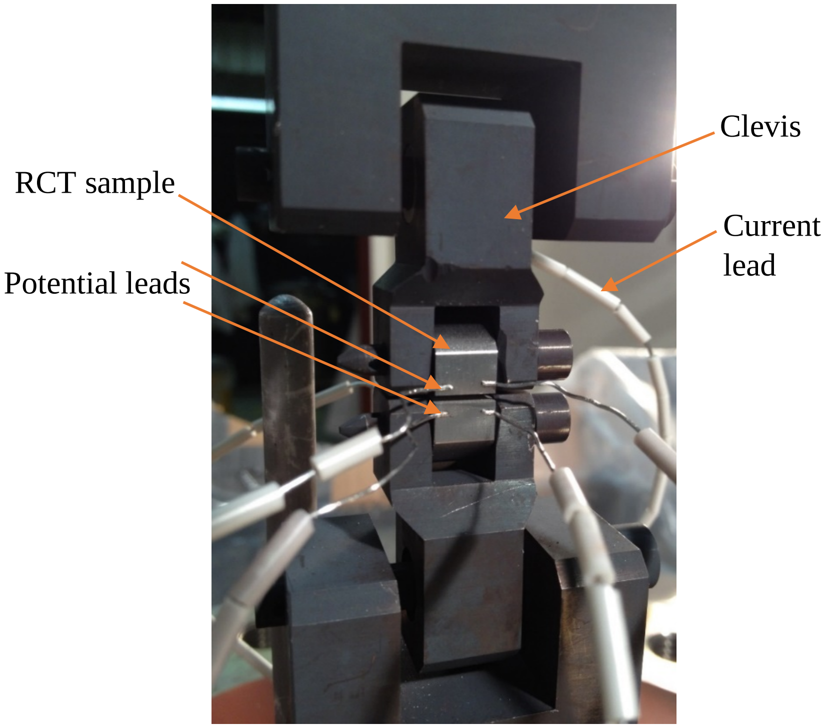

Figure 2-7: RCT sample spot welded in a hot cell.

Water Chemistry

The CGR tests were conducted in a BWR environment, including both NWC and HWC. Temperature and pressure of the testing system are 288°C and 10.3 MPa, respectively. The water in the 3.5 L autoclave was refreshed three times per hour with a flow rate of 180 mL/min. The conductivity of inlet DI water was 0.056 µS/cm. Inlet dissolved oxygen (DO) was controlled at 2 ppm for NWC and dissolved hydrogen (DH) was controlled at about 100 ppb for HWC. DO and conductivity of inlet/outlet water were continuously monitored using a Thornton 770Max DO/conductivity meter.

ECP Measurement

The electrochemical potential (ECP) of the RCT specimen was continuously monitored during the CGR test with a Cu/Cu_2O reference electrode. At the same time, the redox potential between a 1.0 cm^2 Pt flag and the reference electrode was also recorded. The measured potentials were converted to potentials vs standard hydrogen electrode (SHE) by subtracting 0.273 V.

Reset Initial a/W in High Temperature Water

During heating, the DCPD potential reading increases with temperature because of the increasing resistivity of metallic materials. So the initial a/W from direct measurement should be recorded and reset in AT5 once the DCPD potentials stabilize at the target temperature. A fatigue pre-crack step was conducted in high temperature water before beginning the stress corrosion cracking test in the same environment. In this case, the final a/W in air needs to be set as the initial a/W prior to growing the crack at the testing temperature.

Crack Growth Procedures

After loading the sample in the grips, the current and potential wires for DCPD measurement were spot-welded to the CT specimen as described above. The wires in each pair were twisted in order to cancel magnetic fields. A thermocouple for temperature control was placed at the crack plane in the autoclave. Once the temperature, conductivity and DO reached the target levels, the a/W for DCPD readings was reset to the initial value. After that, the system was ready for controlling *K* on the sample. The tare load from high pressure water was accounted for in AT5. The temperature inside the autoclave, inlet and outlet pressure, inlet and outlet conductivity, and inlet and outlet DO were continuously recorded during the entire test period.

The maximum *K* was slightly lower than that being used for the next constant K step. At the beginning of the test, low loading ratio *R* and high frequency ν, were used to introduce cracking at a fast rate and to leave beach marks as evidence on the fracture surface for tracking the crack growth in each step. Later, in order to initiate the transition from TG to IG, *R* was decreased to 0.6 and the frequency was lowered from 0.1 to 0.01, and then to 0.001 Hz. After 0.001 Hz fatigue, a trapezoidal load form was applied with a holding time of 9000 seconds. Subsequently, constant *K* control was started.

Auto *K* control

The CGR is highly dependent on the *K* value applied on the sample. In order to reliably measure the CGR at a certain *K* value, the value of *K* should be kept constant during the test. According to ASME standard E-399 [15], *K* is a function of *a/W* and load:

$$K = \frac{P}{B\sqrt{W}} f\left(\frac{a}{W}\right) \tag{2-4}$$

where:

$$f\left(\frac{a}{W}\right) = \frac{\left(2+\frac{a}{W}\right)\left[0.76+4.8\frac{a}{W}-11.58\left(\frac{a}{W}\right)^2+11.43\left(\frac{a}{W}\right)^3-4.08\left(\frac{a}{W}\right)^4\right]}{\left(1-\frac{a}{W}\right)^{3/2}} \tag{2-5}$$

For which: *P* is applied force, *B* is the sample thickness, *W* is the sample width and *a* is the crack length. So, the applied force should be adjusted as the crack grows to maintain a constant *K*. AT5 has a built-in auto *K* control function which can adjust the applied load automatically once a minimum increase (set to 0.01 in the program) in *a/W* is achieved.

d*K*/d*a* Control

It is very important to sustain the crack growth when changing the *K* value. d*K*/d*a* control was used for a smooth transition for both increasing and decreasing *K*. Trapezoid waveform was normally used during *K* transition. AT5 also has this built-in function. The rate of change of *K* with *a* (d*K*/d*a*) is calculated based on the *a/W* and *K* values from two neighboring steps. As the crack grows, a change in *K* will be made based on the d*K*/d*a* value. The upper threshold for the *K* change was set to 0.02 ksi·in$^{1/2}$.

Post-test Cracking

When the test was finished in high temperature water, the autoclave system was cooled to room temperature. The sample was cracked open at room temperature using fatigue loading. To minimize the plastic deformation at the crack front formed in the environment, *K* was controlled at the same (or lower) level as that last used in high temperature water. After growing a post-test crack about 0.5 mm, the RCT specimen was fatigued at high frequency until it broke.

Fractography

The fracture surfaces of the RCT specimen were observed using both optical microscopy and scanning electron microscopy (SEM). The fracture surface was examined for evidence of each step change during the crack growth rate test. The morphology of the fracture surface, especially transgranular (TG) or intergranular (IG) features and the transition between TG and IG, was confirmed. The area of intergranular fracture surface was measured and divided by the width of sample to calculate the average length of IGSCC growth. The measured crack length from fracture surface analysis was compared with that from DCPD measurement. The ratio between them was used as correction factor for crack length and crack growth rate.

K correction after CGR test

As the real crack length is not exactly the same as the DCPD measured value, neither is the real *K* the same as the nominal *K*. After CGR test, the crack length was corrected using the correction factor mentioned above. *K* was recalculated using the corrected crack length and the applied load which was recorded in the data file.

2.3.4 Crack Initiation Studies using Four Point Bend Test

In order to study the crack initiation behavior of the neutron irradiated alloys, a modified four-point bend test was used as the testing method. The specimens used for testing were obtained from cutting a slice from the heads of the neutron irradiated tensile bars previously tested in the CERT system. The schematic of the specimen dimensions and the location from which the slices were made are shown in Figure 2-8 below.

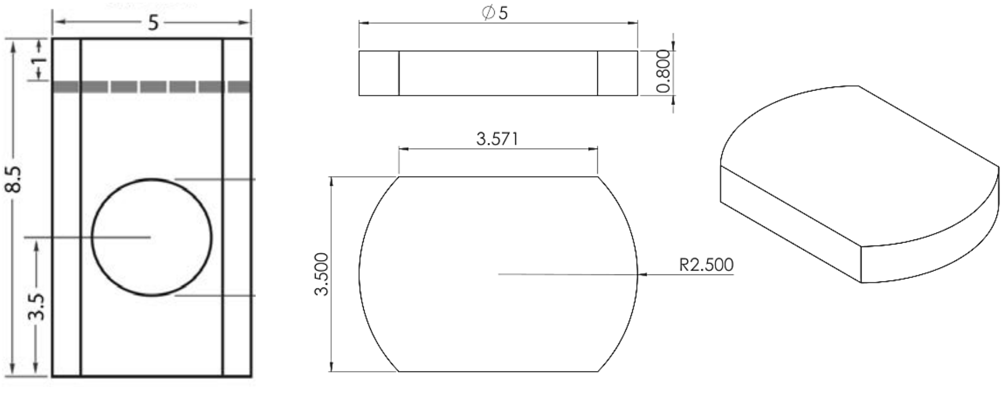

(a) (b)

Figure 2-8: Schematic showing a) tensile bar head dimensions and location of the cut (gray dashed line), and b) bend test sample dimensions.

Prior to testing, the four-point bend test specimens were created from the shoulder region of the tensile bars in the LAMDA facility at ORNL. 1 mm thick slices were generated and were mechanically polished on both sides to create a specimen with a thickness of about 800 μm. A Buehler Mini-met 1000™ sample grinding and polishing tool performed sample thinning to a target thickness of 800 μm using 120, 180, and 340 grit SiC grinding paper on each side to achieve a uniform thickness (final thickness variations were less than 10 μm). One side of each sample was then polished with a nylon pad containing 3 μm polishing media in the Mini-met™ and subsequently electrochemically polished in a Struers LectroPol-5™ system. One electrochemical polishing step was applied for 15 s at a potential of 30 V at 20 °C in a commercially available Struers A2 solution (60% perchloric acid). Parent tensile bar ID, bend sample ID, dose, and thickness are presented in Table 2-11.

Table 2-11: Samples for four-point bend SCC testing.

Parent Tensile Sample ID	Bend Sample ID	Dose, dpa	Thickness, μm
AS14	AS01	5.5	825
AS14	AS02	5.5	797
AS14	AS03	5.5	839
AS14	AS04	5.5	801
AS18	AS05	10.2	813
AS19	AS06	10.2	796
AS17	AS07	10.2	791
AS19	AS08	10.2	777
AS22	AS09	47.5	807
AS23	AS10	47.5	729
ES16	ES01	10.2	770
ES21	ES02	10.7	804
KS13	KS01	9.6	806
KS13	KS02	9.6	815

2.3.5 Finite element analysis

Prior to testing of the neutron irradiated specimens, finite element analysis was performed to optimize the loading fixture and estimate the stress strain distribution on the specimen surface. The details of the FEA analysis have been reported previously [16] and the results are summarized in Section 3.5.1.

To benchmark the four-point bend test setup and evaluate the strain profile on the specimen surface, two different material conditions were used in the simulation, based on the tensile stress-strain behavior of the unirradiated AR and 16.9% cold worked 304L SS alloy. The modulus of these two conditions was that for type 304 SS at 300 °C, 166.3 GPa, the Poisson’s ratio was 0.3, and the density was 7.8 g/cm^3. The respective yield strength and strain hardening coefficients were determined from tensile tests performed in the IM1 test system. The AR and 16.9% CW conditions had yield strength of 445 and 783 MPa, and strain hardening coefficients 4.5 and 7.5 GPa, respectively. The final loading geometry was designed to create a uniaxial tensile strain of up to 3%, which is sufficient to induce cracking in neutron irradiated austenitic stainless steels.

The four-point bend test fixture used for the study was fabricated from Inconel 718 alloy in accordance with the schematic shown in Figure 2-9 below. Heat treatment of fixture parts, post-fabrication, created a hardened state to prevent deformation during bend testing. Four round posts called centering pins, elevated from the bottom support surface by 0.4 mm, surrounded the sample to prevent rotational misalignment. Set screws to the left and right of the sample centered the sample laterally and were retracted after pre-loading the sample to prevent constraint during bending. The loading fixture was electrically insulated with zirconia washers in the connection between the pull rod and the loading fixture.

Bend samples were loaded into the fixture with tweezers, centered by tightening the set screws on either side, and held in place by bringing the loading points into contact with the sample and lightly tightening the connection of the pull rod at the system crosshead.

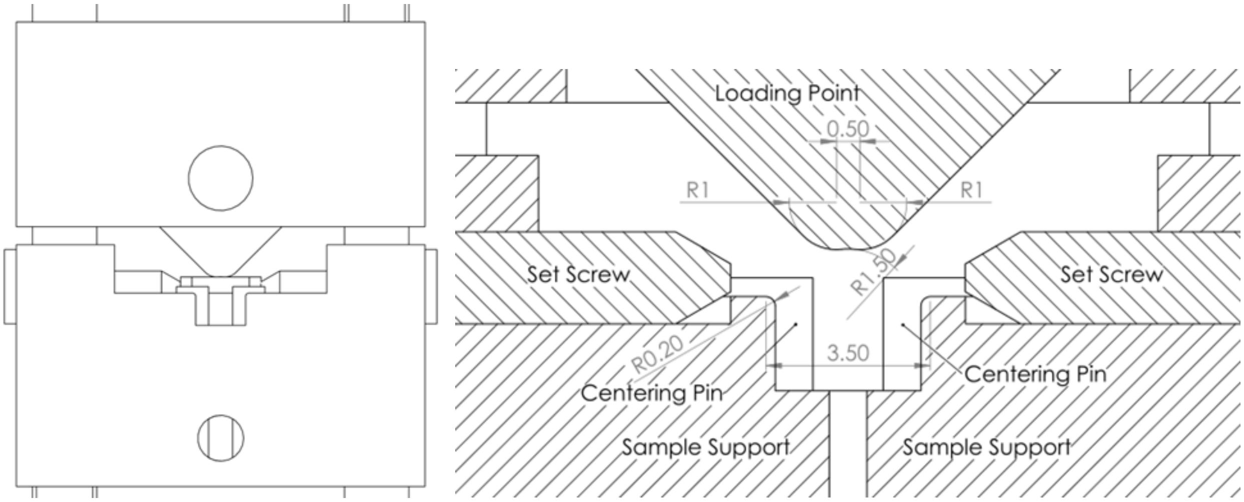

Figure 2-9: Schematic of the four-point bend loading fixture. Left: front view including bend sample, right: cross sectional view excluding the bend sample, showing dimensions in mm.

Four-point bend tests were carried out using the IM1 system in the Irradiated Materials Testing Laboratory (IMTL) at University of Michigan. The details of the closed water loop and the autoclave environment have been described previously in this report for the CERT testing.

Tests were performed in room temperature (RT) air, 288°C Ar gas, or 288°C normal water chemistry (NWC) conditions. Sample bending was performed by moving the crosshead at a constant rate of 1.3×10^{-7} in/s, until achieving the desired amount of stress or sample deflection. The crosshead movement rate created a sample strain rate of 3.5×10^{-7} s^{-1}, identical to the strain rate used in the previous CERT experiments.

The testing was performed in increments to create crack initiation sites and limit the amount of crack propagation in the material. Increments are reported in this report as either the fraction of yield stress or the amount of plastic strain added to the material post yielding. Samples' surfaces were imaged between increments using scanning electron microscopy.

To evaluate the dependence of the strain in the material on the deflection, four-point bend tests were carried out on unirradiated material in as-received and cold-worked conditions. The strain after a particular amount of deflection was measured using the digital image correlation technique. Digital image correlation (DIC) was used to map strain on the surface of bend samples after tests in RT air and 288°C Ar gas, to compare with FEA model results. The DIC technique determines displacement by comparing images of a speckle pattern with high contrast difference recorded pre- and post-deformation. Speckle patterns were applied by using high-temperature RustOleum™ spray paint (10), and images were recorded with a Fujifilm Finepix S7000 digital camera used together with a 4x magnification stereoscope, as shown in Figure 2-10. A Matlab script created by McMurtrey [17] was used to make strain maps from the images, and the surface strain for each test was recorded as the average strain determined from the DIC analysis in the center 500x 500 μm region of the bend sample. DIC results were confirmed by comparison with measurements taken from an array of microhardness indentations made on the sample surface prior to deformation.

The specimen deflections were measured using a microminiature LVDT for the tests carried out at room temperature. For the high temperature tests, direct sample measurements were not possible in high temperature environments due to limitations of the electronics in the device, therefore estimations of sample deflection were made by subtracting a load dependent compliance correction factor from the crosshead deflection measurement. This compliance correction factor was determined in both 288°C Ar and 288°C NWC, by loading a ~10 mm thick 'bend' sample with the same cross-sectional geometry as the actual bend test samples. Due to its large thickness, it was assumed that no sample deflection occurred during loading, and compliance correction curves were determined by fitting a second order polynomial to the resulting load vs. crosshead displacement curves. Compliance correction curve determination was repeated three times for accuracy, and averaged to determine the following correction factors in 288°C Ar:

$$CF_{Ar} = -6.57 \times 10^{-5} P^2 + 0.493P - 15.8 \tag{2-6}$$

and in 288°C NWC:

$$CF_{NWC} = -5.56 \times 10^{-5} P^2 + 0.460P - 24.6 \tag{2-7}$$

where P is the applied load in N and CF_i is the correction factor in environment i in μm. The correction factor subtracted from the crosshead deflection yields the sample deflection.

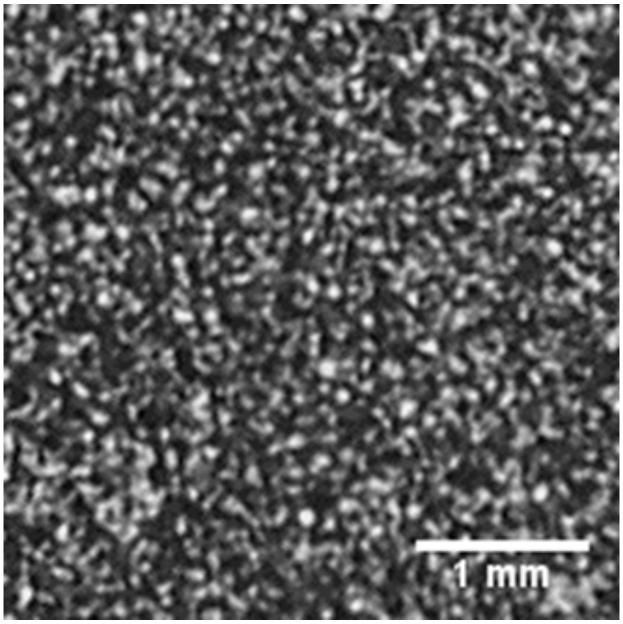

Figure 2-10: DIC speckle pattern applied with Rustoleum spray paint. Particle size ranges between 50 and 100 μm.

2.3.6 Oxide removal

The oxide from exposure during SCC testing was removed after the tests to allow for better observation of IGSCC initiation sites and electron backscatter diffraction imaging in these regions. A chemical procedure which consists of soaks in two water-based solutions is effective at removing surface oxidation,. The first is 100 g/L sodium hydroxide with 30 g/L potassium permanganate, the second is 100 g/L ammonium oxalate. Both solutions are heated to ~95 °C, and samples are soaked for 5 minutes in each, rinsing between soaks and ultrasonically cleaning after each iteration. The process is repeated until all oxide was visibly removed and was found to have a minor effect on surface feature height, causing only a 17 ± 33 nm variation for features in the height range 300 ─ 3000 nm.

3 RESULTS

This section presents a summary of the results of the microstructural analysis, completed on the as-irradiated condition and multiple annealing conditions. The microstructural analysis includes the effect of annealing on the Vickers micro-hardness, dislocation loop size and density, solute cluster size and density, and the grain boundary segregation. Also reported here are results on irradiation hardening, CERT SCC tests, 4-point bend tests, crack growth rate tests, and associated fractography.

3.1 *Hardness*

Vickers micro-hardness has been often reported in the literature as a simple method to evaluate the bulk changes in the irradiated microstructure following PIA treatments, since a greater reduction in hardening has been observed to correspond to a greater removal of irradiation defects such as dislocation loops and solute clusters. As such, to select the specific annealing conditions for microstructure analysis, CERT and CGR experiments, a wide range of annealing temperatures and times were applied to the as-received sample blanks listed in Table 2-6.

Four different temperatures: 450°C, 500°C, 550°C, and 600°C with times: 1, 5, and 20 hr at each temperature were utilized, as these time/temperature combinations were expected to fully bound the partial and complete removal of irradiation hardening. The hardness measurements for the selected temperatures are shown in Table 3-1 and Figure 3-1, where the remaining irradiation hardening is plotted as a percentage of the as-irradiated condition. In this report the iron diffusion distance, d, was calculated using the parameters of Fukuya et al. [18]: $d = \sqrt{Dt}$, where t is the annealing time and D the iron self-diffusion coefficient given by $D = D_o e^{-Q/kT}$, where T is the annealing temperature, k is Boltzmann's constant, Q is the migration energy of 2.95 eV, and D_o equals 4.9 x 10^5 m^2/s [18].

Table 3-1: Change in the as-irradiated hardness due to specific annealing treatments. Overall the hardness was seen to decrease with increasing temperature and time. The irradiation hardening was determined using a value of H_v = 157.95 for the hardness of unirradiated 304L stainless steel.

Sample Blank ID	PIA treatment	As-Irradiated Hardness (H_v)	PIA Hardness (H_v)	Irradiation Hardening (H_v)	Post-PIA Irradiation Hardening (H_v)	% of As-Irradiated Hardening
17	600C: 1hr	371.67	228.95	213.71	71.00	33.22
17A	600C: 5hr	371.67	185.38	213.71	27.43	12.83
9	450C: 5hr	341.50	310.42	183.55	152.48	83.07
9A	450C: 1hr	341.50	329.09	183.55	171.14	93.24
18	500C: 1hr	334.75	321.00	176.80	163.05	92.22
18A	500C: 5hr	334.75	304.81	176.80	146.86	83.07
16	500C: 20hr	350.33	286.61	192.38	128.67	66.88
16A	600C: 5hr	350.33	184.61	192.38	26.67	13.86
11	550C: 1hr	341.67	287.28	183.71	129.33	70.40
11A	600C: 20hr	341.67	150.42	183.71	-7.52	-4.10
5	500C: 1hr	339.75	308.05	181.80	150.10	82.56
5A	450C: 20hr	339.75	309.81	181.80	151.86	83.53
15	550C: 5hr	337.42	248.28	179.46	90.33	50.33
15A	550C: 20hr	337.42	220.19	179.46	62.24	34.68

The irradiation hardening ($\Delta H_{v,\,Irr}$), is the increase in the hardness due to the presence of irradiation defects and is calculated from the following expression:

$$\Delta H_{v,Irr} = H_{v,Irr} - H_{v,Unirr} \, , \tag{3.1}$$

where $H_{v,Irr}$ is the measured hardness of the as-irradiated 304L stainless steel, and $H_{v,Unirr}$ is the measured hardness of the unirradiated 304L stainless steel. As no archive material is available, the hardness of the unirradiated materials was assumed to be that of a 304L stainless steel, which was measured as 157.95 H_v. Similarly, the post-PIA irradiation hardening ($\Delta H_{v,\,PIA}$) can be calculated via equation 3.1, where the measured hardness after PIA ($H_{v,\,PIA}$) is substituted for the as-irradiated measurement ($H_{v,\,Irr}$). The percentage of as-irradiated hardening remaining is then calculated as:

$$\% \text{ of as} - \text{irradiated hardening} = \frac{\Delta H_{v,PIA}}{\Delta H_{v,Irr}} \; . \tag{3.2}$$

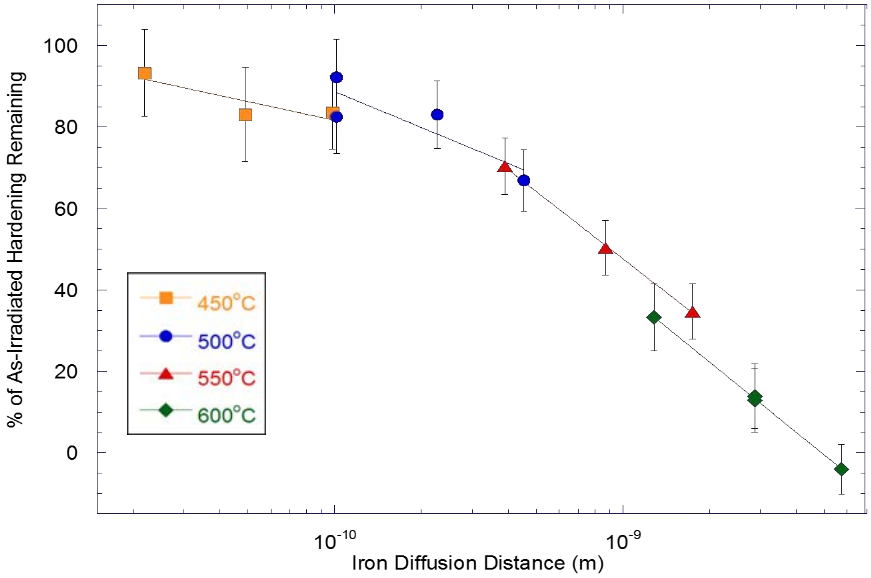

Figure 3-1: Change in the residual irradiation hardening due to specific annealing treatments.

Overall, it was observed that annealing at 450ºC, had a negligible impact on the irradiation hardening up to times of 20 hours. However, temperatures of 500ºC, 550ºC, and 600ºC showed successively greater removal of hardening with increasing time and temperature. Following annealing at 600ºC:20hr, the measured hardness had returned to a value expected for an unirradiated 304L stainless steel.

Using the criterion outlined in previous quarterly reports, annealing conditions of 500ºC: 1hr, 550ºC: 1hr, 550ºC: 5hr, and 550ºC: 20hr, were selected for both more detailed microstructural analysis and application to the CERT and CGR specimens. Following the annealing of the CERT and CGR samples, small slices from the tensile heads were used to confirm the removal of hardness. The results for these slices was outlined in previous reports, but there was a good agreement in hardening removal as compared to the data in Table 3-1.

3.2 *Irradiated Microstructure*

3.2.1 Dislocation Loops

The faulted dislocation loops in the as-irradiated 304L SS and after PIA at 500°C: 1hr, 550°C:1 and 5hr were characterized using rel-rod dark field technique. TEM images of dislocation loops are shown in Figure 3-2. Dislocation loops were confirmed in all examined PIA conditions. However, annealing at 550°C: 20hr resulted in a low density of large loops. Because of the very low density of loops, rel-rods could not be observed and dislocation loops were imaged in bright field under a two-beam condition. In addition to loops, stacking fault tetrahedral were observed as shown in the insert of Figure 3-3.

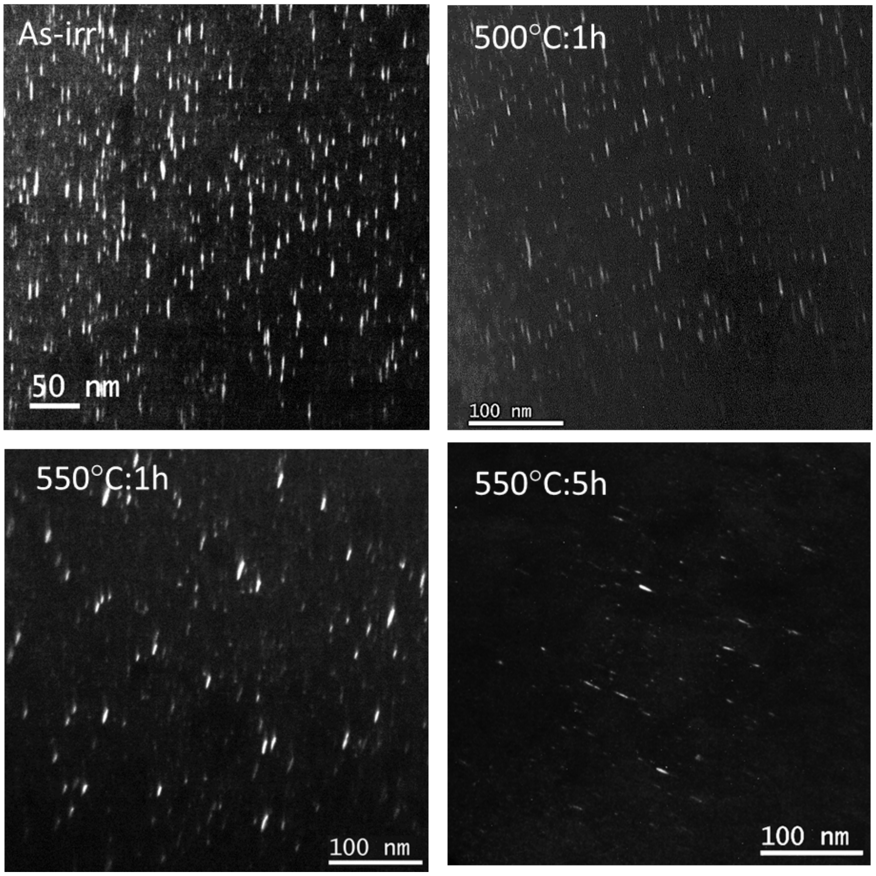

Figure 3-2: Rel-rod dark field TEM image showing the faulted dislocation loops in 304L SS irradiated to 5.9 dpa in BWR after various post-irradiation annealing conditions.

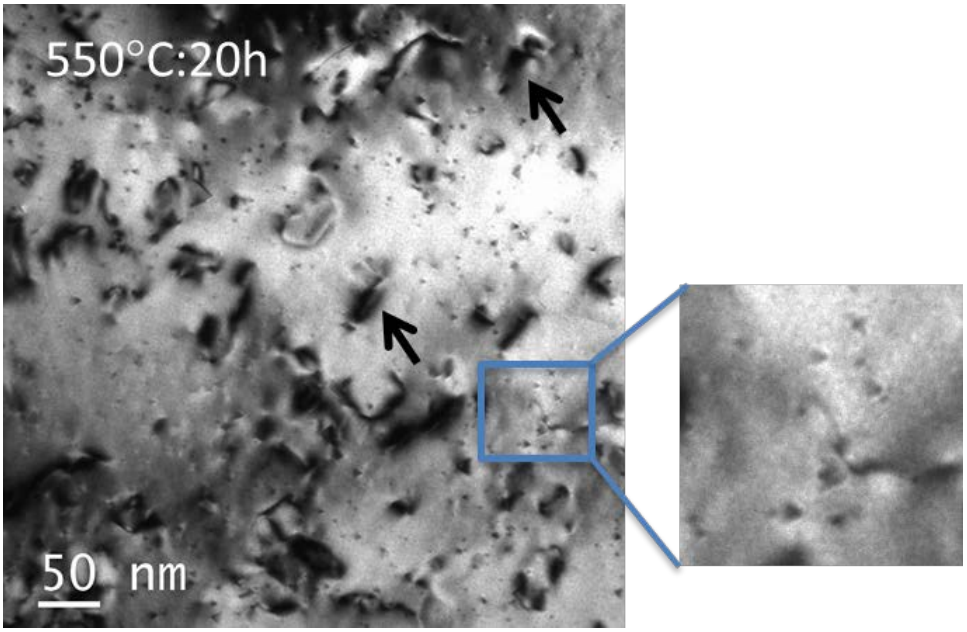

Figure 3-3: Dislocation loops (as indicated by arrows) and small stacking fault tetrahedral (as shown in the insert) in 304L SS after post-irradiation annealing at 550°C for 20 hours.

The average dislocation loop diameter and number density in 304L SS irradiated to 5.9 dpa in BWR and after various post-irradiation annealing conditions are given in Table 3-2. The initial average dislocation loop diameter after irradiation was 8.3 nm and it was 9.6 nm after PIA at 500°C: 1hr. The average loop size was 8.9 nm and 8.0 nm after PIA at 550°C: 1hr and 5hr, respectively. The comparison of loop size at different annealing conditions is shown in Figure 3-4. The dislocation loop sizes are virtually the same after annealing at 550°C for 5h. Significant increase in dislocation loop size was observed after 550°C for 20h, in which the loop size was about 26 nm. The loop density reduced significantly from 1.1×10^{23} m^{-3} at the as-irradiated condition to 8.2×10^{22} m^{-3} after annealing at 500°C: 1hr, to 3.2×10^{22} m^{-3} at 550°C: 1hr, to 1.3×10^{22} m^{-3} at 550°C: 5hr. The number density became negligible after annealing at 550°C: 20hr compared to the number density in the as-irradiated condition. In other words, the loop density reduced to ~3/4 of its initial density after PIA at 500°C: 1hr and to ~1/10 after PIA at 550°C: 5hr. Post-irradiation annealing at 550°C for 20 hours resulted in low number density of large loops.

The size distribution of dislocation loops in 304L SS irradiated to 5.9 dpa at in BWR environment and after various post-irradiation annealing conditions is shown in Figure 3-4b. It appears that smaller dislocation loops are preferably annealed out at the 500°C for 1hr condition and in fact, the density of large loops (>13nm) shows increase in population compared to the as-irradiated condition. However, this is not observed for annealing at 550°C condition, in which the dislocation density decreases across the whole size spectrum.

Table 3-2: Dislocation loop size, number density in 304L SS irradiated to 5.9 dpa in BWR and after various post-irradiation annealing conditions.

Condition	Number Density (m^{-3})	% of As-Irradiated Density	Average Diameter (nm)
As-Irradiated	11.1×10^{22}	100%	8.3
500˚C: 1 hr	8.21×10^{22}	74.0%	9.6
550˚C: 1 hr	3.25×10^{22}	29.3%	8.9
550˚C: 5 hr	1.27×10^{22}	11.4%	8.0
550˚C: 20 hr	0.05×10^{22}	0.4%	26

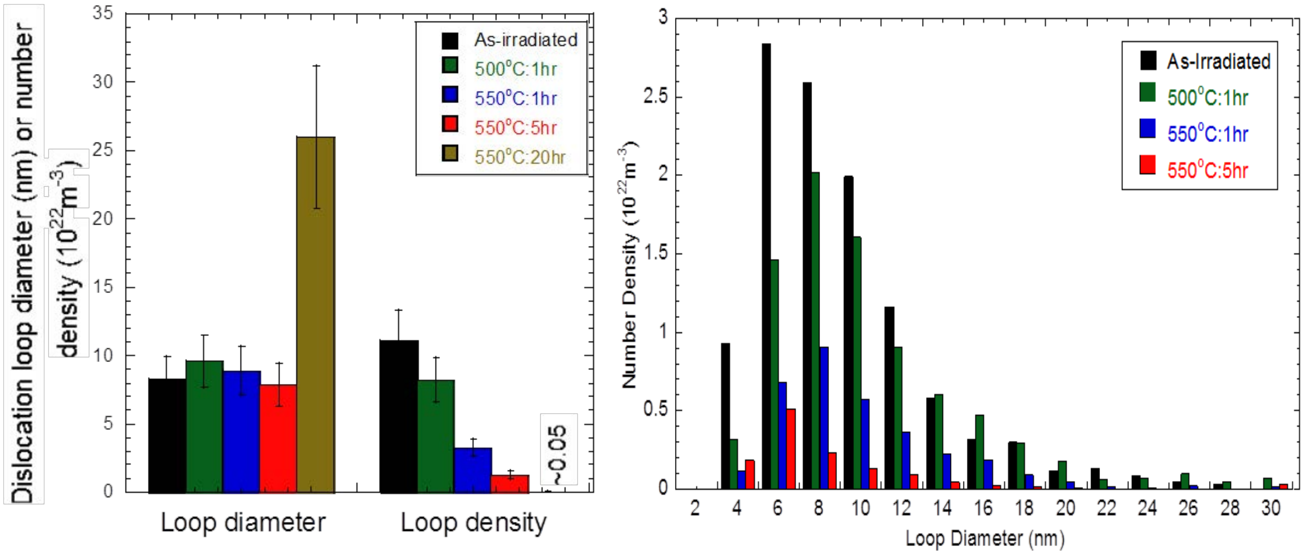

a

b

Figure 3-4: Comparison of (a) size and number density, and (b) size distribution of faulted dislocation loops in 304L SS irradiated to 5.9 dpa in BWR and after various post-irradiation annealing conditions.

3.2.2 Solute Clusters

Two types of solute clusters were observed by APT in the 304L SS irradiated to 5.9 dpa in the BWR; Ni-Si rich clusters and Al-Cu rich clusters. The APT reconstructions are shown in Figure 3-5 for the as-irradiated condition. Evolution of the Ni-Si and Al-Cu clusters after PIA is shown in Figure 3-6 and the number density, diameter, Ni-Si or Al-Cu ratio and volume fraction for Ni-Si and Al-Cu clusters are given in Table 3-3 and Table 3-4, respectively. The Ni-Si clusters are mainly precursors of the γ' or G phase as the concentrations of Ni and Si have not reached that for phase formation (75% Ni and 25%Si). The number density in the as-irradiated condition is 3.88×10^{23} m^{-3} and decreases to 2.83×10^{23} m^{-3} after PIA at 500°C: 1hr and to 2.35×10^{23} m^{-3} after PIA at 550°C:1hr. The density further decreases to 0.7×10^{23} m^{-3} after annealing at 550°C:20hr, at which point only about 18% of the as-irradiated number density remain. The cluster size, however, increases from about 9 nm at the as-irradiated condition to 20 nm after annealing at 550°C:20hr. Due to the increase in the cluster size the volume fraction does not change significantly after annealing: ~2.5% in the as-irradiated condition and ~3.0% after annealing at 550°C:20hr.

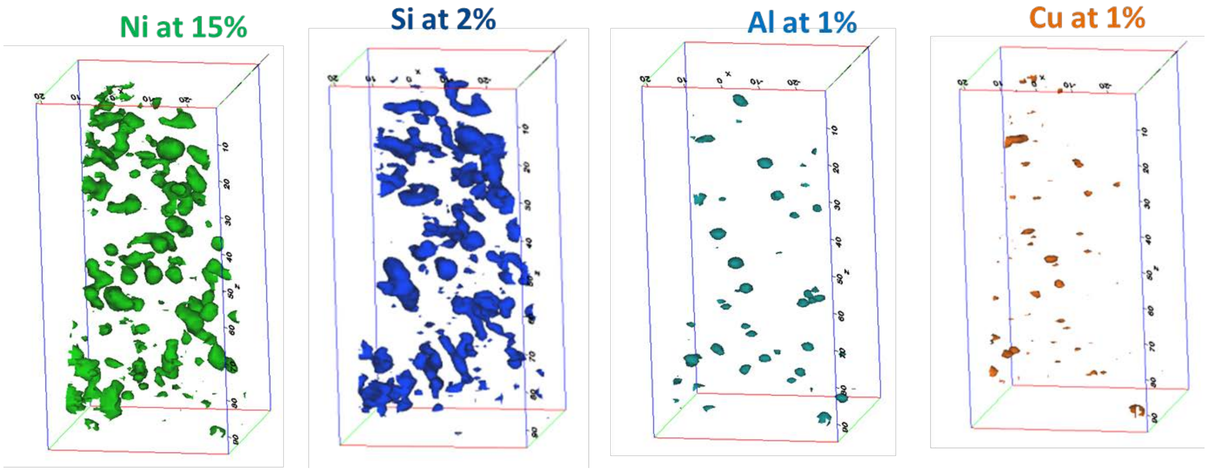

Figure 3-5: Ni-Si and Al-Cu clusters as observed in 304L SS irradiated to 5.9 dpa in BWR. Clusters are shown using isoconcentration surface plots from APT atom maps.

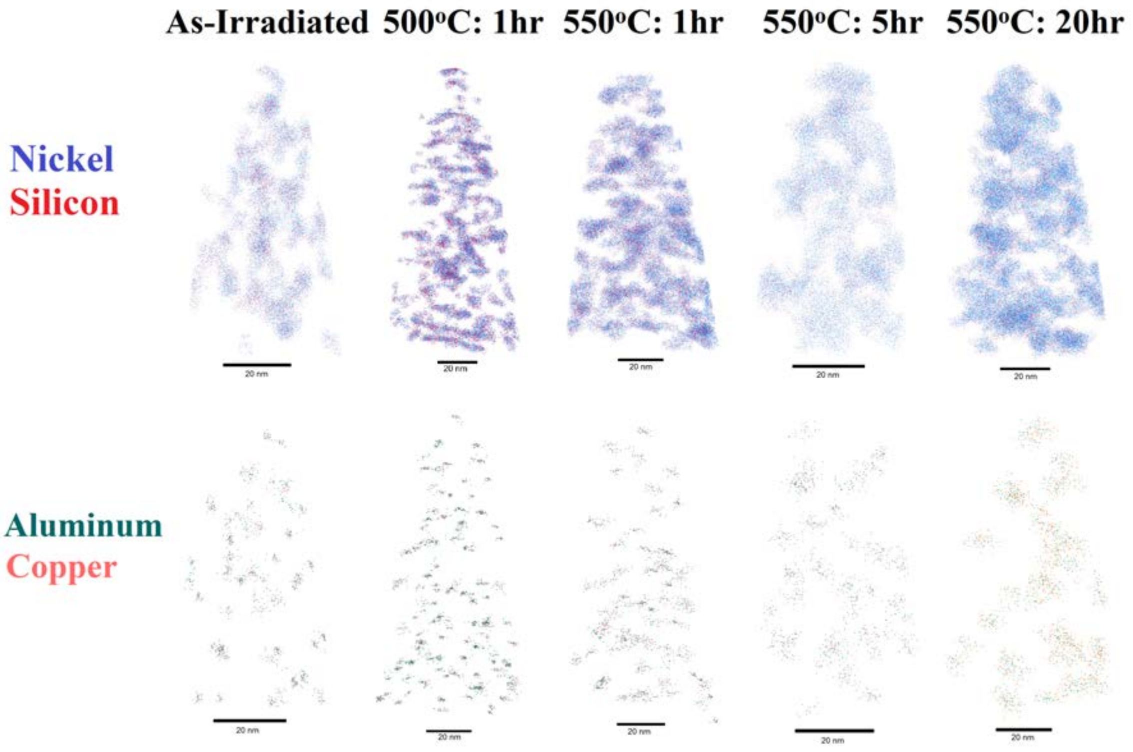

Figure 3-6: Evolution of Ni-Si and Al-Cu clusters in 304L SS irradiated to 5.9 dpa in BWR after various post-irradiation annealing conditions.

Table 3-3: Ni-Si cluster size, density and volume fraction in 304L SS irradiated to 5.9 dpa in BWR and after various post-irradiation annealing conditions.

Condition	Density (10^{23} /m^3)	% of As-Irradiated	Diameter (nm)	Ni-Si Ratio	Volume Fraction (%)
As-Irradiated	3.88 ± 0.59	100%	9.24 ± 0.71	5.13 ± 0.13	2.47 ± 0.08
500^{o}C: 1 hr	2.83 ± 0.46	72.8%	10.79 ± 0.90	5.12 ± 0.48	2.44 ± 0.21
550^{o}C: 1 hr	2.35 ± 0.11	60.5%	12.34 ± 0.09	5.43 ± 0.27	2.97 ± 0.05
550^{o}C: 5 hr	1.21 ± 0.47	31.2%	18.09 ± 4.68	7.61 ± 0.59	3.59 ± 0.91
550^{o}C: 20 hr	0.70 ± 0.07	18.0%	20.23 ± 1.43	7.95 ± 0.03	2.96 ± 0.16

Table 3-4: Al-Cu cluster size, density and volume fraction in 304L SS irradiated to 5.9 dpa in BWR and after various post-irradiation annealing conditions.

Condition	Density (10^{23} /m^3)	% of As-irradiated	Diameter (nm)	Al-Cu Ratio	Volume Fraction of Al (%)
As-Irradiated	2.92 ± 0.20	100%	5.68 ± 0.56	2.13 ± 0.60	0.035 ± 0.006
500^{o}C: 1 hr	2.46 ± 0.10	84.4%	6.19 ± 0.36	2.20 ± 0.06	0.027 ± 0.003
550^{o}C: 1 hr	1.57 ± 0.11	53.8%	9.54 ± 0.66	1.19 ± 0.05	0.021 ± 0.002
550^{o}C: 5 hr	2.61 ± 0.47	89.4%	11.00 ± 0.63	1.14 ± 0.08	0.041 ± 0.006
550^{o}C: 20 hr	0.93 ± 0.26	31.8%	13.15 ± 1.16	0.69 ± 0.02	0.016 ± 0.001

The Al-Cu shows the same trend as Ni-Si cluster after annealing. The number density in the as-irradiated condition is 2.92×10^{23} m^{-3} and it decreases to 2.46×10^{23} m^{-3} after PIA at 500°C: 1hr and to 1.57×10^{23} m^{-3} after PIA at 550°C: 1hr. The density further decreases to 0.9×10^{23} m^{-3} after annealing at 550°C:20hr, which is ~32% of the as-irradiated number density. The cluster size, increases from ~6 nm at the as-irradiated condition to ~13 nm after annealing at 550°C: 20hr. The volume fraction of Al-Cu clusters is rather small, ~0.035% in the as-irradiated condition and ~0.016% after annealing at 550°C: 20hr.

3.2.3 Grain Boundary Segregation

Radiation-induced segregation was examined in 304L SS in the as-irradiated condition and PIA at 550°C for 5 and 20 hours. Figure 3-7 and Figure 3-8 are the elemental images showing segregation of Cr, Ni and Si at the grain boundary in the as-irradiated and PIA at 550°C:20h condition, respectively. Depletion of Cr, Fe and enrichment of Ni, Si and P are evident from composition profile across the grain boundary in the as-irradiated condition (Figure 3-7).

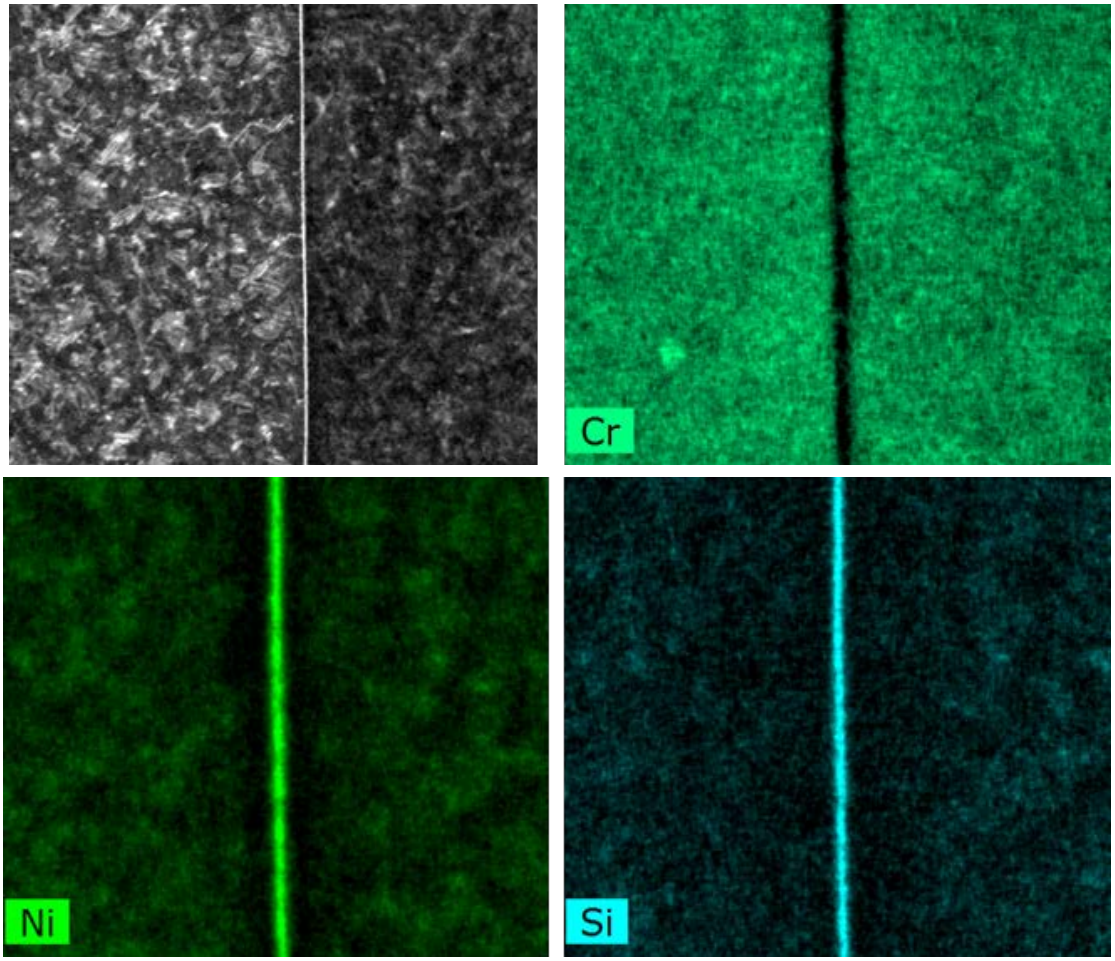

Figure 3-7: Radiation-induced segregation in 304L SS irradiated to 5.9 dpa in BWR as revealed by the composition maps from the TALOS. Depletion of Cr and enrichment of Ni and Si are evident.

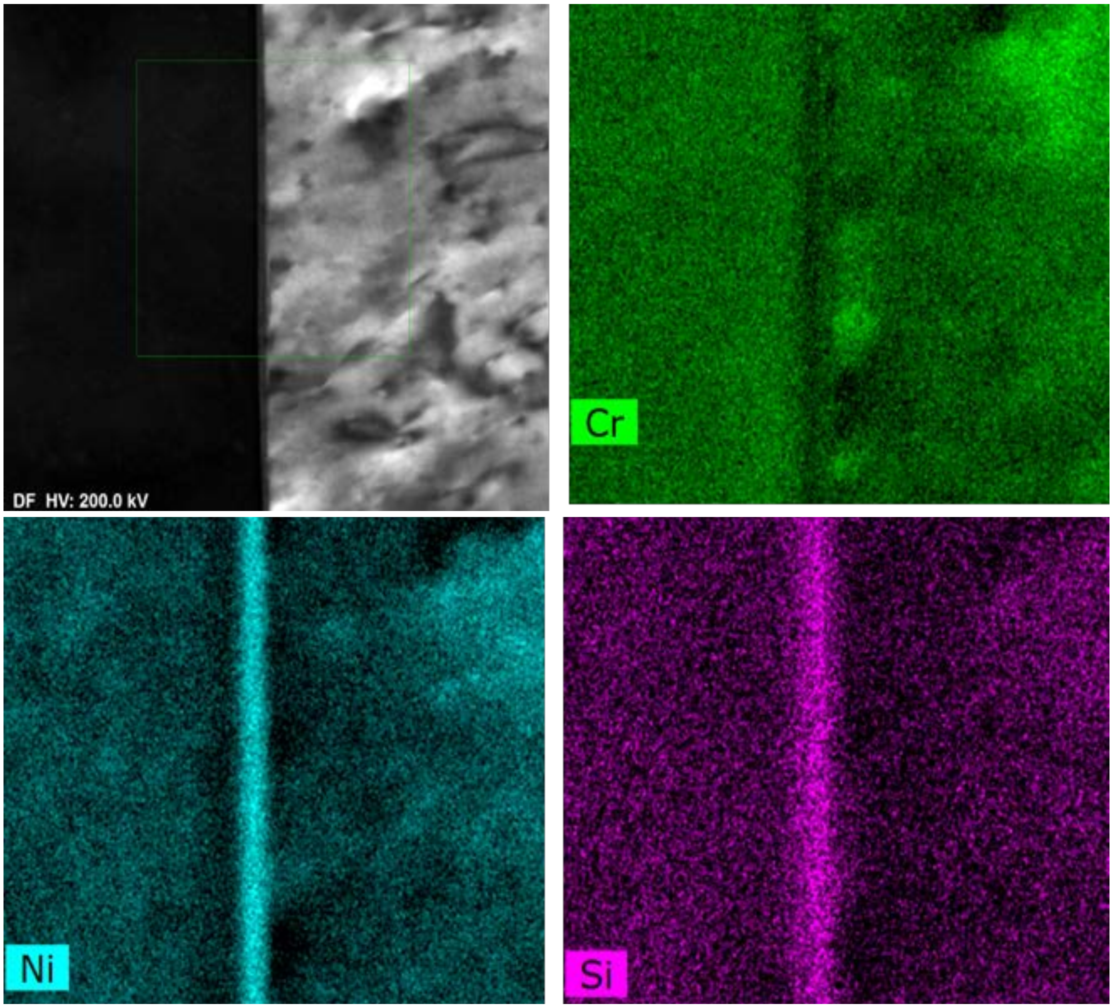

Figure 3-8: Radiation-induced segregation in 304L SS irradiated to 5.9 dpa in BWR and post-irradiation annealing at 550°C for 20 hr as revealed by the composition maps from the TALOS. Depletion of Cr and enrichment of Ni and Si are still evident.

In the as-irradiated condition, the depletion of Cr is about 5.5% and the enrichment of Ni and Si are 13.4% and 2.2% respectively (Table 3-5). The depletion of Cr decreases to 3.2% after annealing at 550°C:5h and 1.4% after annealing at 550°C:20h. Enrichment of Ni drops to ~3.2% after annealing at 550°C:20h, which corresponds to 23% of Ni enrichment in the as-irradiated condition. There is only 0.13% of enrichment of Si at the grain boundary after annealing at 550°C:20h, which is ~6% of the Si enrichment at the as-irradiated condition.

Composition profiles for Cr, Ni, Si and P for the as-irradiated and 550°C PIA conditions are shown in Figure 3-9 and 3-10. Besides the recovery of the segregated elements by thermal annealing, the segregated peaks appear to broaden after annealing.

Table 3-5: Grain boundary concentrations in the as-irradiated condition and after PIA at 550°C for 5 and 20 hours.

	GB Cr (wt%)	ΔCr (wt%)	% of As-Irr ΔCr	GB Ni (wt%)	ΔNi (wt%)	% of As-Irr ΔNi	GB Si (wt%)	ΔSi (wt%)	% of As-Irr ΔSi
As-Irradiated	12.83	-5.52	100	23.98	13.41	100	2.48	2.18	100
550°C:5h	15.11	-3.24	59	14.7	4.13	31	0.65	0.35	16
550°C:20h	16.92	-1.43	26	13.72	3.15	23	0.43	0.13	6

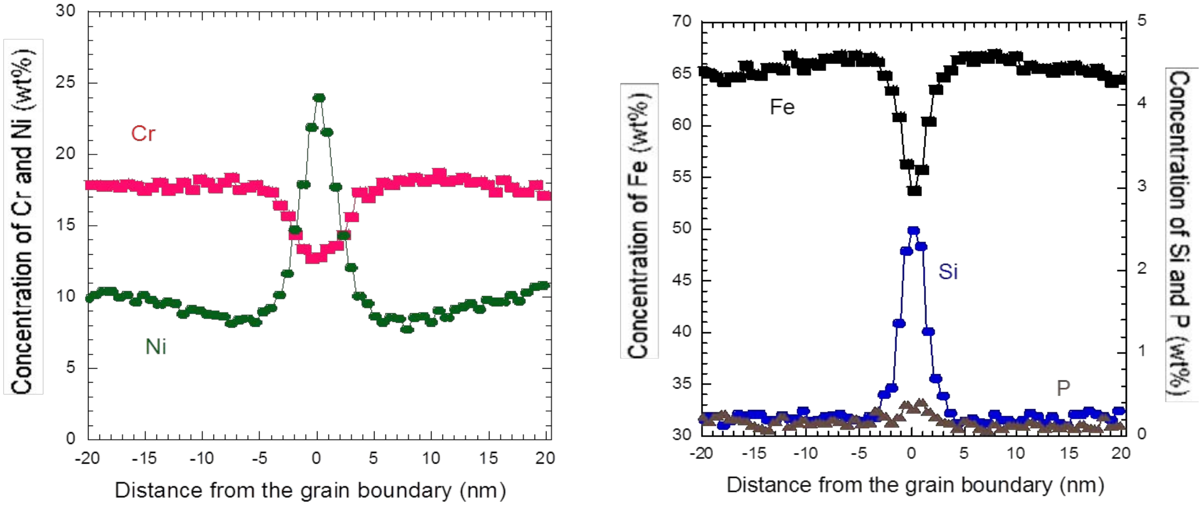

a

b

Figure 3-9: Composition profile across the grain boundary in 304L SS irradiated to 5.9 dpa in BWR for (a) Ni and Cr, and (b) Fe, Si and P.

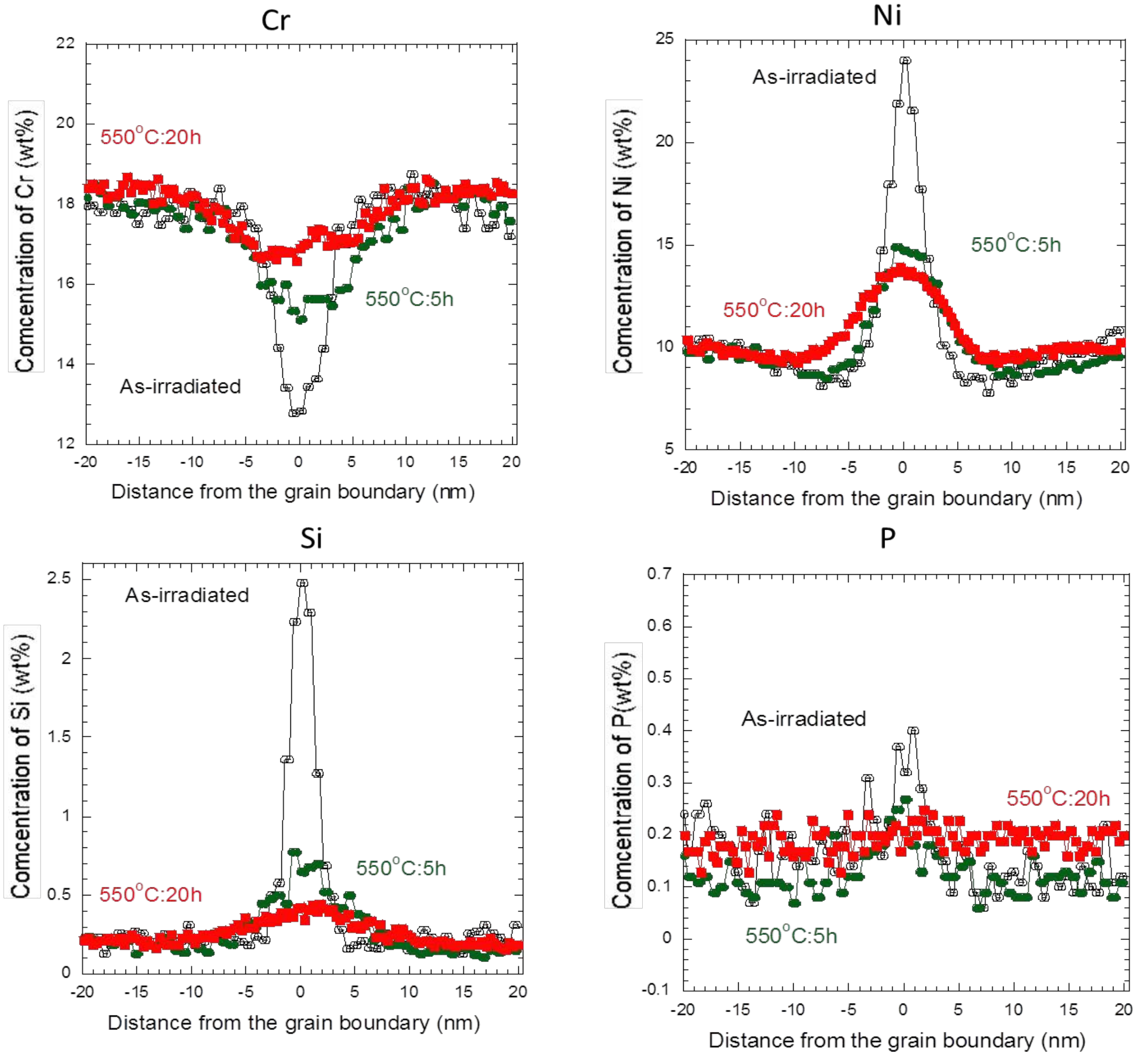

Figure 3-10: Effect of post-irradiation annealing on the segregation profiles of Cr, Ni Si and P in 304L SS irradiated to 5.9 dpa in BWR.

3.2.4 Overview of Microstructure of CIR Alloys

The microstructural characterization for the eleven alloys (four commercial purity and seven high purity alloys) was not carried out as part of this work. However, the microstructure for these materials has been previously characterized by different groups as part of the Cooperative IASCC Research (CIR) program and reported in Refs [19] and [20]. The microstructural details are reproduced here for reference purposes.

A summary of the franks loops and the precipitates observed in alloys A, B, C, E and H are summarized in Table 3-6 below. Frank Loops were observed in all the alloys and at the damage levels of the tensile bars used for the CERT studies (>5.5 dpa), the loop microstructure was observed to have reached saturation as shown by minimal change in the loop size and the loop density in these conditions. The loop size distribution for the different materials in the study are reproduced from the CIR report and are shown in Fig 3-11 below. The similar distribution profiles for the different alloys indicate that the loop microstructure for these alloys is similar in nature.

Table 3-6: Summary of Frank Loop and Precipitate Data in Alloy AS, B, C, ES and HS [19,20].

Alloy	Dose (dpa)	Frank Loops		Precipitates	
		Average Size (nm)	Density (10^{23} m^{-3})	Average Size (nm)	Density (10^{23} m^{-3})
Alloy AS	5.4	6	4.4		
	10.3	8	2	7.6	0.14
Alloy B	5.4	8	1.2		
	25	7.8	1.4	5.7	0.1
Alloy C	5.4	8.5	1.8		
Heat ES	10.3	6.1	4	5.8	0.14
Heat HS	10.3	8.9	1.4	5.2	0.24
Heat KS	9.9	9.2	0.8	5.2	0.12
Heat LS	9.9	11.4	0.47	5.9	0.09

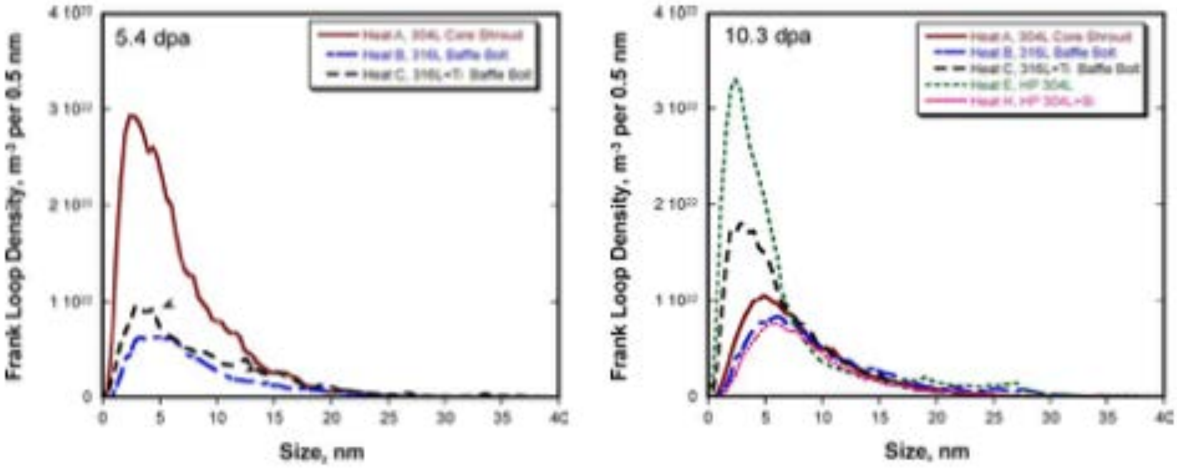

Figure 3-11: Frank loop size distributions for different heats at two damage levels of 5.4 dpa and 10.3 dpa. [19]

Precipitates were observed for alloy AS at a damage level of 10.3 dpa while they were absent at a damage level of 5.4 dpa. For alloy B, the precipitates were only found to be present at a damage level of 25 dpa and the size and number density was similar to those observed for alloy AS at 10.3 dpa. This indicates that the precipitation of γ' precipitates requires higher damage level for type 316 stainless steels compared to type 304 stainless steels. For alloy C (type 316 + Ti), no precipitates were observed in the CIR program for a damage level as high as 25 dpa.

For the high purity(HP) alloys, precipitates were observed in both the model alloy ES as well as the alloy modified using Si addition. The precipitate sizes were similar for both alloys at similar damage level of 10.3 dpa while the number density was higher for alloy HS which indicates that the addition of Si leads to preferential precipitation of γ’ precipitates in the material.

3.3 *Crack initiation in CERT tests on PIA conditions of blade material*

This section presents a description of the incremental CERT test results obtained from the irradiated and PIA tensile bars. CERT tests were conducted at 288°C under simulated BWR-NWC conditions. First of all, however, the strategy employed for identifying the appropriate stress levels at which to interrupt the incremental straining experiments is outlined.

3.3.1 Prediction of Yield Stress and Identification of Increments in Straining Experiments

Prior to beginning the incremental straining experiments, it was necessary to first predict the yield stress of both the as-irradiated condition and following each annealing treatment. Previous studies have shown that the change in irradiation hardening is linearly related to the change in the yield stress as seen in Equation 3.3 [21].

$$\Delta\sigma_y = X * \Delta H_v \tag{3.3}$$

Where X is the linear correlation factor; prior work by Busby *et al.* found that for irradiated austenitic stainless steels, an average correlation factor of X = 3.03, best fits the available data. However, the correlation factors for individual data sets had more variability, ranging from 2.63 to 3.83 [21]. Using the average correlation factor of 3.03 and the unirradiated hardness and yield stress of 157.95 H_v and 211.5 MPa, respectively, an initial prediction of the yield stress for our initial two specimens, T-4 (as-irradiated) and T-9 (550°C: 20 hr) were calculated based on the hardness measurements taken after PIA treatments, as shown in Table 3-7. Based on these predictions straining increments to 40, 60, 80, and 100% were made for these two specimens as listed in Table 3-8. The as-irradiated specimen T-4 showed a very close agreement between the predicted and measured yield stress. However, for the T-9 specimen, the actual hardness was originally incorrectly measured, thus resulting in a miscalculated yield stress prediction. As such, an additional stress increment was required to reach the correct yield stress. After remeasuring the hardness of the T-9 specimen, it was found to be much higher than originally expected, but the new value correctly matched the measured yield stress.

Utilizing these measured yield stresses a new correlation factor was fit to our specific material, which was then used to predict the yield stresses of the T-5 (500°C: 1hr), T-13 (550°C: 1hr), T-7 (550°C: 5hr), and T9 (550°C: 20hr) specimens. As shown in Figure 3-12, the final correlation factor for these five specimens was calculated as X = 2.47. While this correlation factor is lower than those previously seen in literature, the difference is likely an effect of the PIA treatments, as the previous correlation factors only examined as-irradiated microstructures [21]. Figure 3-13 shows a near prefect 1-to-1 comparison between the final predicted and measured yield stresses utilizing this fitted correlation factor.

Table 3-7: Prediction of the yield stress following PIA based on change in hardness.

Specimen	Measured Hardness (H_v)	Predicted Yield Stress (MPa)	Measured Yield Stress (MPa)
T-4 (As-Irradiated)	348.0 ± 9.6	681.3 ± 23.8	685.5
T-5 (500^{o}C: 1 hr)	326.9 ± 9.5	629.1 ± 23.5	633.4
T-13 (550^{o}C: 1 hr)	298.5 ± 13.9	558.9 ± 34.4	553.2
T-7 (550^{o}C: 5 hr)	266.7 ± 10.2	480.2 ± 25.2	483.6
T-9 (550^{o}C: 20 hr)	247.9 ± 14.2	433.7 ± 35.1	421.3

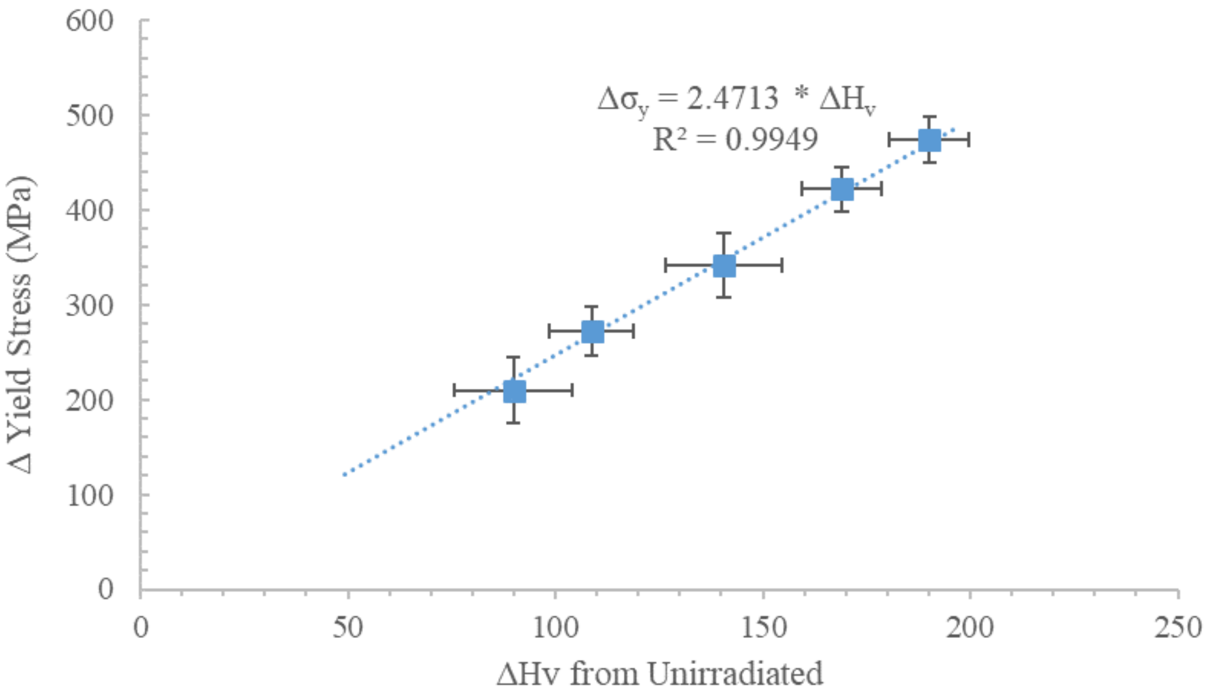

Figure 3-12: Comparison between the measured change in yield stress and the change in hardness from the base unirradiated condition (σ_y = 211.5 MPa, H_v = 157.95) used to predict the yield stress.

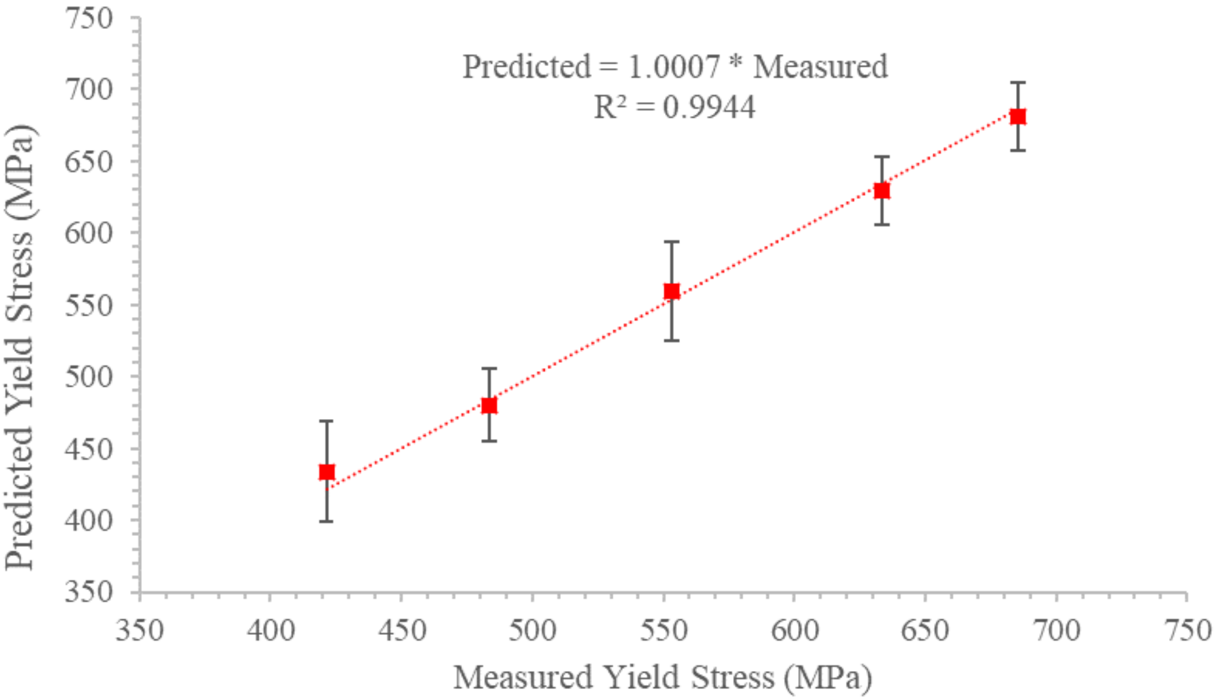

Figure 3-13: Comparison between the predicted yield stress values using a correlation factor of 2.47 and the measured values experimentally.

Table 3-8 shows a complete list of the incremental straining experiments that were applied to each of the examined specimens, including the target stress/strain for each increment as well as the final value. Overall, there was a good agreement between the target and achieved stress/strain, excluding the yield stress for specimen T-9 specimen and the 0.5% ε_p increment for the as-irradiated T-4 specimen. The T-7 increment to 10% ε_p was purposely halted early for examination due to the observed occurrence of significant necking.

Table 3-8: List of the tensile straining increments that were applied to the four tensile specimens tested for this project, including the maximum stress and plastic strain following each increment.

Specimen	Target value of stress or strain	Maximum Stress (MPa)	Fraction of Yield Stress (%)	Total Plastic Strain (%)
T-4 (As-Irradiated)	40% σ_y	270.6	39.5	0.00
	60% σ_y	401.5	58.6	0.00
	80% σ_y	539.5	78.7	0.00
	100% σ_y	685.5	100.0	0.13
	0.5% ε_p	682.8	99.6	0.74
	1.5% ε_p	657.2	95.9	1.51
	ε_f	328.5	47.9	2.00
T-5 (500°C: 1 hr)	80% σ_y	497.7	78.6	0.00
	100% σ_y	633.4	100.0	0.12
	1.0% ε_p	642.4	101.4	1.10
	1.5% ε_p	636.7	100.5	1.63
	2.0% ε_p	607.8	96.0	2.11
	ε_f	471.0	74.4	2.58
T-13 (550°C: 1 hr)	80% σ_y	446.0	80.6	0.00
	100% σ_y	553.2	100.0	0.08
	1.0% ε_p	555.1	100.3	1.07
	2.0% ε_p	558.6	101.0	2.05
	3.0% ε_p	564.0	102.0	3.11
	4.0% ε_p	565.8	102.3	4.07
	5.0% ε_p	571.1	103.2	5.10
	7.0% ε_p	569.2	102.9	7.19
	9.0% ε_p	557.7	100.8	9.35
	ε_f	515.8	93.2	11.61
T-7 (550°C: 5 hr)	80% σ_y	377.4	78.0	0.00
	100% σ_y	483.7	100.0	0.13
	2.0% ε_p	502.0	103.8	2.06
	4.0% ε_p	510.5	105.6	4.04
	6.0% ε_p	512.0	105.9	6.08
	10.0% ε_p	512.6	106.0	9.47
	ε_f	470.1	97.2	12.12
T-9 (550°C: 20 hr)	40% σ_y	130.8	31.0	0.00
	60% σ_y	196.2	46.6	0.00
	80% σ_y	261.6	62.1	0.00
	100% σ_y	341.1	81.0	0.00
	100% σ_y	415.6	98.6	0.08
	1.0% ε_p	437.7	103.9	1.06
	2.0% ε_p	454.4	107.9	2.02
	3.0% ε_p	463.6	110.0	3.00
	5.0% ε_p	478.6	113.6	5.00
	ε_f	491.5	116.7	11.43

3.3.2 Stress-Strain Behavior

Stress-strain curves for each of the tested conditions: as-irradiated, 500°C: 1 hr, 550°C: 1 hr, 550°C: 5 hr, and 550°C: 20 hr are shown in Figure 3-14. The elastic deformation portion of each curve has been corrected to subtract system compliance by normalizing to the expected Young's modulus for an austenitic stainless steel.

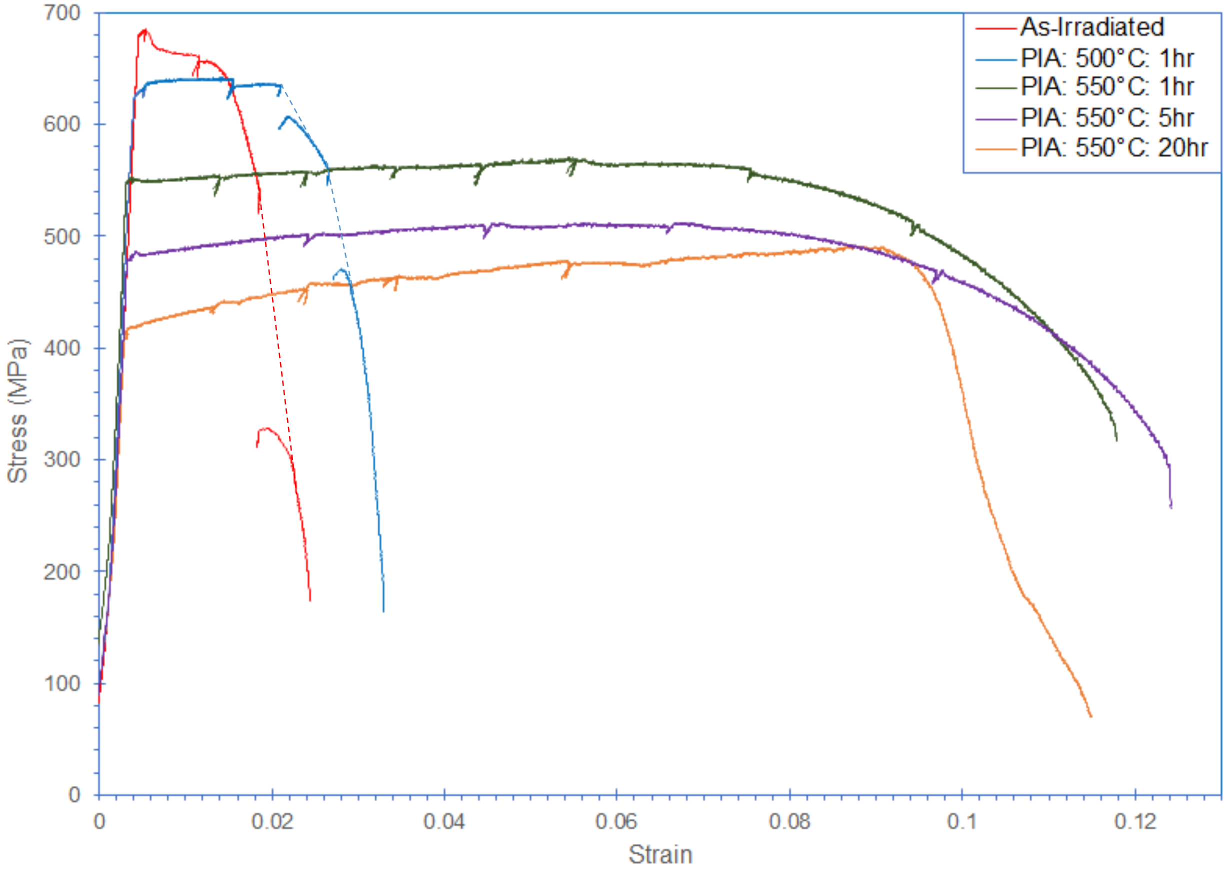

Figure 3-14: Change in the stress strain behavior because of specific annealing treatments: 500°C: 1hr, 550°C: 1hr, 550°C: 5hr, and 550°C: 20hr.

The as-irradiated condition displayed a yield stress drop and subsequent strain softening, as typical of the irradiated condition of a solution-annealed stainless steel. Annealing at 500°C:1 hr slightly reduced the yield stress, while completely removing the yield stress drop and strain softening behavior, introducing a very slight strain hardening behavior. Annealing at 550°C:1 and 5hr, further reduced the yield stress and resulted in a slight strain hardening behavior, with higher elongations and onset of necking at ~7% plastic strain. Annealing at 550°C:20 hr caused a further drop in the yield stress and an increase in the elongation. Furthermore, this condition displayed a clear strain hardening behavior, up to about 8.5% plastic strain.

3.3.3 Mechanical Properties

Mechanical properties after the varying annealing treatments, as determined from the CERT tests, are summarized in Table 3-9. The table is organized by annealing condition, showing the yield stress, maximum stress, uniform and total elongation. For the as-irradiated condition, uniform elongation and maximum stress both occurred at the yield point (~0.5%) because of strain softening.

Table 3-9: Change in the mechanical properties due to specific annealing treatments: 500°C: 1hr to 550°C: 20 hr.

Specimen	Yield Stress (MPa)	Maximum Stress (MPa)	Uniform Elongation (%)	Total Elongation (%)	Reduction in Area (%)
T-4 (As-Irradiated)	685.5	685.5	0.00	2.00	28.6
T-5 (500°C: 1 hr)	633.4	642.4	0.95	2.58	46.8
T-13 (550°C: 1 hr)	553.2	559.2	6.52	11.61	83.8
T-7 (550°C: 5 hr)	483.6	512.6	6.27	12.12	84.0
T-9 (550°C: 20 hr)	421.3	491.5	8.71	11.43	73.0

Overall, it was observed that the yield stress was reduced in proportion to the residual hardening following the annealing treatments. Furthermore, it was seen that the annealing treatments also lead to a change in the mechanical behavior, from a strain softening to strain hardening, and an increase in the ductility of the specimen. Reduction in area followed a similar trend as total elongation in that it increased with annealing, however, specimen T-5 (PIA 500°C) showed a much higher reduction in area as compared to T-4 (as-irradiated), despite an only slightly higher final elongation.

3.3.4 SCC Behavior

Following CERT testing, the fracture and gage surfaces were fully examined by SEM. Areas of IG or TG cracking were quantified to determine %IG, %TG, %mixed IG/TG, and %ductile failure. Examples of each type of fracture can be seen in Figure 3-15. Reduction in area was also determined based on the full area of the fracture surface. Each sample fracture surface is shown in Figure 3-16.

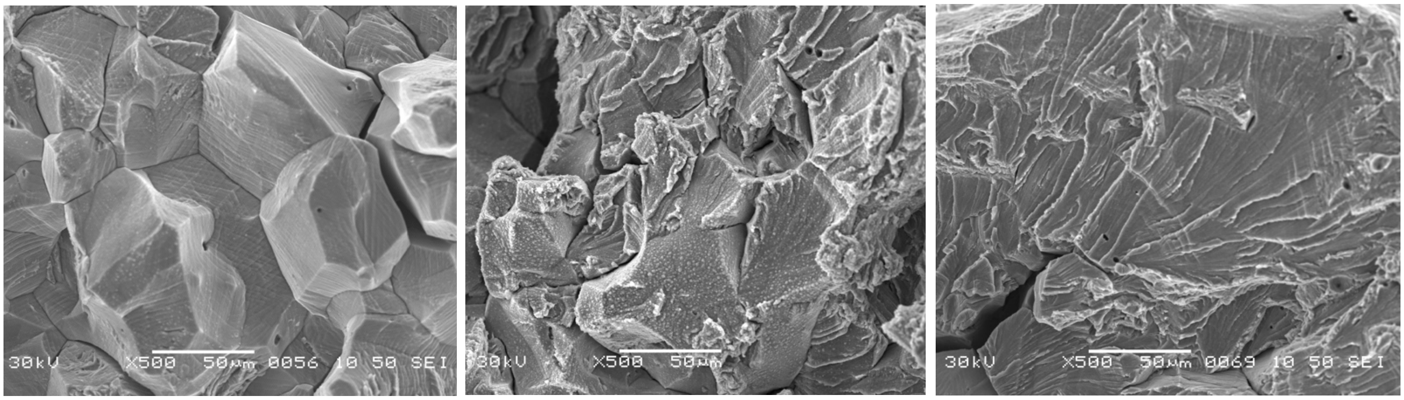

a b c

Figure 3-15: Example images from the T-5 (PIA 500^{o}C: 1hr) specimen of the three primary modes of failure that were observed during the crack growth of the as-irradiated and PIA specimens: a) intergranular, b) mixed intergranular-transgranular, c) transgranular.

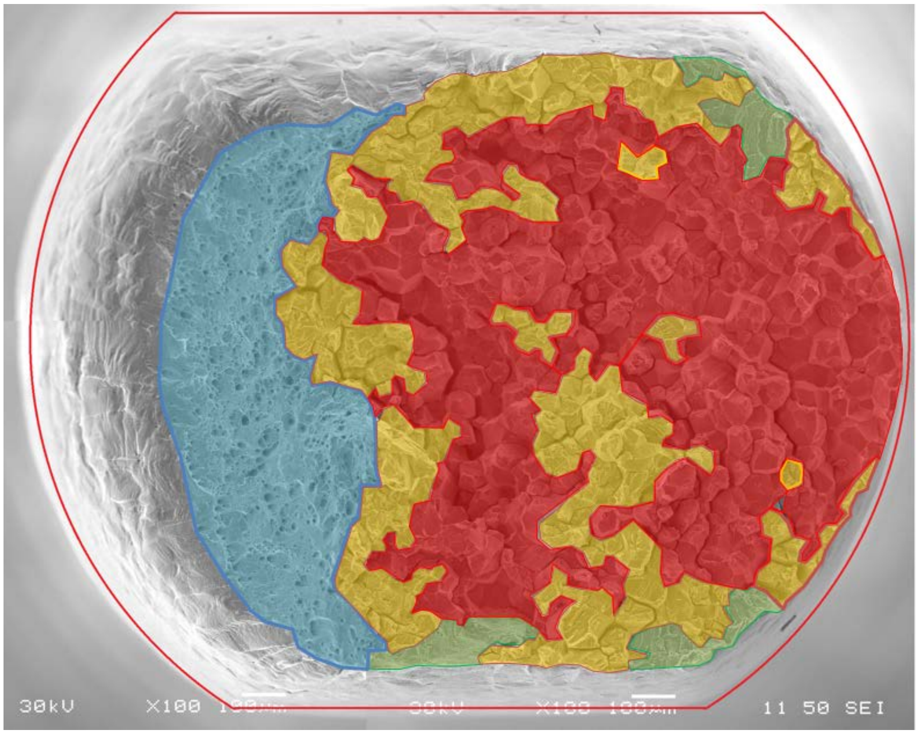

a

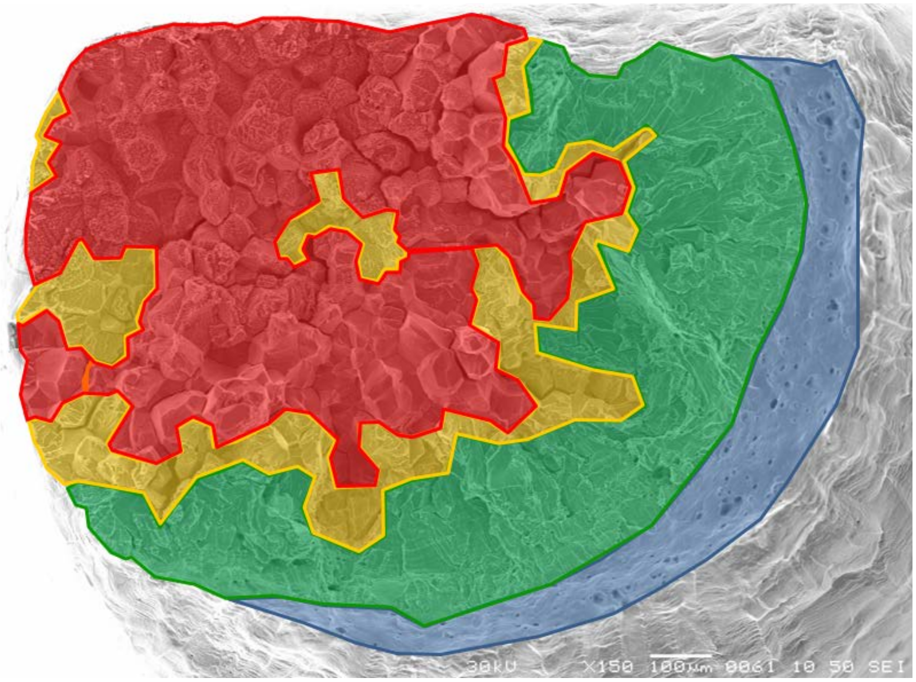

b

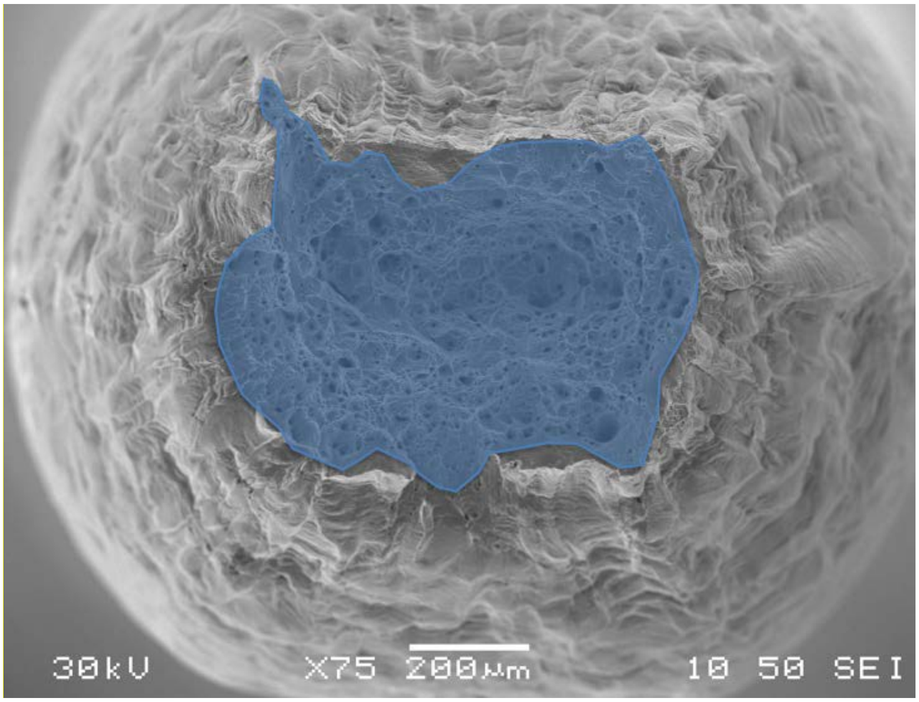

c

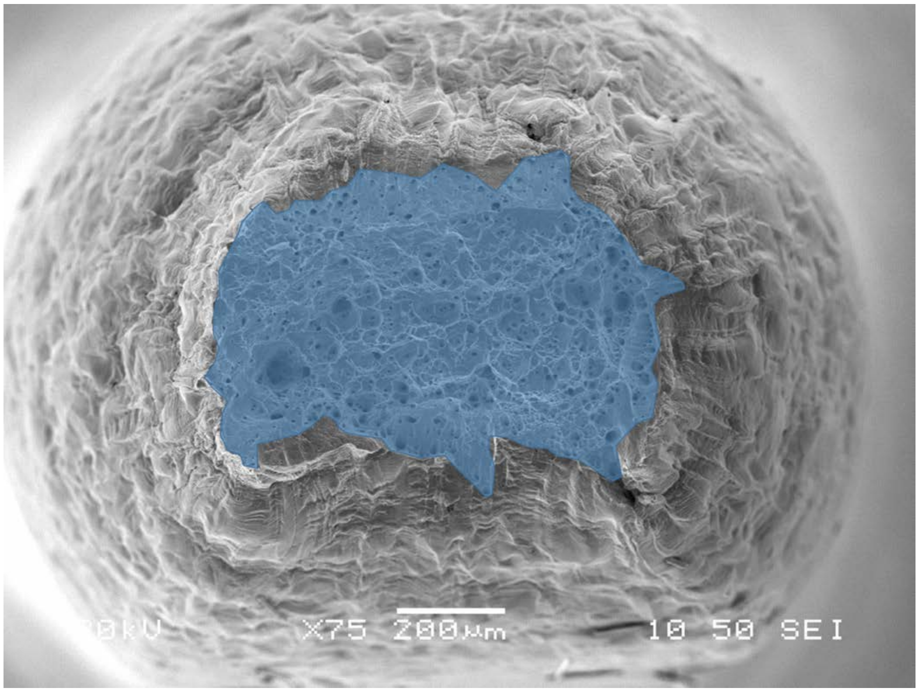

d

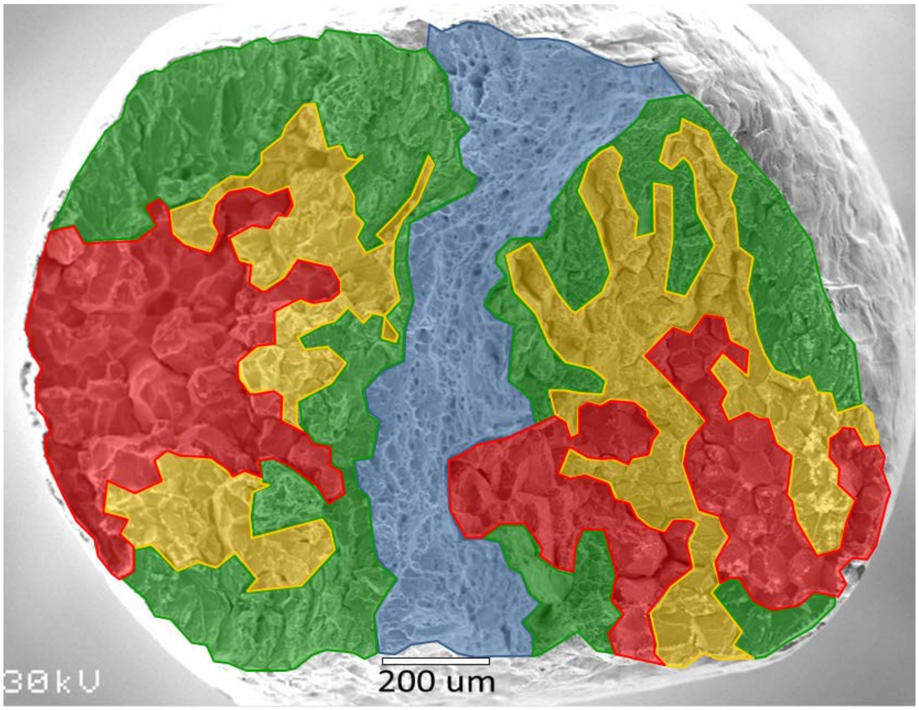

e

Figure 3-16: Comparison of the final fracture surface of the CERT tensile specimens: a) as-irradiated, b) PIA: 500°C: 1hr, c) PIA 550°C: 1hr, d) PIA 550°C: 5hr and e) PIA: 550°C: 20hr.

The results of the fractography classification and reduction of area analysis after CERT are summarized in Table 3-10 and Figure 3-17. The %IG varied between 48.4% and 0%, and was observed to largely decrease in response to increasing annealing time and temperature. However, while the IASCC susceptibility was fully removed for the 550°C: 1 and 5 hr annealed specimens, as evidenced by the fully ductile fracture surfaces, the 550°C: 20 hr specimen still displayed some residual IASCC susceptibility. It is worth noting that characterizing IASCC susceptibility by %IG produces a higher susceptibility for the 550°C: 20 hr condition than expected based on other results due to its unique failure. The T-9 tensile specimen initiated two cracks that grew from opposite sides of the tensile specimen slightly off plane from one another. After both cracks progressed through roughly 50% of the cross section, the specimen failed in shear between the two separate crack planes. As such, the final fracture cross section displays two independent crack fronts, which might account for the higher percentage of pure intergranular fracture.

Table 3-10: Change in the relative areas of fracture mode for the as-irradiated and PIA treatments: 500°C: 1hr and 550°C: 20 hr.

Specimen	%IG fracture	%Mixed fracture	%TG fracture	%Ductile fracture
T-4 (As-Irradiated)	48.40	28.62	3.62	19.41
T-5 (500°C: 1 hr)	34.86	12.82	36.58	15.74
T-13 (550°C: 1 hr)	0.00	0.00	0.00	100.00
T-7 (550°C: 5 hr)	0.00	0.00	0.00	100.00
T-9 (550°C: 20 hr)	20.60	25.04	35.28	19.08

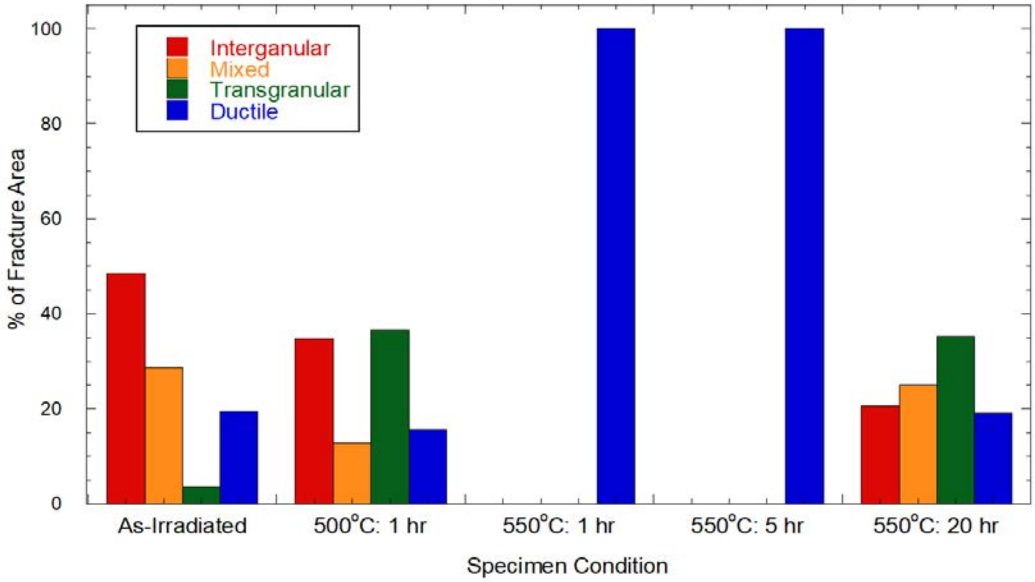

Figure 3-17: Change in the fracture morphology of the as-irradiated, PIA: 500°C: 1hr, PIA: 550°C: 1, 5, and 20 hr conditions.

3.3.5 Dislocation Channeling

As previously mentioned, the degree of localized deformation was measured via SEM following each stress/strain increment. However, due the highly strained region that occurs during the advancement of a crack tip, measurements of the dislocation channel density were only taken for increments which displayed no significant crack growth. Furthermore, the as-irradiated material displayed an unexpected resistance to localized deformation as significant populations of dislocation channels were only observed post-yield, following the addition of bulk plastic strain. Previous literature studies for irradiated material have observed significant localized deformation below the specimen yield stress [22-24].

The measured dislocation channel densities, grain boundary interaction site densities, and ratio of discontinuous to continuous interaction sites for each strain increment are shown in Table 3-11. As multiple specimens exhibited regions of enhanced strain, where the eventual crack initiation later occurred, the measured channel densities are averaged over this region (~1mm of gage length) where later crack initiation was observed, rather than over the entire gage length. Comparison of the dislocation channel density with strain for the examined conditions: as-irradiated, 500^{o}C: 1hr, 550^{o}C: 1, 5, and 20hr, is shown in Figure 3-18. The density of dislocation channel-grain boundary interaction sites is given in Figure 3-19, while the ratio of discontinuous to continuous interaction sites is presented in Figure 3-20.

It is observed that the as-irradiated, PIA: 500^{o}C: 1hr, and PIA: 550^{o}C: 1 hr conditions have very similar dislocation channel densities, while the 550^{o}C: 5 hr sample exhibited a decrease in the density. The 550^{o}C: 20hr had a significantly reduced density regardless of the plastic strain. The interaction site density seems to change in proportion to the total dislocation channel density regardless of the annealing condition.

Table 3-11: Change in the dislocation channel and interaction site densities in the failure region. A plastic strain of 0.00 corresponds to the density observed at the yield stress.

Specimen	Plastic Strain (%)	Channel Density (#/mm^2)	Continuous Site Density (#/mm^2)	Discontinuous Site Density (#/mm^2)	Discontinuous /Continuous site ratio
T-4 (As-Irradiated)	0.00	121 ± 19	21.2 ± 7.3	139 ± 22	6.5
	0.74	1337 ± 169	332 ± 67	1747 ± 229	5.3
T-5 (500^{o}C: 1 hr)	0.00	3.5 ± 2.9	0.0 ± 0.0	6.9 ± 5.8	-
	1.00	1903 ± 246	239 ± 99	3019 ± 424	12.7
	1.50	2462 ± 232	307 ± 78	3454 ± 553	11.2
	2.00	2718 ± 297	325± 116	4239 ± 553	13.1
T-13 (550^{o}C: 1 hr)	0.00	180 ± 48	42 ± 18	230 ± 66	5.5
	1.00	2448 ± 228	398 ± 68	3540 ± 520	8.9
	2.00	2602 ± 153	451 ± 51	3618 ± 225	8.0
	3.00	2737 ± 274	417 ± 48	4010 ± 446	9.6
	4.00	2869 ± 206	427 ± 95	4201 ± 306	9.8
	5.00	2856 ± 192	405 ± 65	4105 ± 296	10.1
	7.00*	5099 ± 344	765 ± 115	7365 ± 498	9.6
T-7 (550^{o}C: 5 hr)	0.00	99 ± 38	14 ± 12	151 ± 58	10.9
	2.00	2137 ± 220	262 ± 69	3289 ± 332	12.6
	4.00	2617 ± 376	405 ± 132	3891 ± 579	9.6
	6.00*	3657 ± 494	438 ± 79	5588 ± 736	12.8
T-9 (550^{o}C: 20 hr)	0.00	8.8 ± 5.5	0.0 ± 0.0	16 ± 10	-
	1.00	132 ± 46	21 ± 13	190 ± 61	9.1
	2.00	174 ± 76	44 ± 38	260 ± 81	5.9
	3.00	499 ± 115	100 ± 49	694 ± 132	6.9
	5.00	585 ± 136	107 ± 56	835 ± 156	7.8

*Specimens T-7 and T-13 were observed to neck at ~6% ε_p, thus the sharp increase in dislocation channel density is believed to be a direct result of the necking and does not actually represent a change in localized deformation with strain.

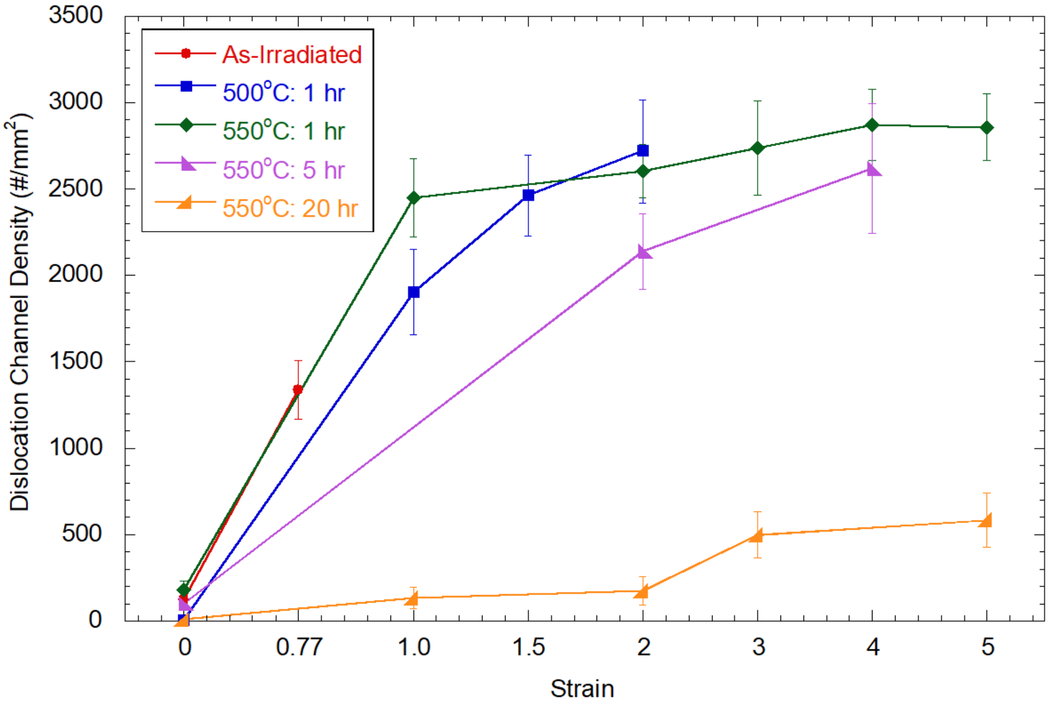

Figure 3-18: Change in the dislocation channel density of the failure region in response to increasing plastic strain, prior to crack growth or specimen necking.

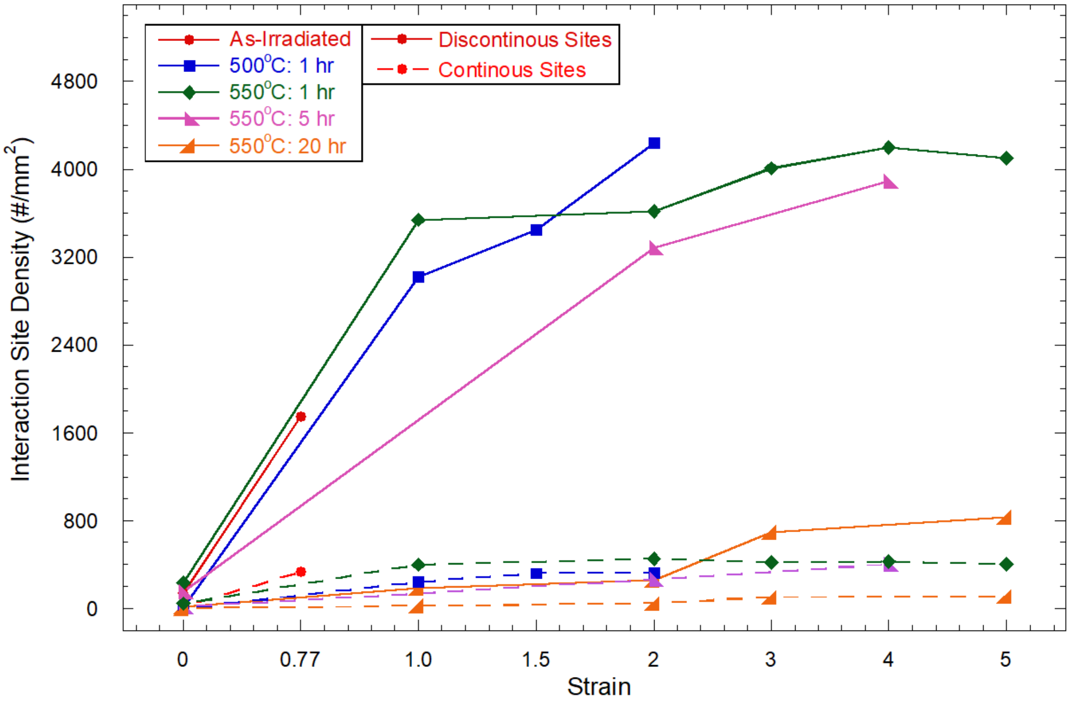

Figure 3-19: Change in the grain boundary-dislocation channel interaction site density of the failure region in response to increasing plastic strain.

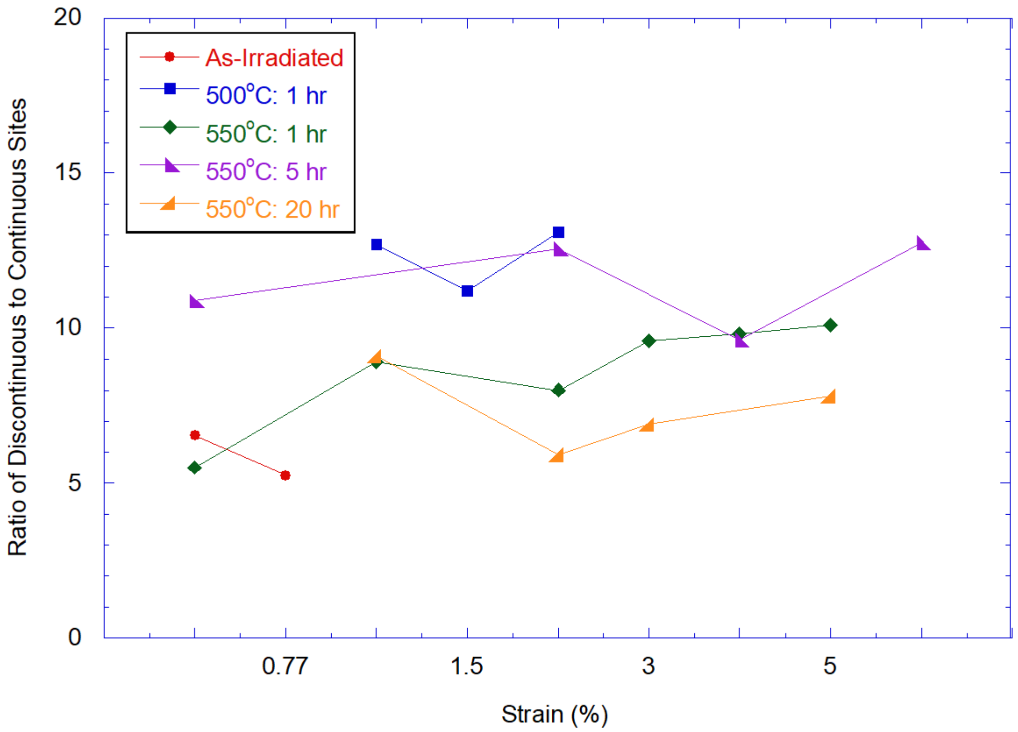

Figure 3-20: Change in the ratio of discontinuous to continuous grain boundary-dislocation channel interaction sites.

3.4 *Crack initiation in CERT tests on neutron-irradiated CIR alloys*

This section presents a summary of the CERT test results obtained from the BOR-60 irradiated tensile bars. CERT tests were conducted in one of three environments, 288°C BWR NWC, 288°C BWR HWC, or 320°C PWR PW, straining each sample until complete failure. The stress-strain curves of each sample are first presented with comments about the observed mechanical behavior. A summary of the mechanical properties is then presented followed by images of each fracture surface after completion of the CERT tests. More detailed information from each of the fracture surfaces and higher magnification images are presented in the appendices of previous semi-annual reports (January 2012, July 2012, January 2013, and July 2013). Finally, a summary of the fractographic analysis is presented.

3.4.1 Stress-Strain Curves

Stress-strain curves for each alloy are shown in Figure 3-21, Figure 3-22 and Figure 3-23 for samples tested in 288°C BWR NWC, 288°C BWR HWC, and 320°C PWR PW, respectively. The elastic deformation portion of each curve has been corrected to subtract system compliance, using the technique described in section 2.3.2.

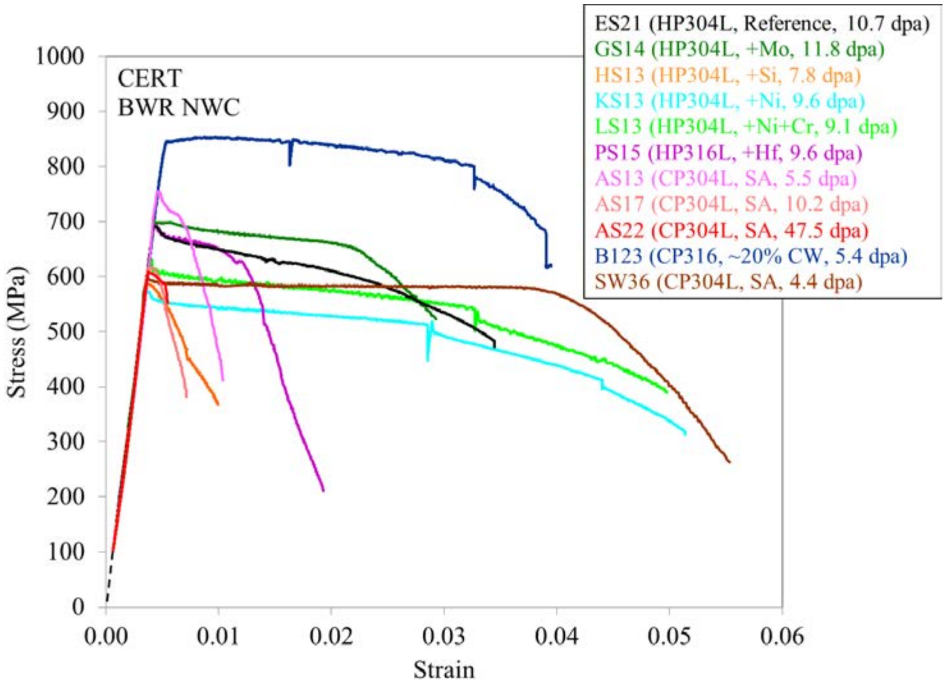

Figure 3-21: Stress-strain curves of neutron irradiated specimens tested in BWR NWC.

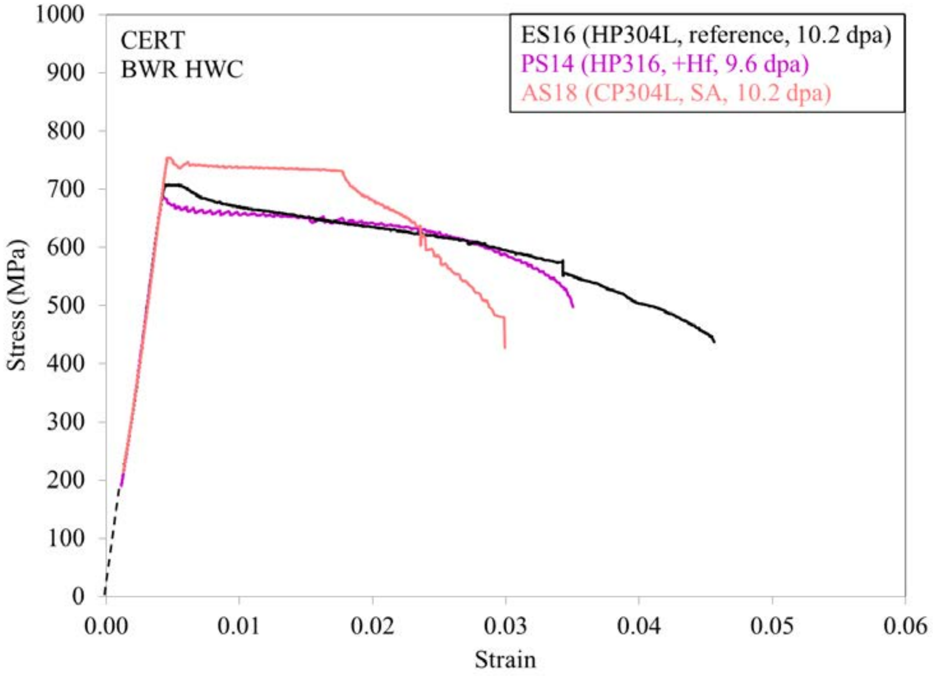

Figure 3-22: Stress-strain curves of neutron irradiated specimens tested in BWR HWC.

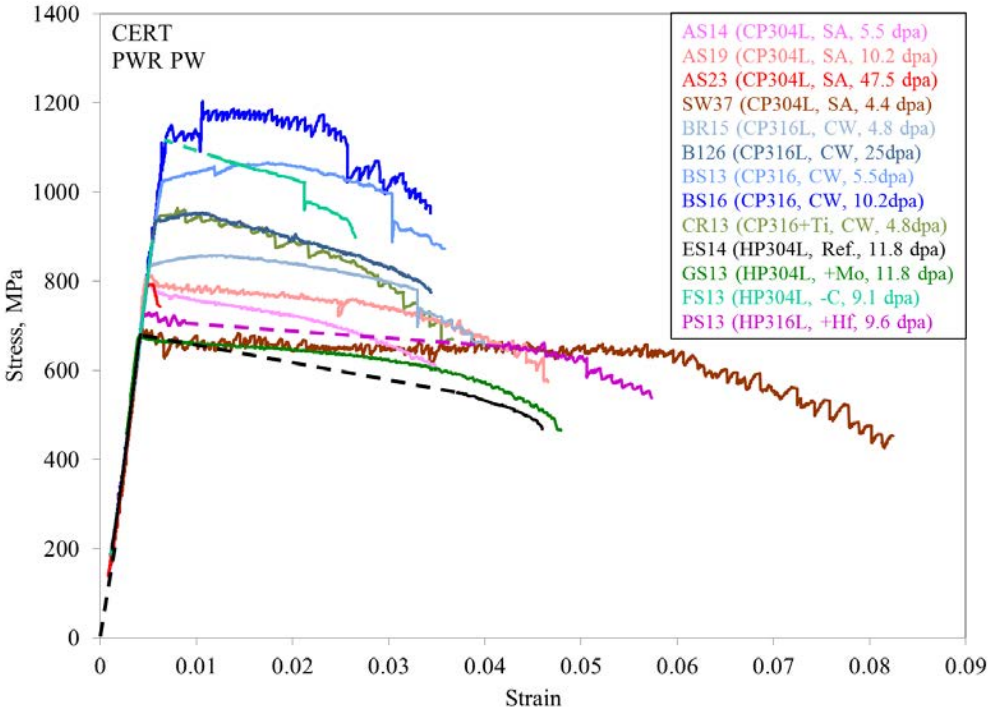

Figure 3-23: Stress-strain curves of neutron irradiated specimens tested in PWR PW.

All alloys that had been in the solution annealed condition prior to irradiation exhibited strain softening, therefore the yield stress equaled the maximum stress, and uniform elongation consisted of only elastic deformation. Also common to the solution annealed alloys was the observation of a sharp drop in stress upon yielding, likely caused by dislocation channeling [25]. When dislocation channeling starts to occur the local strain and strain rate in the channels greatly increases, rapidly removing barriers in the channels, thereby reducing the flow stress in the channels and allowing still more of the overall strain to be concentrated into the channels. In general, increasing irradiation dose caused an increase in YS for solution annealed alloys, with the exception of those with very high SCC susceptibility, which failed during elastic deformation and did not achieve their full expected YS (i.e., samples AS17, AS22, AS23, HS13).

All alloys in the cold worked condition prior to irradiation exhibited a small degree of strain hardening, even up to 25 dpa. None of the CW alloys exhibited a stress drop at the yield point, likely because of the dislocation barriers remaining from the cold work. Alloy BS had a higher degree of cold work than alloy BR or B, as the increased YS suggests. Increasing irradiation dose also caused an increase in YS for the cold worked alloys.

Solute addition alloys exhibited similar YS between ~600 and ~700 MPa, as expected due to the similar microstructures created prior to irradiation. Sample FS13 was the only exception, having a much higher yield stress than the other solute addition alloys. The YS and maximum stress of this sample were not recorded due to an error in data collection but were estimated to be 1140 MPa by extrapolating the stress-strain curve pre- and post- yield point. Regions where the gap in data exists due to the collection error for samples FS13, ES14, and PS13 are indicated by dashed lines in Figure 3-23. The high YS of sample FS13 implies that either the alloy was cold worked prior to irradiation or the irradiation dose was higher than the reported 9.1 dpa.

Substantial variations were observed in the elongation of the irradiated samples, but several trends were observed. In general, elongation was greater in environments with lower corrosion potential (samples had greater elongation in PW than in HWC, and both were greater than in NWC). The high purity solute addition alloys had generally greater elongation than the commercial purity alloys, although those with cold work had consistently intermediate elongations and little variation as a result of varying degree of cold work or irradiation dose. The only exception was alloy SW, which had very high elongation in both NWC and PW environments. The cause of the high elongation of alloy SW is unknown due to the lack of processing history for this alloy.

3.4.2 Mechanical Properties

Mechanical properties determined from the CERT tests are summarized in Table 3-12. The table is organized by experiment, showing the test environment, samples tested (including alloy and dose) and results from each including the YS, maximum stress, uniform and total elongation.

Table 3-12: Mechanical properties from CERT tests.

Test ID	Environment	Sample ID (alloy, dpa)	Yield Stress, MPa	Yield Stress in 330°C Air, MPa[a]	Maximum Stress, MPa	Uniform elongation, %[b]	Total Elongation, %[b]
CI-01	**BWR NWC (288° C)**	K-4 (CP304L, 0)	687	NM	722	1.50	6.10
		ES21 (HP304L, 10.7)	691	712	691	0.42	3.45
CI-02	**BWR NWC (288° C)**	K-5 (CP304L, 0)	805	NM	810	0.65	2.78
		GS14 (HP304L+Mo, 11.8)	705	745	705	0.43	2.93
		PS15 (HP316L+Hf, 9.6)	696	688	696	0.43	1.93
		HS13 (HP304L+Si, 7.8)	587	829	587	0.36	0.99
CI-03	**BWR NWC (288° C)**	K-6 (CP304L, 0)	867	NM	888	1.15	1.43
		KS13 (HP304L+Ni, 9.6)	574	606	574	0.35	5.14
		LS13 (HP304L+Ni+Cr), 9.1)	633	NM	633	0.39	4.98
		B123 (CW CP316L, 5.4)	843	861	855	0.97	3.94
CI-04	**BWR NWC (288° C)**	SW36 (CP304L, 4.4)	602	623	602	0.36	5.53
		AS13 (CP304L, 5.5)	755	784	755	0.45	1.04
		AS17 (CP304L, 10.2)	616	825	616	0.37	0.72
		AS22 (CP304L, 47.5)	608	907	608	0.37	0.54
CI-05	**BWR HWC (288° C)**	PS14 (HP316L, 9.6)	687	688	687	0.42	3.50
		AS18 (CP304L, 10.2)	754	825	754	0.46	2.99
		K-4 (CP304L, 0)	665	NM	682	1.08	5.37
		ES16 (HP304L, 10.2)	707	712	707	0.45	4.56
CI-06	**PWR PW (320° C)**	SW37 (CP304L, 4.4)	695	623	695	0.42	8.24
		AS14 (CP304L, 5.5)	794	784	794	0.48	3.53
		AS19 (CP304L, 10.2)	813	825	813	0.49	4.65
		AS23 (CP304L, 47.5)	793	907	793	0.48	0.62
CI-07	**PWR PW (320° C)**	B126 (CW CP316L, 25)	916	947	953	1.07	3.44
		BR15 (CW CP316L, 4.8)	840	861	858	1.18	3.99
		K-5 (CP304L, 0)	889	NM	935	1.83	4.82
CI-08	**PWR PW (320° C)**	BS13 (CW CP316L, 5.5)	1023	1056	1065	1.76	3.58
		BS16 (CW CP316L, 10.2)	1126	1087	1204	1.07	3.43
		CR13 (CW CP316L, 4.8)	945	949	963	0.80	3.67
		K-5 (CP304L, 0)	967	NM	996	1.18	3.61
CI-09	**PWR PW (320° C)**	ES14 (HP304L, 11.8)	681	712	681	0.41	4.60
		GS13 (HP304L+Mo, 11.8)	676	745	676	0.41	4.79
		FS13 (HP304L-C, 9.1)	1140[c]	594	1140[c]	NA[c]	2.65
		PS13 (HP316L+Hf, 9.6)	730	688	730	0.44	5.74

[a] Data reproduced from [22]

[b] Based on the original gage length of 12 mm.

[c] Data not collected, values were not available or estimated by extrapolation of pre- and post-yield stress-strain data.

For all samples irradiated in the solution annealed condition, uniform elongation was the strain at the yield point (~0.5%) because of strain softening. Irradiated samples with prior cold work all displayed a small amount of strain hardening and limited amounts of uniform elongation, never exceeding 2%. Despite the small uniform elongation in most cases, a wide range in total elongation (TE) (0.54% to 8.24%) was observed. In general, TE increased in HWC and PW environments compared to NWC. TE decreased with increasing dose, although CW materials showed more consistent TE with variations in dose.

3.4.3 Fractography

Following CERT testing, the fracture and gage surfaces were fully examined by SEM. Areas of IG or TG cracking were quantified to determine %IG, %TG, or % mixed IG/TG. Reduction in area was also determined based on the full area of the fracture surface. Each sample fracture surface is shown in Figure 3-24. Although not shown, gage surfaces were fully investigated for the existence of secondary cracks and other defects such as pitting. Previous semi-annual reports (January 2012, July 2012, January 2013, July 2013) contain all gage surface images as well as higher magnification investigation of each fracture surface.

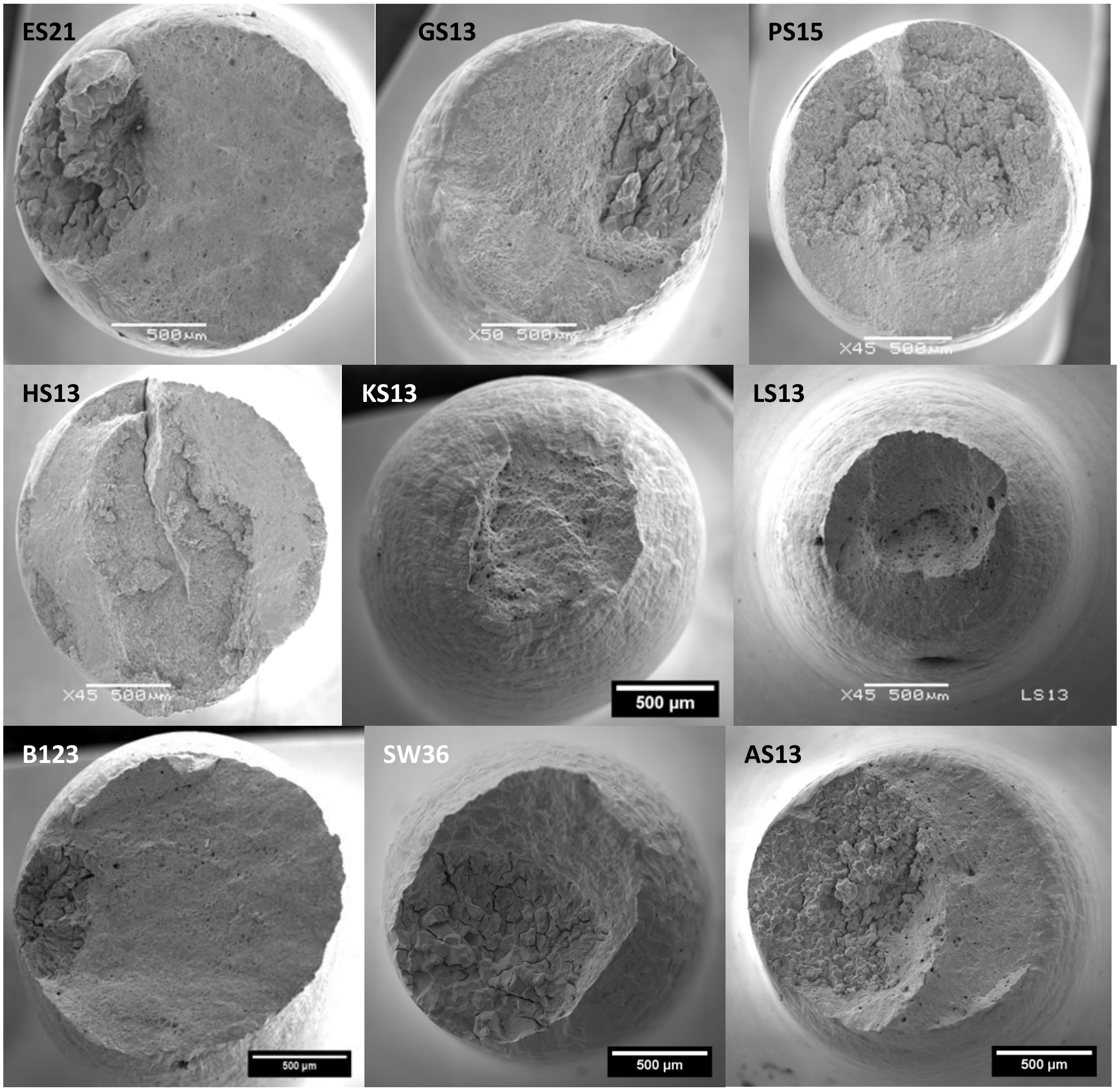

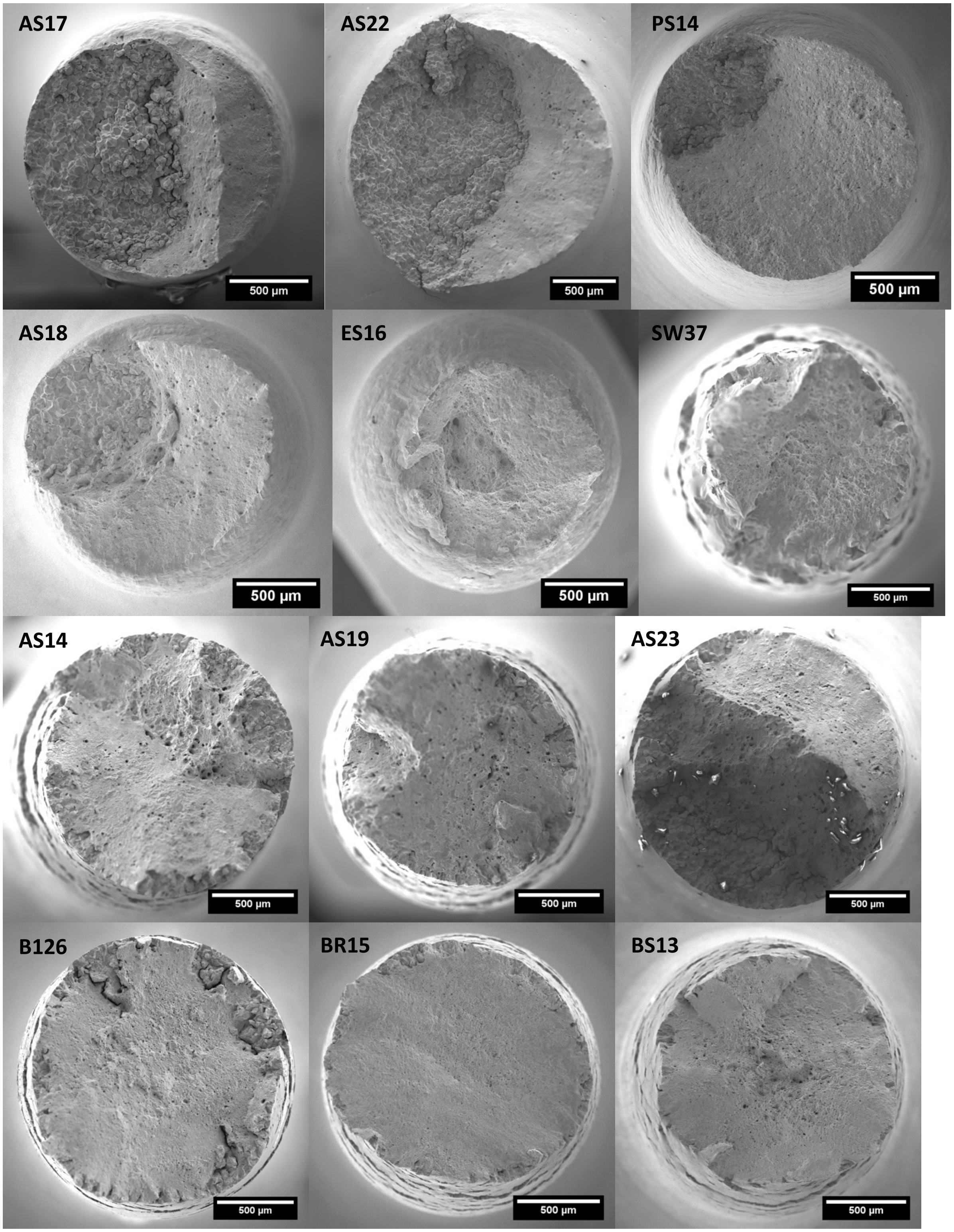
AS17
500 µm
AS22
500 µm
PS14
500 µm
AS18
500 µm
ES16
500 µm
SW37
500 µm
AS14
500 µm
AS19
500 µm
AS23
500 µm
B126
500 µm
BR15
500 µm
BS13
500 µm

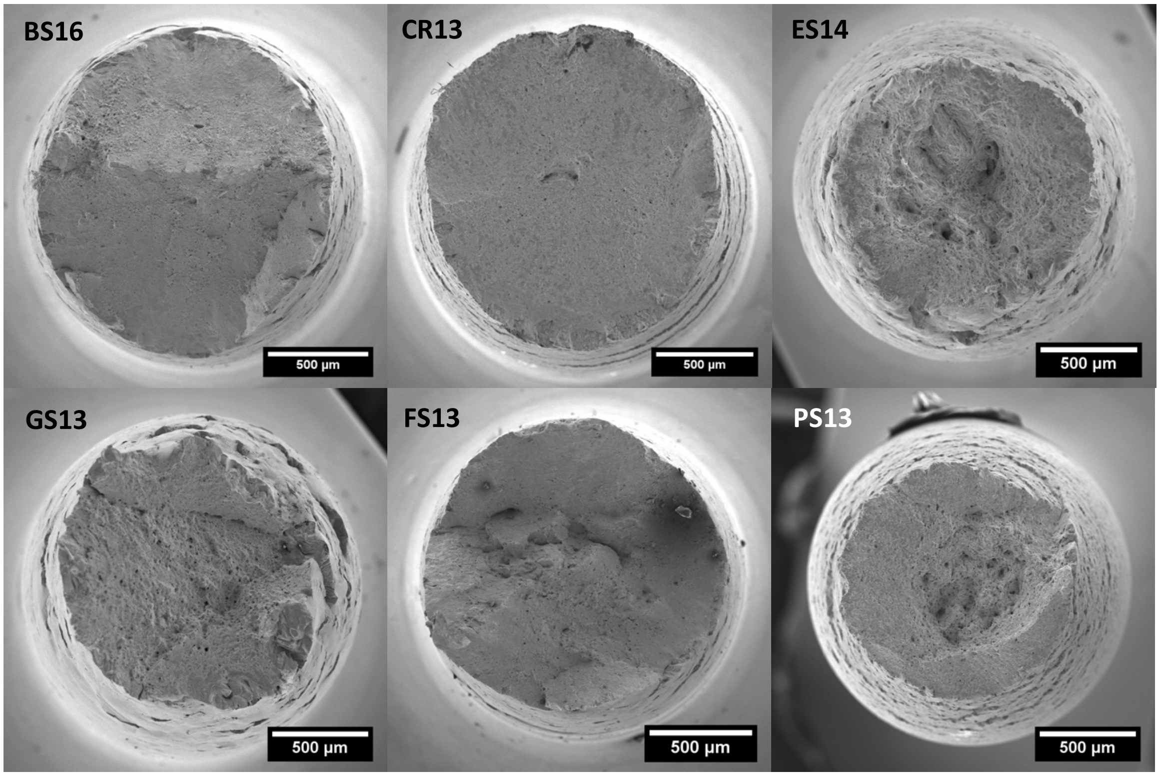

Figure 3-24: Fracture surfaces of samples strained to failure during CERT tests.

The results of the fractography and reduction of area analysis after CERT are summarized in Table 3-13. Commercial purity alloy AS samples were the most susceptible to IASCC in all test environments. High purity solute addition alloys were less susceptible than the CP alloys, and not susceptible to IGSCC in the PW environment. Similar to the results from the CERT tests in NWC, alloy PS was the most susceptible solute addition alloy in the PW environment. Cold work apparently reduced the amount of IG cracking in both NWC and PW. BS alloys with presumably the highest amount of cold work were the least susceptible of the cold worked alloys.

%IG varied between 0% and 57.5% for all irradiated samples. In general, %IG was higher in NWC than in HWC or PW for a given alloy. %IG was accepted as the best indicator of IASCC susceptibility and is used to describe relative differences in cracking susceptibility throughout the discussion chapter.

Reduction of area followed a similar trend as total elongation but could not be calculated for sample AS22 due to failure at the sample shoulder where the initial cross-sectional area was unknown. Typically, either measure of ductility (TE or %RA), followed the inverse trend of %IG.

Table 3-13: Reduction in area and percentage of crack type on the fracture surface.

Test ID	Environment (°C)	Sample (Alloy, dpa)	RA (%)	%IG	%Mixed IG/TG	%Ductile
CI-01	**BWR NWC (288)**	K-4 (CP304L, 0)	49.7	0.0	12.8[a]	87.2
		ES21 (HP304L, 10.7)	39.2	16.8	7.4	75.8
CI-02	**BWR NWC (288)**	K-5 (CP304L, 0)	36.8	0.0	13.4[a]	86.6
		GS14 (HP304L+Mo, 11.8)	38.6	16.9	9.1	74.1
		PS15 (HP316L+Hf, 9.6)	31.8	50.5	8.4	41.1
		HS13 (HP304L+Si, 7.8)	13.3	42.8	14.2	43.1
CI-03	**BWR NWC (288)**	K-6 (CP304L, 0)	20.8	0.0	12.9[a]	87.1
		KS13 (HP304L+Ni, 9.6)	78.5	0.0	0.0	100.0
		LS13 (HP304L+Ni+Cr), 9.1)	64.5	0.0	0.0	100.0
		B123 (CW CP316L, 5.4)	40.7	4.2	10.5	89.5
CI-04	**BWR NWC (288)**	SW36 (CP304L, 4.4)	58.8	29.2	32.5	38.3
		AS13 (CP304L, 5.5)	45.3	40.7	0.0	59.3
		AS17 (CP304L, 10.2)	39.9	55.9	0.0	44.1
		AS22 (CP304L, 47.5)	NA	57.5	0.0	42.5
CI-05	**BWR HWC (288)**	PS14 (HP316L, 9.6)	37.9	16.9	0.0	83.1
		AS18 (CP304L, 10.2)	41.6	23.4	0.0	76.6
		K-4 (CP304L, 0)	65.6	0.0	0.0	100.0
		ES16 (HP304L, 10.2)	64.1	0.0	0.0	100.0
CI-06	**PWR PW (320)**	SW37 (CP304L, 4.4)	52.2	5.2	0.0	94.8
		AS14 (CP304L, 5.5)	38.7	20.4	0.0	79.6
		AS19 (CP304L, 10.2)	46.7	14.0	0.0	86.0
		AS23 (CP304L, 47.5)	20.2	28.4	0.0	71.6
CI-07	**PWR PW (320)**	B126 (CW CP316L, 25)	41.4	22.4	0.0	77.6
		BR15 (CW CP316L, 4.8)	53.8	10.9	0.0	89.1
		K-5 (CP304L, 0)	51.7	0.0	1.4	98.6
CI-08	**PWR PW (320)**	BS13 (CW CP316L, 5.5)	44.5	3.7	0.0	96.3
		BS16 (CW CP316L, 10.2)	42.1	3.9	0.0	96.1
		CR13 (CW CP316L, 4.8)	36.2	9.6	0.0	90.4
		K-5 (CP304L, 0)	48.0	0.0	0.6[a]	99.4
CI-09	**PWR PW (320)**	ES14 (HP304L, 11.8)	57.4	0.0	1.6[a]	98.4
		GS13 (HP304L+Mo, 11.8)	50.4	0.0	11.9	88.1
		FS13 (HP304L-C, 9.1)	42.5	0.0	1.3	98.7
		PS13 (HP316L+Hf, 9.6)	61.8	1.8	0.0	98.2

[a] Only TG type cracking was observed.

3.4.4 Step Height Measurement

Dislocation channel step heights were measured on several select samples after failure during CERT testing. Measurements were taken from replicas made of the gage surfaces after oxide removal had been performed. Randomly selected grains near the IG fracture edge were measured, because these regions were believed to be IG crack initiation sites. A summary of the dislocation channel height measurement is shown in Table 3-14, along with select CERT test results for comparison. Error values for the weighted average channel height were calculated based on the standard deviations calculated from each measured channel height.

Table 3-14: Dislocation channel height analysis from sample replicas, with CERT test results for comparison.

Sample ID	Dose, dpa	TE, % (air)	YS, MPa	TE, %	%IG	Grains Analyzed	Channels Analyzed	Weighted Avg. Channel Height, nm
AS13	5.5	8.4	755	1.04	40.7	16	130	291 ± 57
AS17	10.2	8.0	616	0.72	55.9	9	82	364 ± 67
AS18	10.2	8.0	754	2.99	23.4	11	130	507 ± 93
AS22	47.5	7.8	608	0.54	57.5	7	25	1342 ± 497
ES21	10.7	7.6	691	3.45	16.8	10	136	265 ± 34
KS13	9.6	10.7	574	5.14	0.0	11	146	541 ± 127

Dislocation channel height varied substantially among the six samples. Due to the low elongation during CERT, samples AS17 and AS22 had very few visible channels, limiting the number available for analysis. The gage surfaces of samples AS13 and AS22 are compared in Figure 3-25 as an example. Weighted average channel height decreased in the order: AS22, AS18, AS17, AS13 for commercial purity alloys. The high purity ES21 sample had the lowest channel height of all samples, and the KS13 sample with no IG cracking had a step height of nearly double that of sample ES21. Because of the lack of IG cracking, step height measurements were taken in the necked region of the gage surface on KS13, which likely caused the increased channel height.

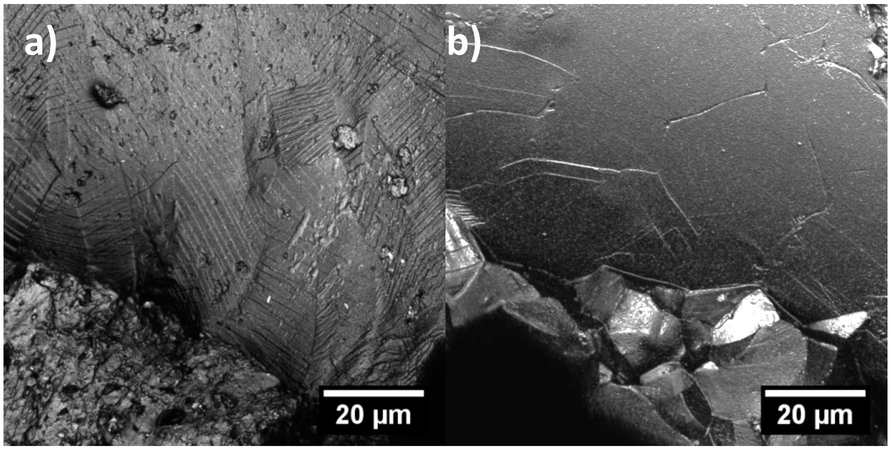

Figure 3-25: Surface topography of the gage surfaces of a) AS13 and b) AS22. The IG fracture edge is visible at the bottom of each image.

3.5 *Four-Point Bend Test Results*

To describe and qualify the strain state created during the four-point bend test, results of the FEA model are first presented and compared with unirradiated bend test results in RT air, 288°C Ar gas, and 288°C NWC. Results from irradiated samples are then summarized, while discussing the capability of the bend test to create IASCC initiation with limited crack propagation, and how bend test results compare to more traditional SCC initiation test techniques. Results will focus on the convex surface of the bend sample, where the tensile stress/strain state exists. Images are presented with the sample oriented as shown in Figure 3-26, with the tensile (ε_{xx}) direction left to right.

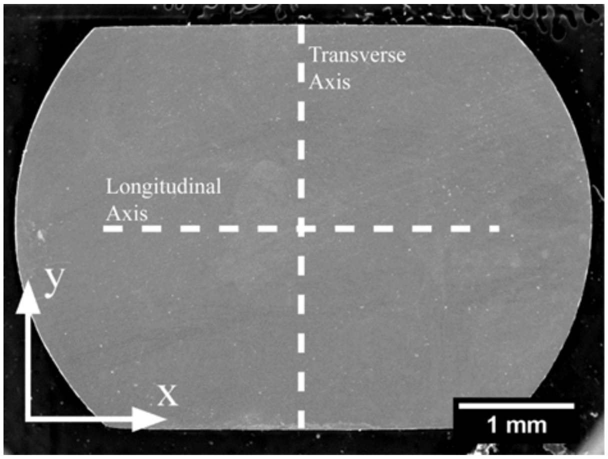

Figure 3-26: Sample orientation and coordinate system. Dashed lines indicate axes for strain profiles.

3.5.1 FEA results

A full description of the in-plane surface strain for the 16.9% CW condition at a sample deflection of 58.3 μm is shown in Figure 3-27. This amount of deflection was chosen as it gives a description of the strain state after a significant amount of plastic deformation. The xx component of the strain tensor accounted for the majority of the surface strain, however, strain in the yy component was observed near the edges of the sample. Very little shear strain (xy component) was created on the sample surface. A more quantified view of the surface strain as a function of deflection for the 16.9% CW condition is shown in Figure 3-28. The main difference observed by changing material condition was in the response of the xx component of strain, which is shown for the AR condition in Figure 3-29. Because of the lower yield stress, strain peaks under the loading points become larger, and are likely a result of additional tensile stress formed by the frictional constraint at the lower sample supports due to the small sample size. This likelihood was confirmed by performing FEA simulations with an increased coefficient of friction between the sample and supports. With an increased coefficient of friction, the formation of strain peaks was observed at the same locations but at smaller sample deflection.

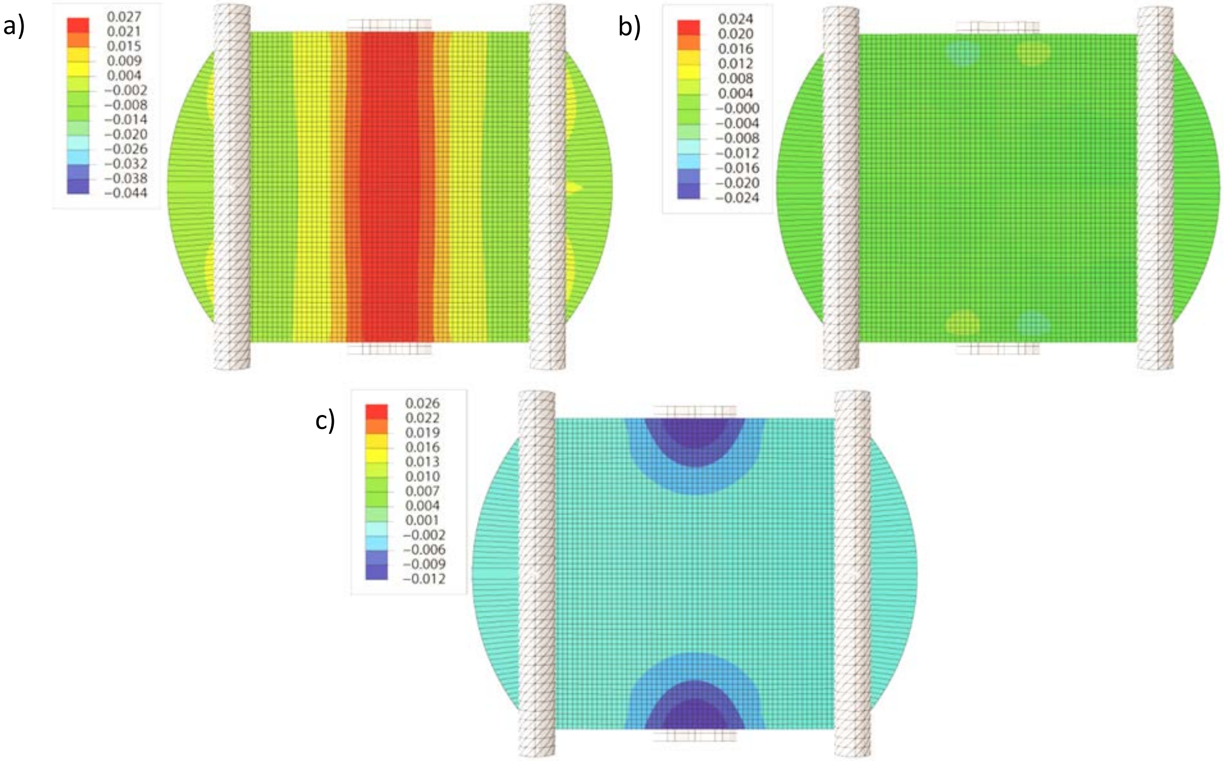

Figure 3-27: Color representations of total strain (elastic plus plastic) components a) xx, b) xy, c) yy. 16.9% CW condition after a sample deflection of 58.3 µm.

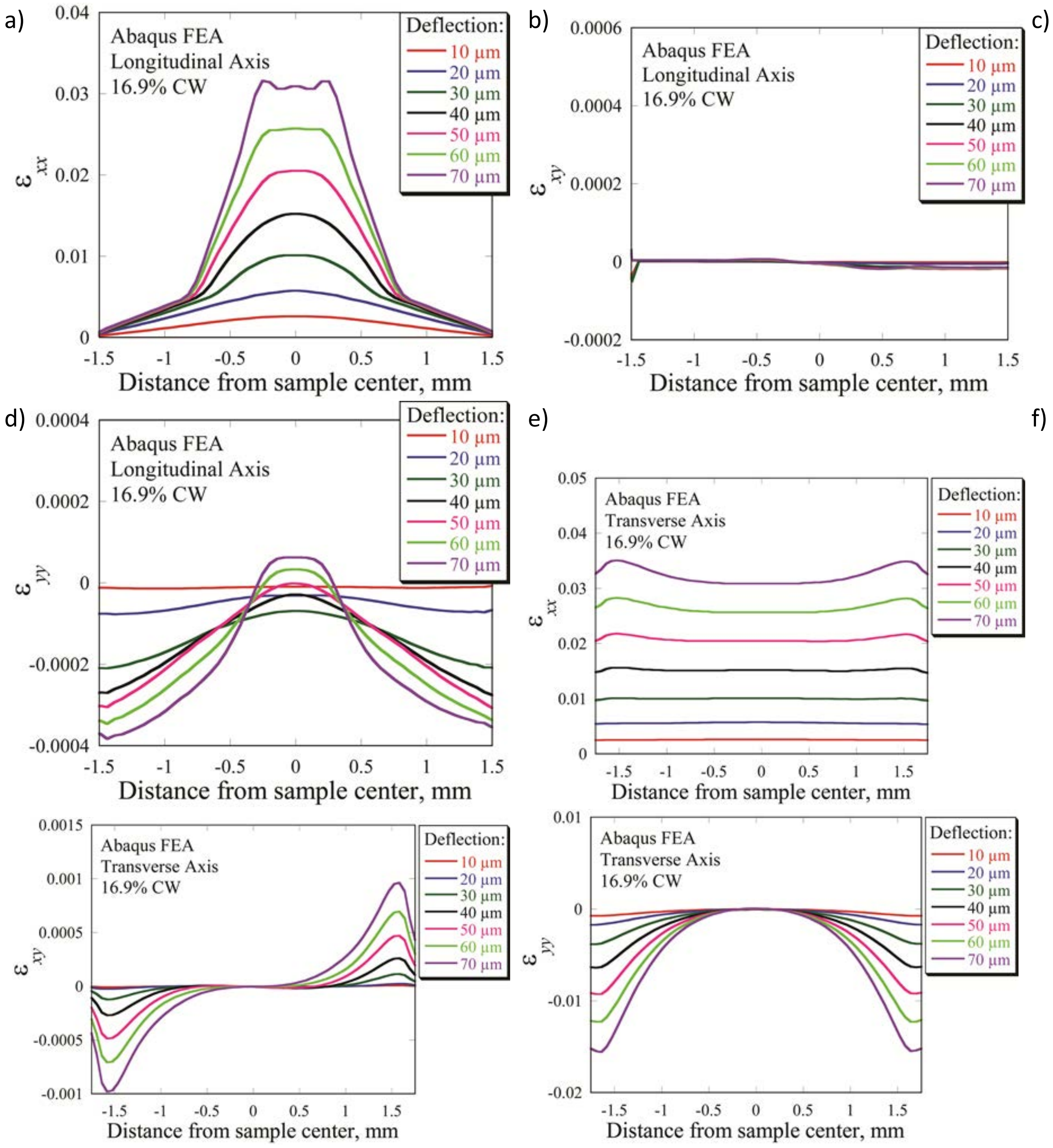

Figure 3-28: Quantitative strain profiles for the 16.9% CW condition at a variety of sample deflections. a) xx, b) xy, and c) yy components of strain along the longitudinal axis, and d) xx, e) xy, and f) yy components of strain along the transverse axis of the bend sample.

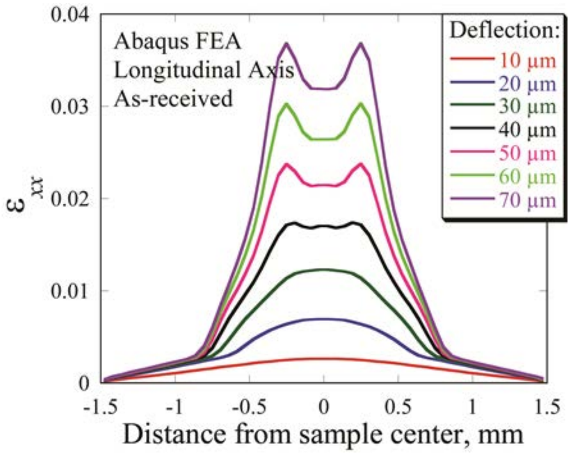

Figure 3-29: Quantitative strain profiles (xx component) at various sample deflections for the AR condition.

Experimental error determination

Several modifications were made to the model to determine the effect of possible errors that could occur during experimentation. Specifically, the effect of off-centering the sample laterally (Figure 3-10), off-centering the load points laterally (Figure 3-11), or varying sample thickness along the longitudinal direction (Figure 3-12). Comparing these effects at similar amounts of bend deflection in the simulation showed that none would significantly impact the strain profile during bend testing.

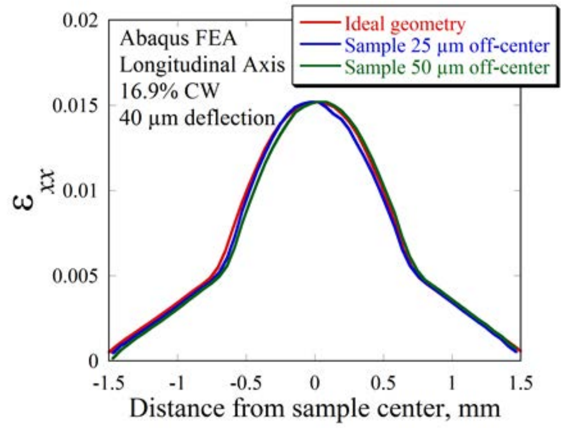

Figure 3-10: The effect of sample lateral off-centering on the xx component strain profile for the 16.9% CW condition at 40 μm deflection.

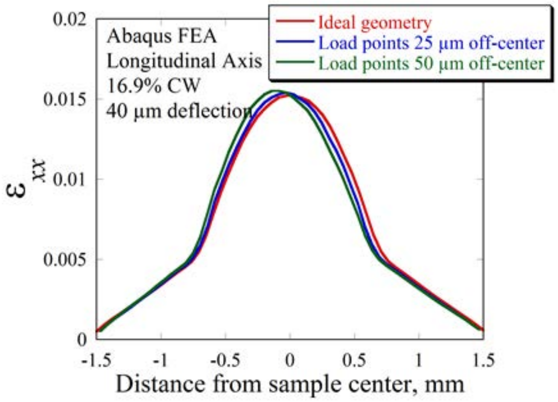

Figure 3-11: The effect of load point lateral off-centering on the xx component strain profile for the 16.9% CW condition at 40 μm deflection.

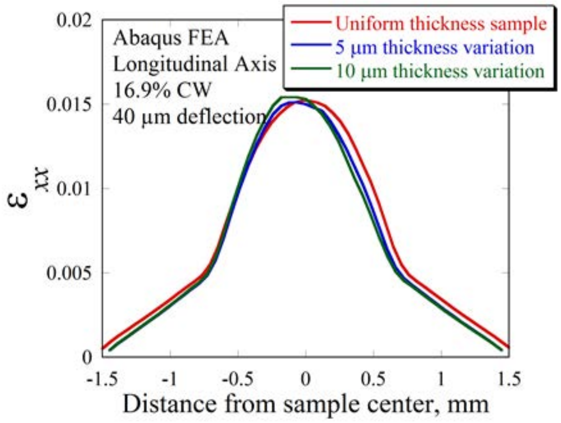

Figure 3-12: The effect of sample thickness variation on the xx component strain profile for the 16.9% CW condition at 40 μm deflection.

3.5.2 Four-point bend tests of unirradiated samples

To confirm accurate results in the FEA model, a series of bend tests were performed on unirradiated, cold-worked materials with a yield strength range similar to the neutron irradiated samples planned for testing. A summary of the unirradiated bend tests performed and their results is shown in Table 3-15.

Table 3-15: Unirradiated four point bend test matrix.

Environment	**Sample Condition and ID**	**Increment No.**	**Sample Deflection, µm**	**Deflection Measurement Technique**	**Sample Center Strain**	**Strain Standard Deviation**	**Strain Measurement Technique**
RT Air	AR #1	1	21.3	Direct	0.004	0.002	DIC
RT Air	AR #1	2	29.2	Direct	0.007	0.003	DIC
RT Air	AR #1	3	39.0	Direct	0.014	0.004	DIC
RT Air	AR #1	4	49.6	Direct	0.020	0.006	DIC
RT Air	16.9% CW #1	1	30.0	Direct	0.005	0.003	DIC
RT Air	16.9% CW #1	2	40.1	Direct	0.008	0.003	DIC
RT Air	16.9% CW #1	3	49.9	Direct	0.019	0.004	DIC
RT Air	16.9% CW #1	4	59.7	Direct	0.027	0.005	DIC
RT Air	16.9% CW #2	1	38.4	Direct	0.008	0.002	DIC
288 °C Ar	16.9% CW #3	1	39.8	Correction Factor	0.008	0.002	DIC, Indent Spacing
288 °C NWC	16.9% CW #4	1	42.2	Correction Factor	0.013	0.004	Indent Spacing

Bend tests were first performed in air on samples at both levels of CW, utilizing direct sample deflection measurement as well as DIC for surface strain measurement. One sample of each condition was tested, stopping the experiment after pre-determined increments to record the surface strain. Increments were stopped at sample deflections of 20, 30, 40 and 50 µm on an AR condition sample, and at deflections of 30, 40, 50, and 60 µm on a 16.9% CW condition sample. Load vs. deflection curves for each material condition after the incremented tests are shown in Figure 3-13.

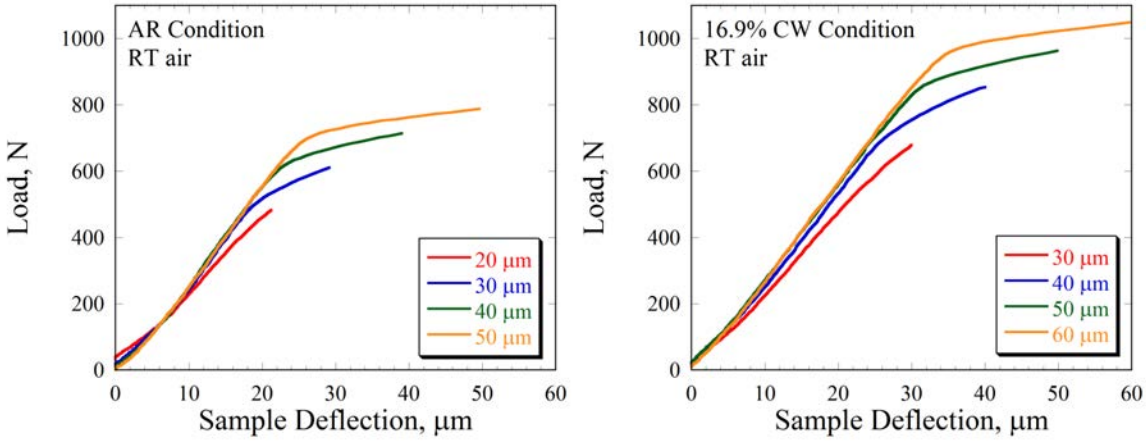

Figure 3-13: Load vs. sample deflection curves for incremented bend tests performed in RT air on a sample of the AR condition (left) and 16.9% CW condition (right).

Surface strain in the center of the bend sample after the incremented bend tests is compared with FEA model results in Figure 3-14. The small amount of disagreement is likely due to elastic spring-back between increments, which was not accounted for in the measurements.

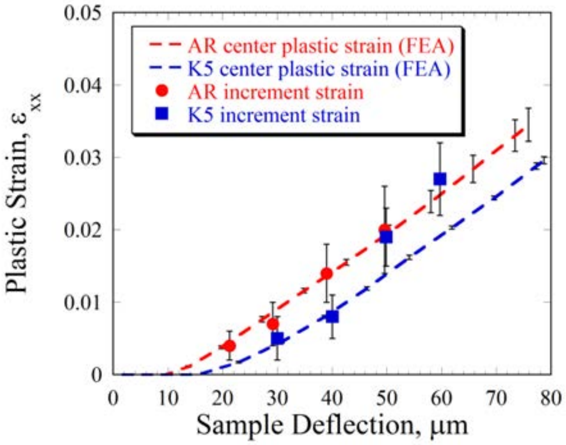

Figure 3-14: Average strain at the bend sample center after incremented experiments and FEA on each unirradiated material condition.

Three additional bend tests were performed to a nominal sample deflection of 40 µm on samples in the unirradiated 16.9% CW condition. These three bend tests were performed in RT air, 288°C Ar, and 288°C NWC environments to confirm similar bend test behavior in the three environments, and compare strain behavior with the results from the incremented bend tests. Load vs. deflection curves for these experiments are shown in Figure 3-15. Due to the high temperature in Ar and NWC, the sample deflection was not directly measured but was instead estimated using the appropriate high temperature compliance correction, detailed in Section 2.3.5. Use of this technique resulted in noise in the measured deflection because small changes in load (due to noise in the load cell) caused relatively large changes in the correction factor. All average strain measurements from the 16.9% CW condition are compared in Figure 3-16, showing that results in the high temperature environments agree well with those measured at room temperature, and incrementing strain in the bend test also has a negligible effect. Figure 3-17 shows the distribution of plastic strain in the longitudinal axis. The peak strain is fairly constant in the central 0.5 mm region.

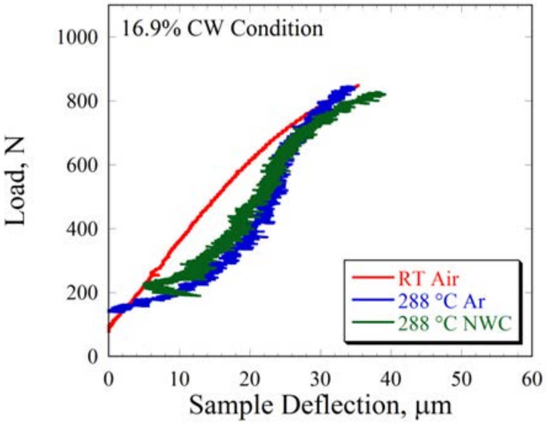

Figure 3-15: Load vs. sample deflection curves for bend tests on a 16.9% CW sample performed in RT air, 288 °C Ar, and 288 °C NWC.

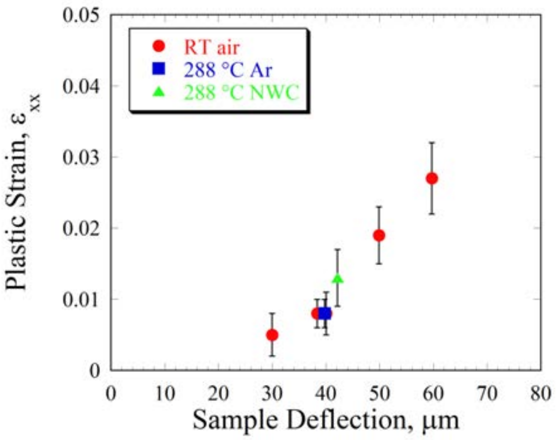

Figure 3-16: Average strain at the bend sample center for 16.9% CW samples in the three environments described in Fig. 13.

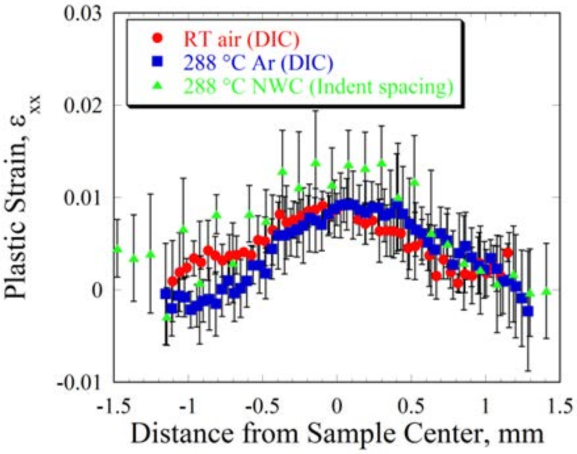

Figure 3-17: Plastic strain (ε_{xx}) in the longitudinal axis of 16.9% CW samples after 40 µm sample deflection in each test environment. Strain in NWC was measured via indent spacing.

3.5.3 Four-point bend tests of irradiated samples

The first neutron irradiated bend sample, alloy AS (CP 304L) irradiated to 10.2 dpa, was strained to failure in a single increment. This procedure determined general susceptibility to cracking, and established a guideline for subsequent bend tests, which were performed in small strain increments with the intent of stopping deformation at a point when a crack had become visible, but with a limited amount of propagation. An example of the load vs. LVDT deflection curves determined from an incremented bend experiment is shown in Figure 3-18, and a summary of the neutron irradiated bend test results are presented in Table 3-16. Fractions of the yield strength in bending were calculated based on the correlation observed between tensile yield strength and load required to cause yield in the bend test, Figure 3-19. When the yield strength was exceeded, plastic strain in the longitudinal direction (ε_{xx}) is used to track the deformation. Tensile yield strength values for irradiated alloys were obtained from [26]. The final increment of each sample presented in Table

3-16 indicates when a crack initiation site was first observed, except in the case of alloy KS which was not expected to form an intergranular crack based on the purely ductile failure mode observed after CERT testing [14].

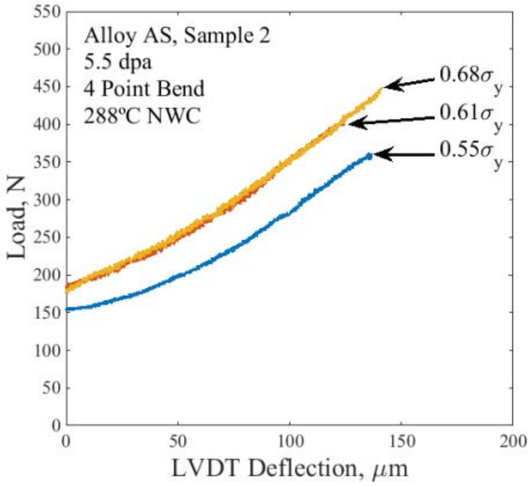

Figure 3-18: Load vs LVDT deflection curves for alloy AS at 5.5 dpa (#2), which was strained in three increments.

Table 3-16: Irradiated four point bend test matrix. N/A indicates that value was not available.

			Increment									
Alloy, dpa	**ID No.**		**1**	**2**	**3**	**4**	**5**	**6**	**7**	**8**	**9**	**10**
AS, 10.2	1	σ_y	1.12									
		ε_{xx}	N/A									
AS, 5.5	1	σ_y	0.63	0.82								
		ε_{xx}	–	–								
AS, 10.2	2	σ_y	0.45	0.51	0.58	0.61						
		ε_{xx}	–	–	–	–						
AS, 5.5	2	σ_y	0.54	0.61	0.68							
		ε_{xx}	–	–	–							
ES, 10.2	1	σ_y	0.68	0.76	0.83	0.89	0.97	1.16	1.28	1.11		
		ε_{xx}	–	–	–	–	–	0.0033	0.0029	N/A		
KS, 9.6	2	σ_y	0.73	0.98	1.21	1.41	1.42	1.46	1.46	1.56	1.57	1.69
		ε_{xx}	–	–	0.0013	0.0054	0.0050	0.0046	0.0000	0.0059	0.0050	0.0059
AS, 47.5	1	σ_y	0.38	0.43								
		ε_{xx}	–	–								

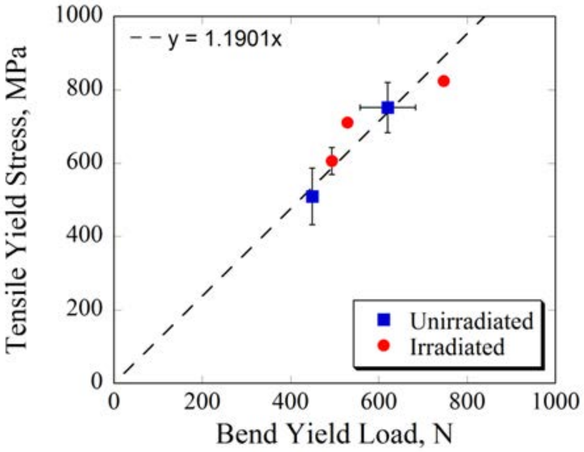

Figure 3-19: Comparison between tensile yield strength (determined from CERT experiments in 288°C NWC) and load required to cause yield in the four point bend test (in RT air for unirradiated samples and 288°C NWC for irradiated samples).

The CP 304L alloy was highly susceptible to IGSCC; crack initiation occurred prior to macroscopic yield at all three irradiation doses. By performing the bend tests in increments, several observations were made, which resulted in a better understanding of the crack initiation process. The first observation of discrete, localized plastic deformation (dislocation channels) was at an applied stress as low as 38% of the anticipated yield stress in bending. Examples of this deformation, Figure 3-20 and Figure 3-21, show that despite the highly brittle state of alloy AS and the limited number of sites of localized deformation observed outside of the IGSCC initiation sites, deformation occurs prior to IGSCC initiation in alloy AS. Deformation was not observed prior to crack initiation in the 10.2 dpa alloy, however it was assumed to occur because of it was observed observations in the 5.5 and 47.5 dpa samples.

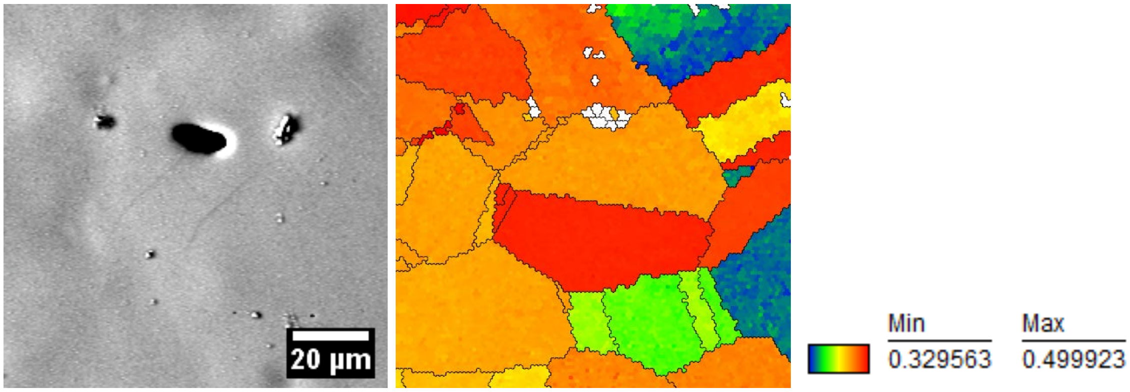

Figure 3-20: Deformation observed on the surface of the 47.5 dpa alloy AS sample after loading to $0.38\sigma_{ys}$ (left), and corresponding EBSD pattern showing schmid factor of grains in this region (right).

Localized deformation was also typically observed at IGSCC initiation points, as observed in Figure 3-21 as well as Figure 3-22, which show crack initiation sites after oxide removal. Despite the observation of localized deformation adjacent to IGSCC initiation sites, it is still unknown whether the deformation is a necessary precursor to crack formation.

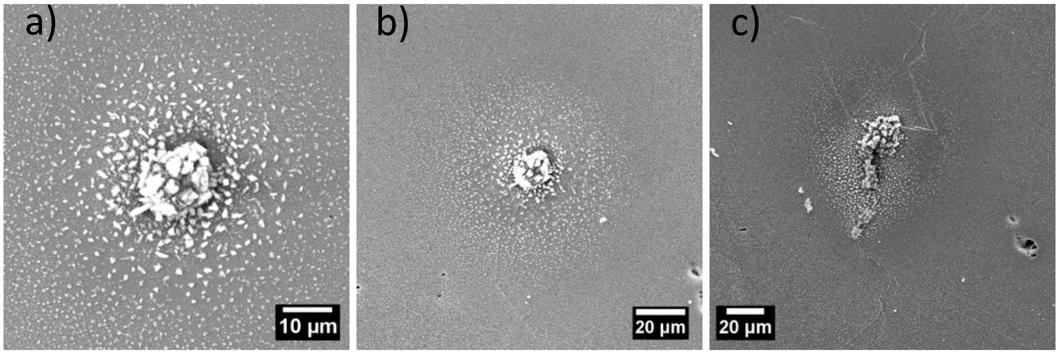

Figure 3-21: The location of the IGSCC crack on the 5.5 dpa alloy AS bend sample (#2) after a) 0.55σ_y, b) 0.61σ_y, c) and 0.68σ_y.

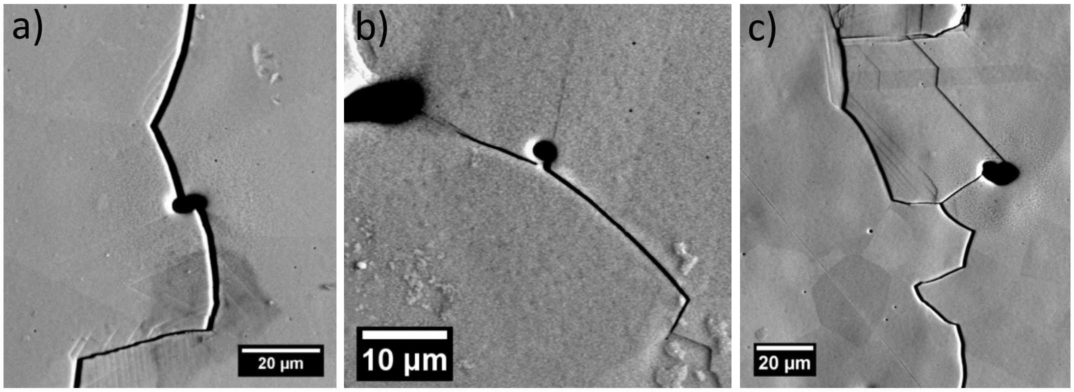

Figure 3-22: IGSCC initiation points in alloy AS at a) 5.5, b) 10.2, and c) 47.5 dpa after oxide removal.

Also seen in Figure 3-22 are surface inclusions at IGSCC initiation sites. Stress concentration at these large surface inclusions was a likely a factor causing the high susceptibility of alloy AS. The size of the inclusions may be account for the difference in susceptibility compared to alloy ES and KS, which still had much smaller inclusions than those in alloy AS, Figure 3-23. IGSCC initiation sites were typically observed at inclusion sites within the largest 10% of all inclusions observed on the sample surface.

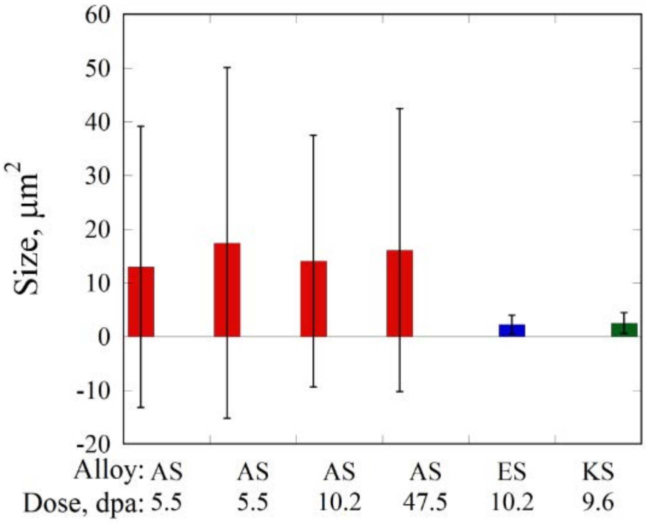

Figure 3-23: Average inclusion size on irradiated sample surfaces, recorded in the center 1 mm x 3.5 mm area of bend sample surfaces. Error bars represent standard deviations of the mean.

A final commonality observed at alloy AS IGSCC initiation points was large corrosion product formation. As observed in Figure 3-21, corrosion product formation occurred at inclusions prior to the formation of a crack, but the corrosion product increased in size with the opening of an IG crack. Corrosion was not typically observed at inclusion sites, only occurring at <1% of surface inclusions on alloy AS bend sample surfaces. It is still unknown whether this corrosion product forms without the application of stress, or whether a crack in the inclusion is necessary for the formation of a crevice to induce corrosion product formation. Further experiments are necessary to separate the effects of corrosion product formation and localized deformation in the IASCC initiation process of alloy AS samples.

HP alloys ES and KS displayed very different behavior than alloy AS, as expected from previous CERT test results. Significant amounts of localized deformation were observed prior to both the point of macroscopic sample yielding, as well as IGSCC initiation in the HP 304L alloy. As expected from the observation of ductile failure in the CERT test, the HP 304L+Ni alloy did not form an IGSCC crack after straining to ~3.3% plastic strain. Two cracks initiated in the HP 304L alloy at the sample edge, Figure 3- and Figure 3-25. Due to interaction with the sample edge, it is difficult to identify the exact cause of crack formation, and what caused the difference in cracking susceptibility between the two HP alloys. However, comparing localized deformation at similar levels of strain on the two alloy surfaces showed that the density of slip transmission sites in alloy KS were higher than in alloy ES, Figure 3-. Slip transmission can refer to locations where a dislocation channel transmits across a grain boundary, cross slips onto a separate slip system in the same grain, or causes grain boundary sliding. All events resulted in a sharp direction change in the trace of the dislocation channel, and were assumed to impart less stress to a grain boundary than interactions where the dislocation channel forms a discontinuous interaction with the grain boundary [16]. Since less stress is able to accumulate at channel – grain boundary intersections in alloy KS (due to the higher probability of slip transmission), the stress required for IG crack initiation is likely unable to be achieved.

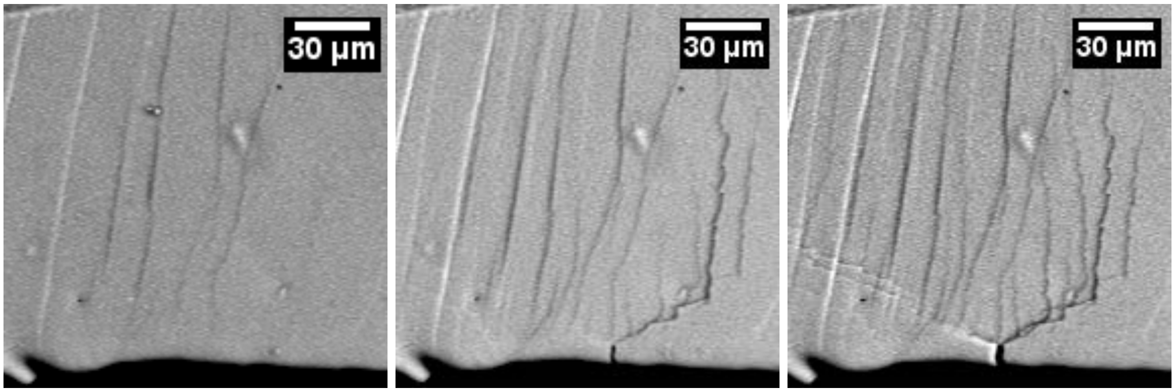

Figure 3-24: The region where the small IGSCC crack formed at the edge of the 10.2 dpa alloy ES sample a) prior to initiation after straining to 0.97σ_y, b) after crack initiation at ε_{xx} = 0.3%, and c) after straining to ε_{xx} = 0.6%.

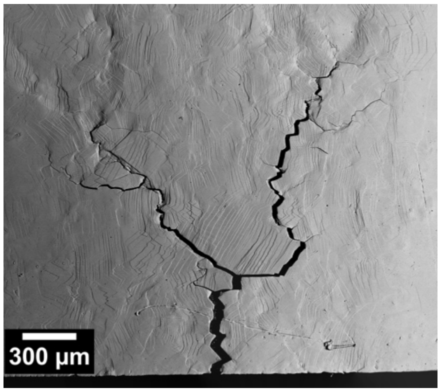

Figure 3-25: The large IGSCC crack on the 10.2 dpa alloy ES sample after the final straining increment.

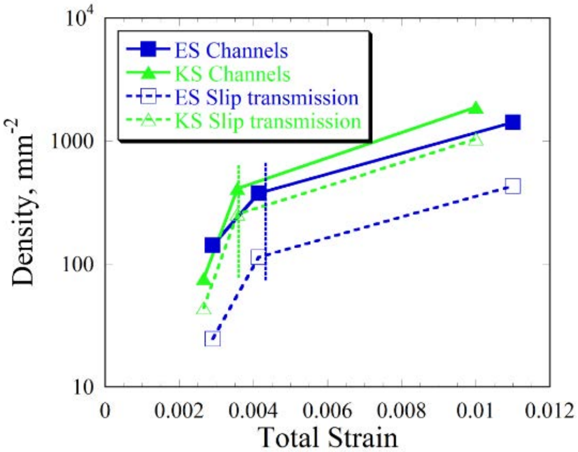

Figure 3-26: Comparison of localized deformation on HP alloys ES and KS after a range of applied strain. Vertical solid lines represent the point at which macroscopic yield was observed.

3.5.4 Comparison to Literature

The strain to crack initiation from the four-point bend tests is compared with strain to failure determined from previous CERT tests in Figure 3-27. A linear relationship is observed between the two measures of strain obtained from the experiments, indicating that the CERT test clearly gives a good indication of crack initiation susceptibility, and the strain to failure determined from this test is representative of the strain to crack initiation.

The stress at crack initiation determined from four-point bend tests in BWR NWC was compared with the results of constant load experiments on neutron irradiated stainless steels in PWR environments. The constant load test database has been summarized by Fyfitch [27] and indicates that a stress threshold to initiate IASCC in a primary water test environment exists at ~40% of the yield strength in high dose materials, greater than approximately 20 dpa. Results of the four-point bend tests have been superimposed over these databases in Figure 3-28, with a red dashed line plotted to indicate the lower threshold for cracking observed in the bend test. Excellent agreement was observed between the two test types, as crack initiation occurred in the bend test between 38% and 43% of the yield strength in the 47.5 dpa specimen. The consistency in this stress threshold between the two test types, despite differences in test environment and material condition (many constant load results were from CW materials), highlights the importance of stress in the IASCC initiation mechanism.

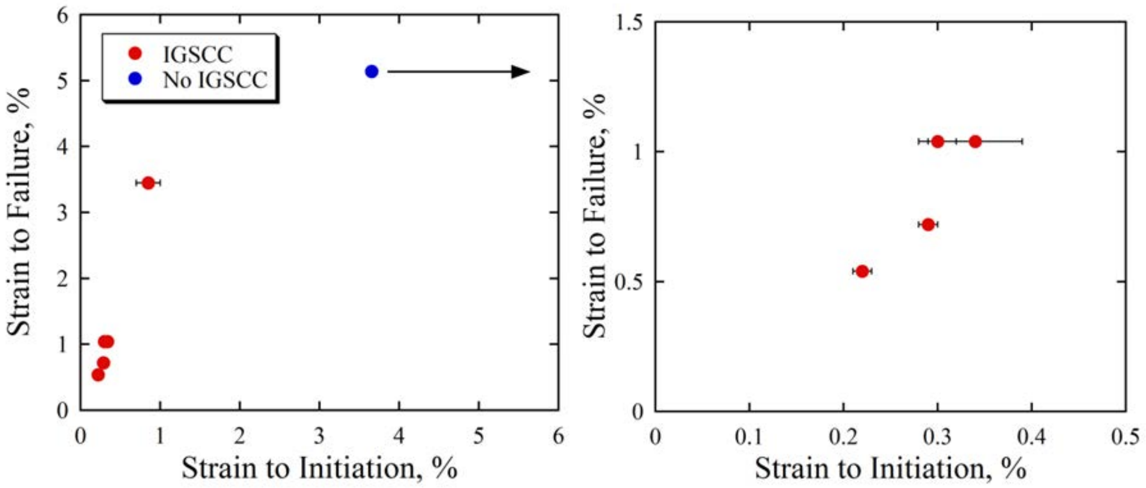

Figure 3-27: Comparison between strain to failure (by CERT testing, from [14]) and strain to initiation determined (from four point bend tests) on neutron irradiated samples tested in 288 °C NWC at a strain rate of $3.5x10^{-7}s^{-1}$. The right figure is a magnified view of the small strains in the left figure.

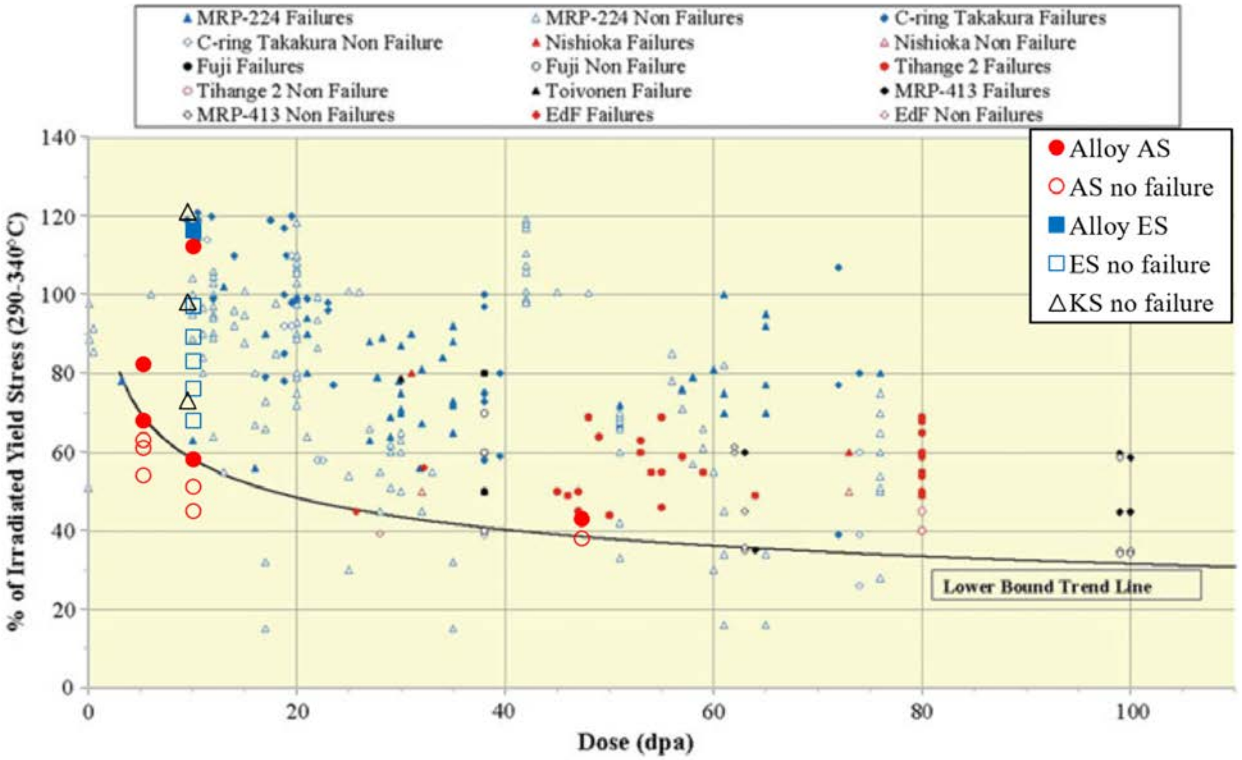

Figure 3-28: Stress required to initiate IASCC as a function of dose. Four point bend test data from the current study in 288°C NWC has been superimposed on the constant load database available from Fyfitch in primary water conditions [27].

3.5.5 Refinement of four-point bend test technique

To provide a dedicated system for the project, the four-point bend test setup has been moved to the IM2 system containing a 4-liter 316 SS autoclave system connected to a water recirculation loop. Furthermore, the previous setup configuration used a multi-specimen CERT loading frame connected to a crosshead outside the vessel through an Inconel 718 pull rod. The displacement data recording was done at the cross-head level. In a CERT experiment, an additional specimen of the same geometry is loaded in a position opposite to the specimen being tested to balance the crosshead. However, in the crack initiation studies using a bend test setup, only one position was being used, which led to an unbalanced crosshead. Since crack initiation studies are carried out at small deflections at the sample surface ~30-50 µm, the reliability of the displacement measurements at the crosshead level are of paramount importance.

To improve the system stability and reliability of the results, it was decided to use a single specimen configuration with the specimen along the central loading axis. Therefore, the system configuration was changed from a multi-specimen CERT loading frame to a single specimen loading frame. The autoclave lid compatible with the single-specimen loading frame (CGR lid) had been machined for use with a 3/8” pull rod. However, at this pull rod dimension, the tare load applied by the high pressure water would be high enough to cause deformation in the sample.

Therefore, an adaptor to allow the use of a smaller, 3/16” pull rod, was designed along with a number of other components to facilitate the use of the CGR lid with the 3/16” pull rod.

The reconfigured IM2 system was employed to conduct four-point bend test with a single specimen aligned with the central loading axis. Load was applied by a 33 kN servo motor which displaces the system crosshead. A linear variable differential transformer (LVDT) mounted to the load train to measure displacement. For room temperature experiments, the deflection at the sample surface has also been measured using a micro-miniature DVRT for comparison purposes. Load readings were measured by a load cell mounted on the pull rod. The same four-point bend fixture shown in Figure 2-9 was used.

Four-point bend tests were initially tested by moving the crosshead at a constant rate of 1.3x10^{-5} in/s until achieving a desired amount of stress or sample deflection. The crosshead displacement rate created a strain rate of 3.5x10^{-5} s^{-1}. At the mid-point of the outer plane of the sample. Straining in environment was done at a much slower displacement rate of 1.3x10^{-7} in/s. System compliance measurements were made using a 5-mm thick block of hardened Inconel 718 loaded up to an applied load of 200 lbs. From prior experience, it was observed that the applied loads for neutron-irradiated materials were significantly lower than 200 lbs. Therefore, the compliance measurements included the entire range of loads applicable to neutron irradiated materials. Subtraction of the compliance from the measured crosshead LVDT displacement gives an approximation to the actual deflection at the sample surface. Furthermore, the compliance has also been measured in room temperature air as the difference between the measurements by the micro-miniature LVDT at the specimen surface and the crosshead LVDT. The schematic illustration of the two methods of compliance measurements is shown in Figure 3-29.

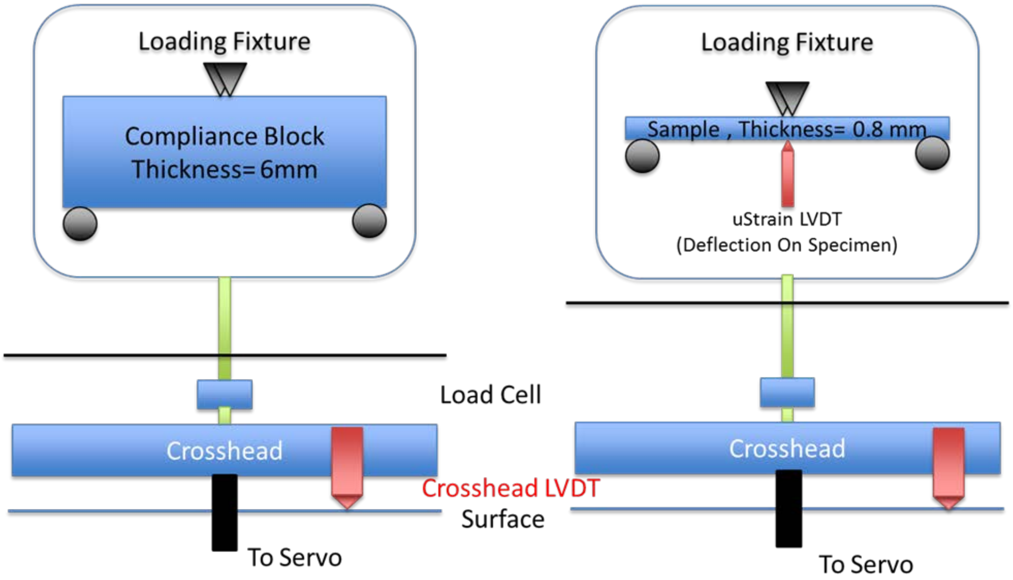

Figure 3-29: Schematic illustration of the compliance measurement setup in IM2 system.

Figure 3-30 shows the compliance measurements for the four-point bend test in single specimen configuration in air. Many of the curves followed the same trend, however, there was some divergence at loads greater than 160 lbs. The compliance fit curve is shown by the dotted line. The equations for calculating the compliance were determined as:

$$y = - 0.00189949x^2 + 2.21551042x - 88.19793270 \qquad (3\text{-}1)$$

in air at room temperature and

$$y = 0.000037x^3 -0.017133x^2 +4.305777x - 133.072585 \qquad (3\text{-}2)$$

in 288 ^{o}C water,

where x is the applied load in pounds and y is the compliance in µm. The compliance subtracted from the crosshead deflection yields the sample deflection.

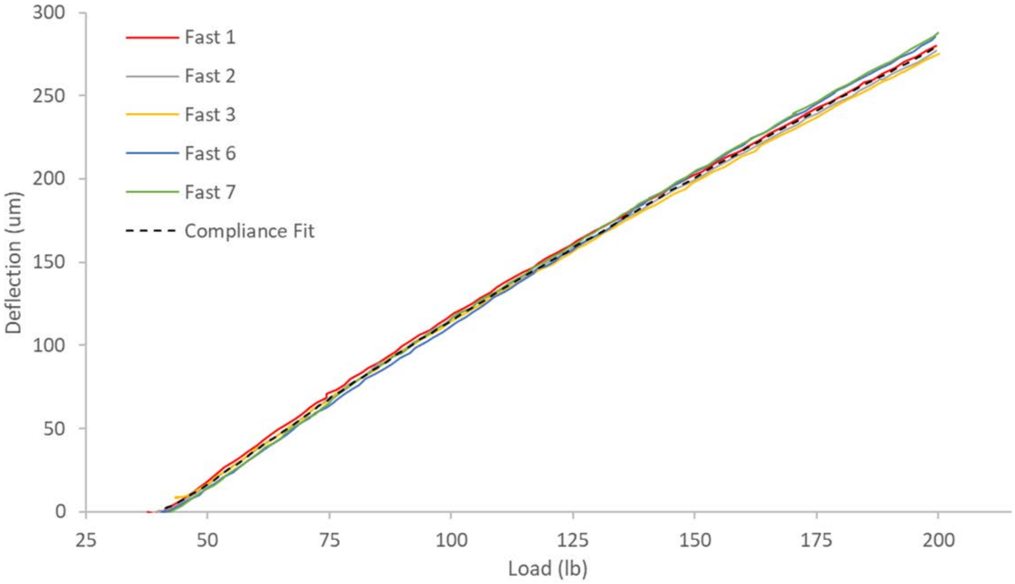

Figure 3-30: Compliance measurements for the four-point bend test in single specimen configuration in air. Many of the curves follow the same trend, however, there is some divergence at loads greater than 160 lbs. The compliance fit curve is shown by the dotted line.

Strain Measurement

To measure the strain produced in the material during the four-point bend test, multiple rows of indentation marks spaced roughly 100 µm apart were generated onto the specimen surface. The separation between the indents was measured before and after the four-point bend test using a scanning electron microscope (SEM). The change in the indent spacing after straining the material was used to measure the strain formed in different regions of the material during four-point bend test.

Deflection Measurement

To measure the deflection produced in the material during the four-point bend test, multiple measurements were completed. During the experiments completed in air at room temperature, *in situ* measurements were collected from the crosshead LVDT curve and the DVRT on the specimen surface; during experiments in the simulated-NWC environment, only the corrected LVDT measurement was used. Through both measurements the amount of plastic deformation was measured using the parallel line method to subtract the elastic deflection components. Post-straining the amount of deflection was measured *ex situ* by comparing the change in deflection for each of the leading edges through compiled SEM images as seen in Figure 3-31. A comparison of the deflection measurements for several test specimens made from 12.9 % cold-worked CP 304L material is shown in Table 3-17, where a good agreement can be observed, particularly between the corrected LVDT measurements and the SEM deflection measurements.

Figure 3-31: Compiled images of the entire Edge 1 for test specimen K-4 Air 1: a) edge pre-straining, b) edge post-straining. A clear amount of plastic deformation occurred in the center of the specimen during the straining increment. The plastic deflection is measured as the change in central 500 μm between the pre- and post-strain images.

Table 3-17: Comparison of the measurement of plastic deflection through different techniques. There is a good agreement between the cumulative corrected-LVDT measurement and the side profile measurements for the SEM. The μLVDT measurements appear to underestimate the plastic deflection in the specimen, but these measurements cannot be used for experiments in a simulated water environment.

Experiment	**Total (μm)**	**Plastic Deflection (μm)**					
		μLVDT	C-LVDT	Cumulative C-LVDT	Edge 1	Edge 2	Average
K-4 Air 1	60	19.5 ± 0.5	21.7 ± 4.1	21.7 ± 4.1	22.8 ± 1.7	19.3 ± 1.6	21.1 ± 1.6
K-4 Air 2	45	17.6 ± 0.5	20.5 ± 4.2	20.5 ± 4.2	25.2 ± 1.6	19.9 ± 1.6	22.5 ± 1.6
K-4 Air 3-1	20	5.4 ± 0.5	8.5 ± 3.7	8.5 ± 3.7	11.3 ± 1.5	6.4 ± 1.68	8.8 ± 1.6
K-4 Air 3-2	25	6.4 ± 0.5	8.7 ± 3.9	15.4 ± 3.8	16.2 ± 1.5	12.8 ± 1.5	14.5 ± 1.5
K-4 Air 3-3	28	13.4 ± 0.5	17.8 ± 4.1	30.0 ± 3.9	30.6 ± 1.6	28.2 ± 1.6	29.4 ± 1.6
K-4 NWC 1	31	N/A	18.7± 3.9	18.7± 3.9	19.2 ± 1.4	20.2 ± 1.5	19.7 ± 1.5

Strain vs. Deflection Behavior

Before evaluating the crack initiation behavior of the neutron irradiated austenitic stainless steels, four-point bend tests are being done using unirradiated stainless steel to evaluate the performance of the system in different environments. Specifically, the variation in strain produced in the material as a function of the bend deflections in the material. For the new system configuration, a series of tests were being carried out at room temperature in air and under simulated-NWC conditions using test specimens made from 12.9 % cold-worked CP 304L material. A linear correlation between strain induced in the material (as measured by the change in indent spacing) and the plastic bend deflection (as measured by the residual plastic deflection) was observed in different environment conditions as shown in Figure 3-32.

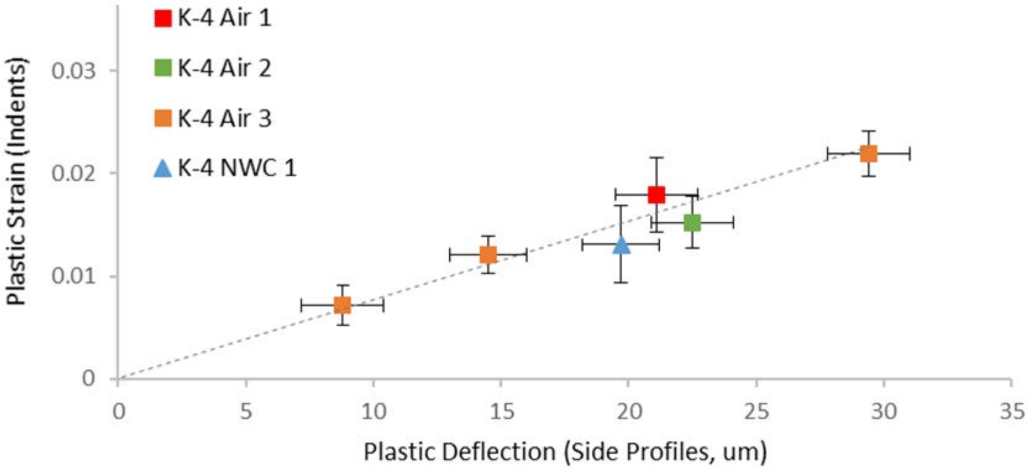

Figure 3-32: Plastic strain vs. plastic deflection for the current four-point bend test configuration. A linear correlation was observed between the plastic deflection and strain induced in the material was observed for tests in both air and simulated NWC environment.

3.6 *CGR test results*

3.6.1 304L Irradiated in Barseback 1 BWR

RCT-2: As-irradiated

Precracking

Figure 3-33 shows the crack length in terms of *a/W* and corrosion potential of RCT-2 during the precracking stage. The precracking steps were started when the corrosion potential of sample stabilized. The crack had not initiated after about 400 h at a nominal K_{max} of 18 MPa·m$^{1/2}$. In order to accelerate the precracking, K_{max} was increased to 20 MPa·m$^{1/2}$ and R was gradually decreased to 0.2. Dropping the value of R changes the loading mode from fatigue reverse loading to more of an applied tensile stress with cycling. Afterwards, the crack initiated and CGR stabilized at 3.0×10^{-6} mm/s. Then R was increased to 0.6 in steps and K_{max} was gradually decreased to 18 MPa·m$^{1/2}$, causing the CGR to decrease. Thereafter, the waveform frequency was gradually decreased to

0.001. The decreased further during these steps. The waveform was also switched to trapezoidal and then maintained at a constant *K* of 18 MPa·m$^{1/2}$. An anticipatory correction factor (CF) of 2.5 was applied to account for an underprediction of crack growth typical for austenitic steels in high temperature water. Post-test, the actual SCC crack length was determined and used to correct both the CGRs and the *K* values.

Changing environment

To study the effect of hydrogen environment, the environment was switched from NWC to HWC as the CGR stabilized at 1.8×10^{-6} mm/s. Nominal *K* was kept at 18 MPa·m$^{1/2}$. As shown in Figure 3-34, the CGR dropped significantly to 2.6×10^{-7} mm/s after the switch. Then the environment was switched back to NWC and the CGR increased to a value of 1.9×10^{-6} mm/s, which is very consistent with the previous value obtained in NWC. During this process, no action was taken to control the outlet conductivity which ranged between 0.055 and 0.085 µS/cm when the environment stabilized.

Conductivity has a significant effect on the CGR. In order to study the effect of conductivity on the CGR, dilute H_2SO_4 solution was injected into the main water column via a peristaltic pump. As shown in Figure 3-35, when the outlet conductivity was increased from 0.075 to 0.2 µS/cm, the CGR increased from 1.9×10^{-6} mm/s to 3.7×10^{-6} mm/s. As the conductivity was further decreased to ~0.1 µS/cm, CGR dropped to 3.2×10^{-6} mm/s. The outlet conductivity was maintained at ~0.1 µS/cm thereafter.

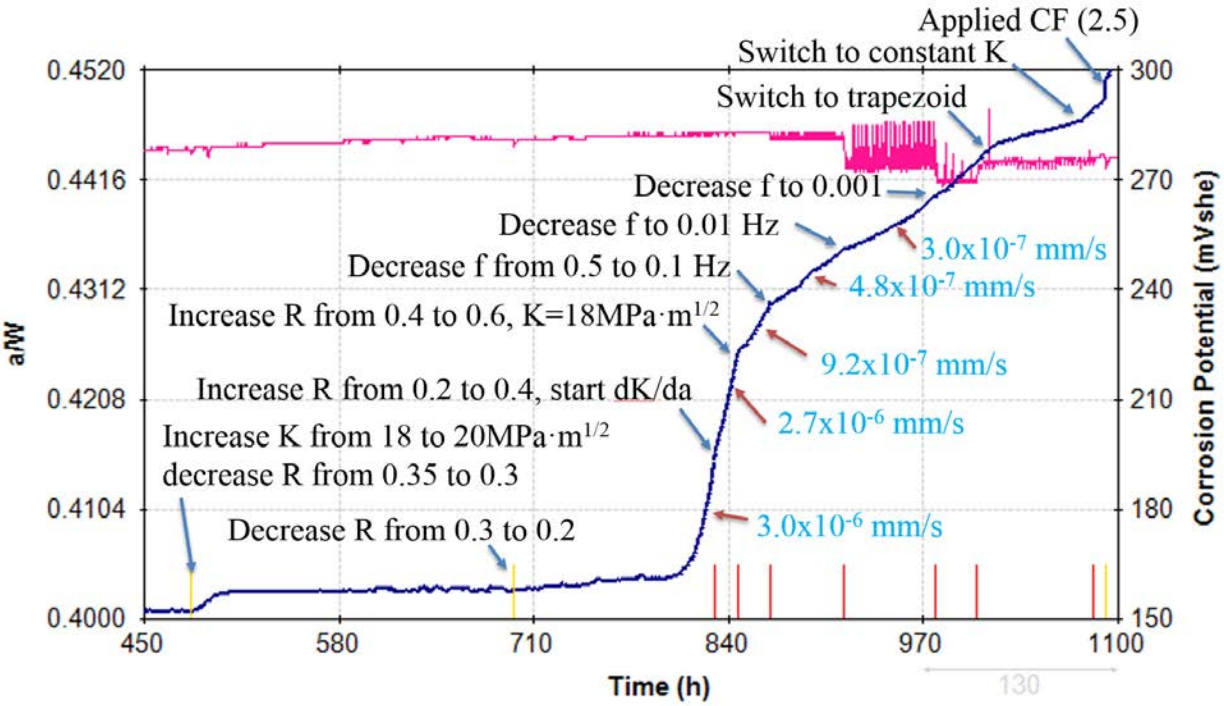

Figure 3-33: Crack length and corrosion potential of RCT-2 in 288 °C water containing 2 ppm O_2 during precracking stage.

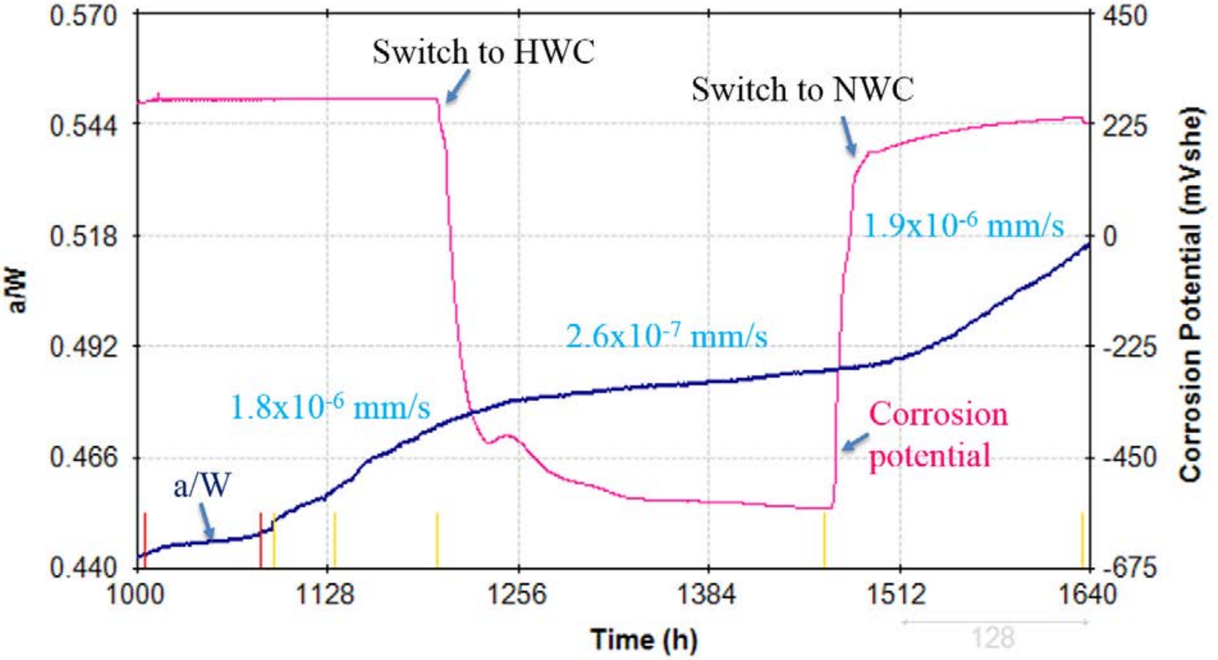

Figure 3-34: Crack length and corrosion potential of RCT-2 in 288 °C water at a nominal *K* of 18 MPa·m$^{1/2}$ during the change of corrosion potential.

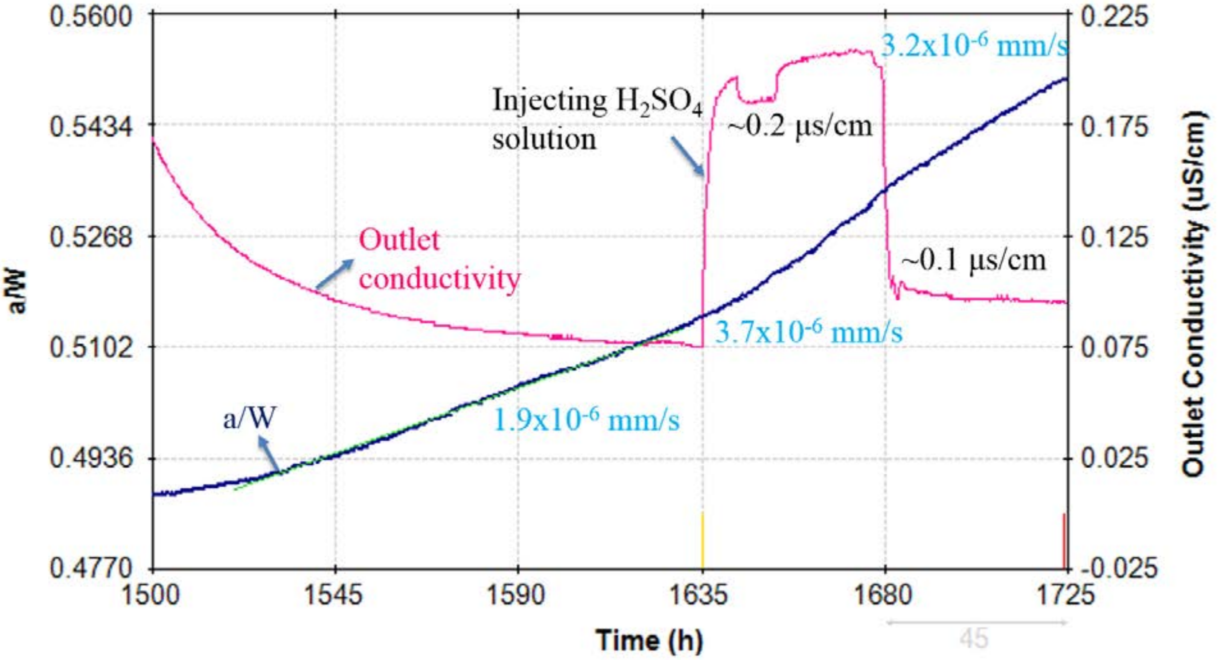

Figure 3-35: Crack length and corrosion potential of RCT-2 in 288 °C water containing 2 ppm O_2 at a nominal *K* of 18 MPa·m$^{1/2}$ during the change of conductivity.

Decreasing *K*

In order to study the CGR dependence on *K*, the nominal *K* value was first dropped from 18 to 14 MPa•m$^{1/2}$ and then to 11MPa•m$^{1/2}$. As shown in Figure 3-36, the CGR dropped from 3.2×10^{-6} mm/s to 6.7×10^{-7} mm/s as *K* was decreased from 18 to 14 MPa•m$^{1/2}$. Then the CGR decreased to 9.5×10^{-8} mm/s as *K* was further dropped to 11 MPa•m$^{1/2}$.

The effect of corrosion potential was also studied at nominal *K* of 11 MPa•m$^{1/2}$. As shown in Figure 3-37, CGR decreased from 9.5×10^{-8} mm/s to 2.3×10^{-8} mm/s after the switch from NWC to HWC.

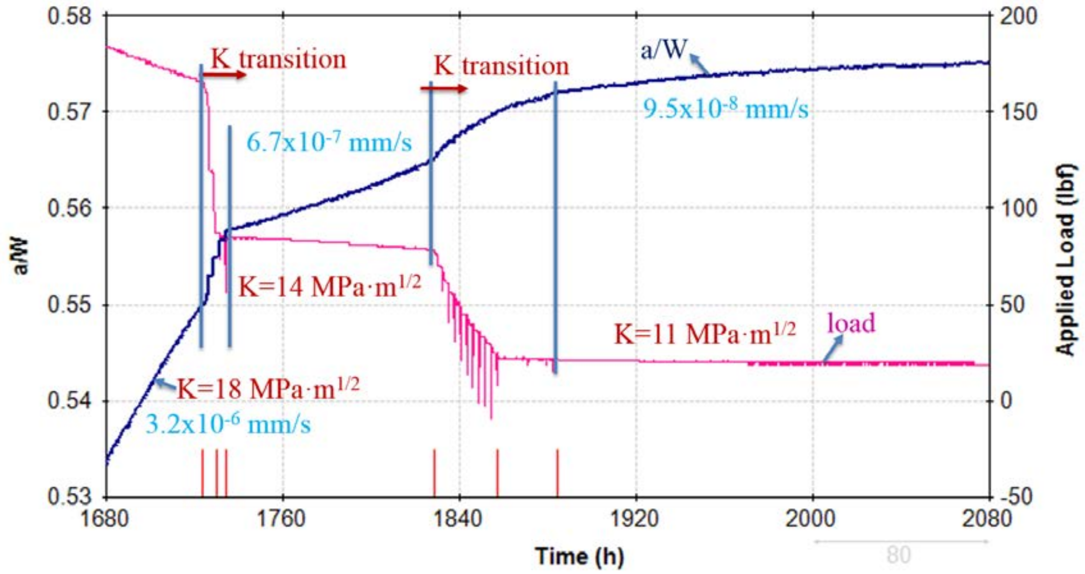

Figure 3-36: *a/W* and applied load of RCT-2 in 288 °C water containing 2 ppm O_2 during the change of corrosion potential.

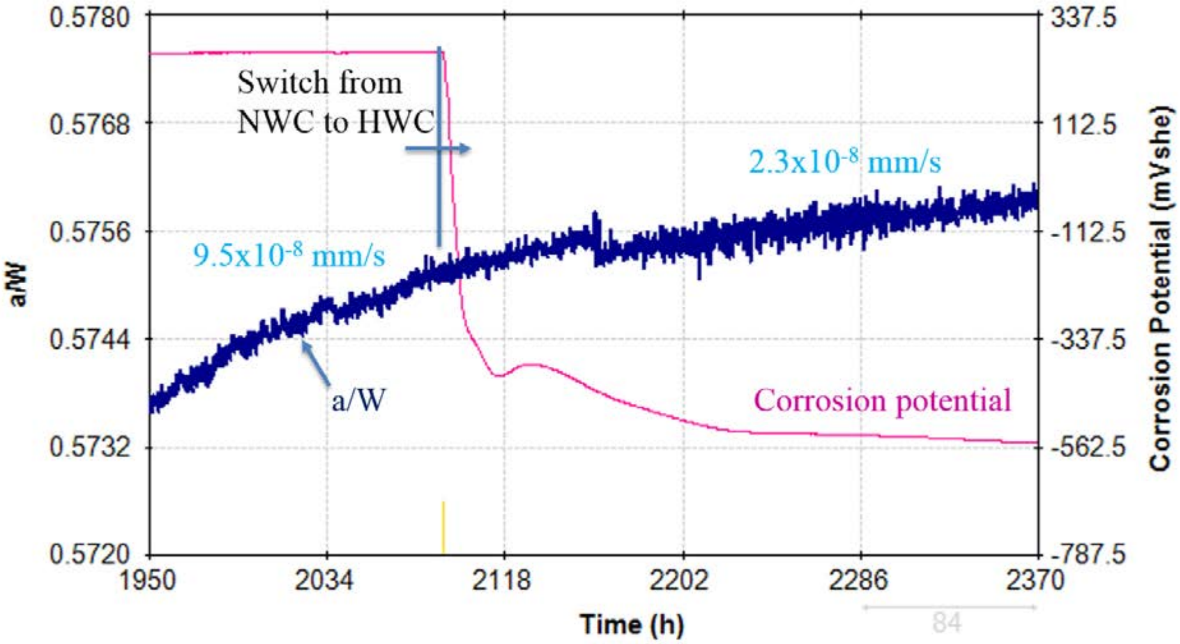

Figure 3-37: Crack length and corrosion potential of RCT-2 in 288 °C water at a nominal *K* of 11 MPa·m$^{1/2}$ during the change of corrosion potential.

Fracture surface analysis

The sample was opened and the fracture surface was observed with SEM. Figure 3-38 shows a portion of the fracture surface and a section of the side of the specimen. The images show that the crack is in plane and follows the side grooves well.

Figure 3-39 shows the plane view image of fracture surface. The fracture surface is intergranular except the pre-cracking and the post-cracking region. The pre-cracking region is not even. The SCC region is mainly intergranular and no significant ligament was found. Nevertheless, DCPD still underestimated the real CGR even when anticipatory correction factor was applied.

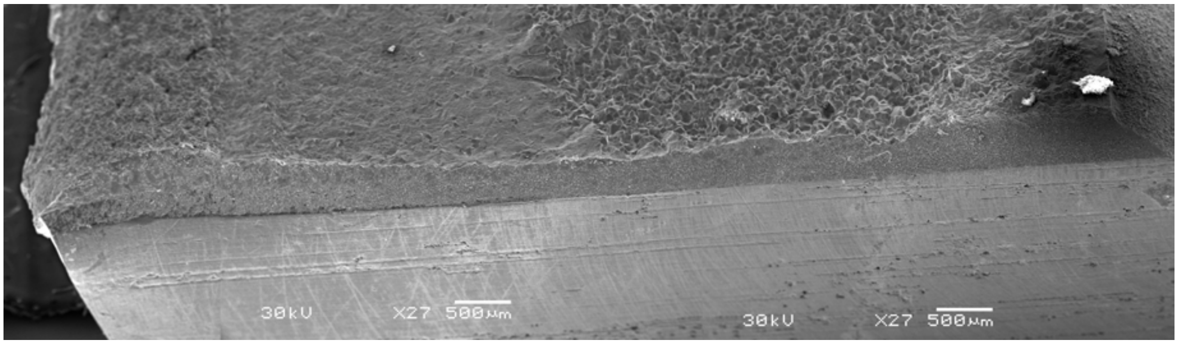

Figure 3-38: Side view image of fracture surface of RCT-2.

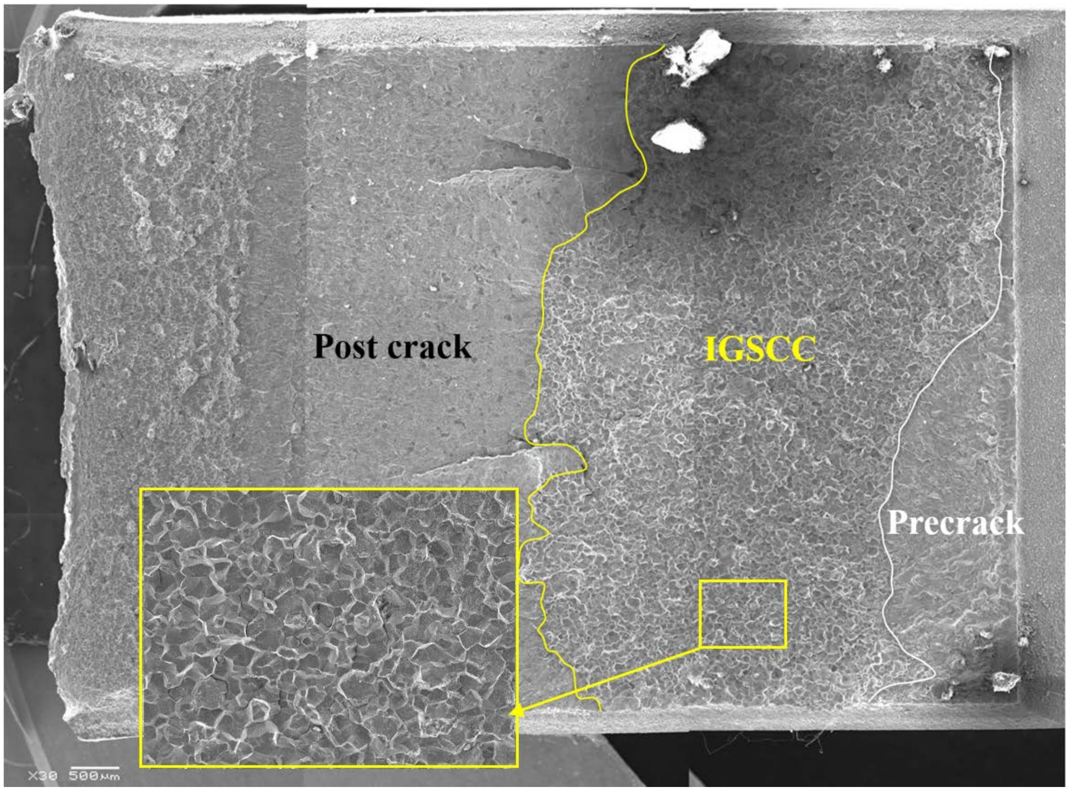

Figure 3-39: Fracture surface of RCT-2.

DCPD Estimation and Actual CGR

The crack lengths measured by both DCPD and SEM are listed in Table 3-18. For the pre-crack region, the length measured by DCPD is close to the real length even though the crack front is not straight. DCPD underestimated the crack length for the IGSCC region. The crack lengths measured by DCPD and from the SEM images were compared for precrack and IGSCC regions in table 3-18. From the comparisons, correction factors for the DCPD crack length measurements were made. The correction factors were used to correct all of the DCPD crack length measurements. Based on the corrected crack lengths, corresponding corrected stress intensity (*K*) values were also calculated. Validity of stress intensities calculated by this means was checked using the corrected *K* values and the yield strength of this sample as measured by a matching tensile experiment: 685.5 MPa at 288 °C. The results of the K-validity checks for this, and other tested samples, are given in Table 3-22.

Table 3-18: Results of crack length measurements and correction factor for RCT-2.

	Pre-Crack	IGSCC
Length by DCPD (mm)	0.775	2.073
Length by SEM (mm)	0.737	3.83
Correction factor	0.95	1.85

RCT-3: PIA 550^{o}C:20 hr

Precracking

Figure 3-40 shows the *a/W* and corrosion potential of RCT-3 during precracking stage. The precracking steps were started when the corrosion potential of sample stabilized. Nominal K_{max} was set to 18 MPa∙m$^{1/2}$. The CGR decreased as *R* was increased from 0.4 to 0.6. It decreased further as the frequency was decreased. The CGRs on the graph have been corrected after the fracture surface was analyzed.

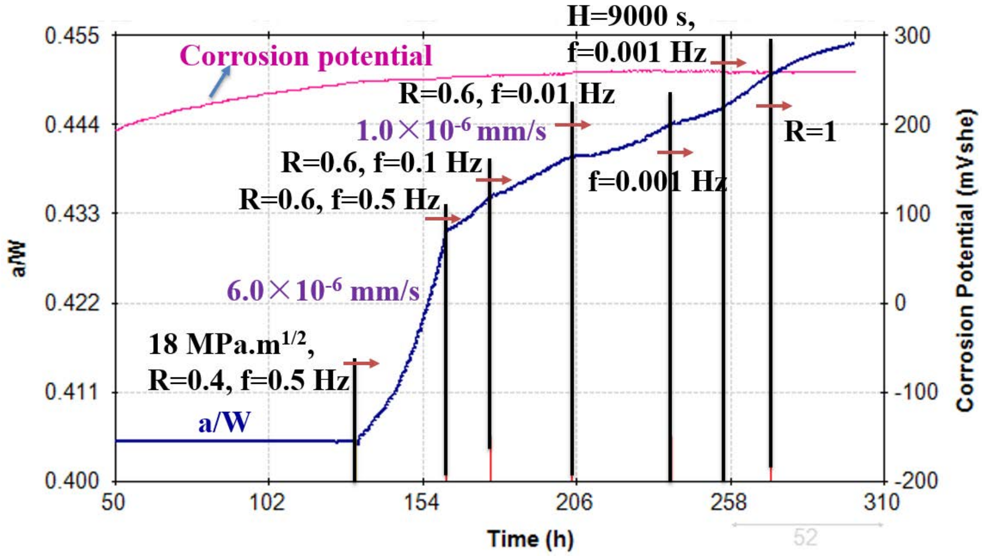

Figure 3-40: *a/W* and corrosion potential of RCT-3 in 288 ^{o}C water containing 2 ppm O_2 during precracking stage.

Changing environment

To study the effect of hydrogen, the environment was switched from NWC to HWC as the CGR stabilized at 5.9×10^{-7} mm/s. Nominal *K* was kept at 18 MPa∙m$^{1/2}$. As shown in Figure 3-41, the CGR dropped significantly to 1.5×10^{-8} mm/s after the switch. Then the environment was switched back to NWC, requiring ~650 hr before the CGR stabilized at a value of 6.6×10^{-7} mm/s, which was very consistent with the previous value in NWC. There are some jumps in *a/W* (up to 0.002) which may be due to the break of ligaments on the crack propagation path. Such jumps have also been reported in the results from the sample of the same heat [1].

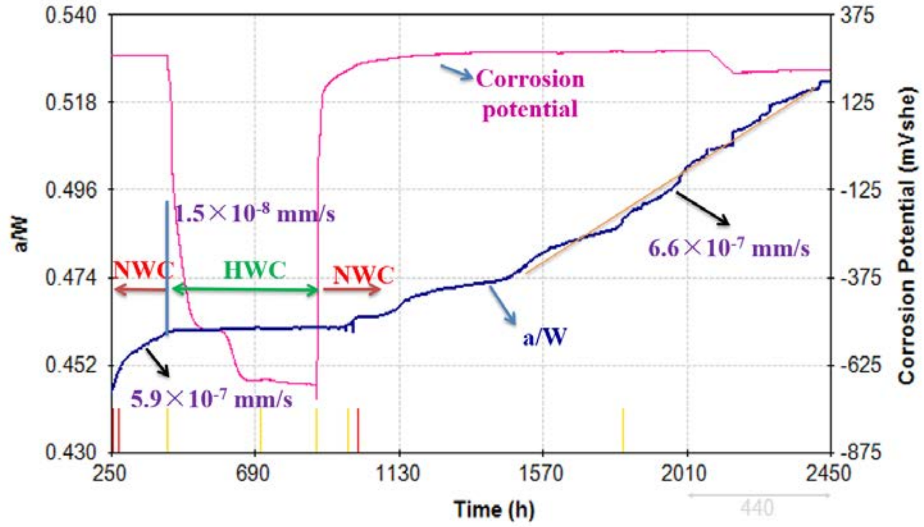

Figure 3-41: *a/W* and corrosion potential of RCT-3 in 288 ^{o}C water at a nominal *K* of 18 MPa·m$^{1/2}$ during the change of corrosion potential.

<u>Decreasing *K*</u>

In order to study the CGR dependence on *K*, the nominal *K* value was dropped from 18 to 14 MPa·m$^{1/2}$. As shown in Figure 3-42, there was a large jump in *a/W* (~0.033) after the *K* was held at 14 MPa·m$^{1/2}$. It is very unusual to see such a large jump. This jump was confirmed to be due to the fracture of the ligament on the fracture surface which is shown in Figure 3-43. The CGR at 14 MPa•m$^{1/2}$ finally stabilized at 2.9×10^{-7} mm/s. Then *K* was further dropped to 11 MPa•m$^{1/2}$. Unexpectedly, two large jumps in *a/W* (over 0.14) occurred. The final *a/W* was around 0.92 when the test was stopped.

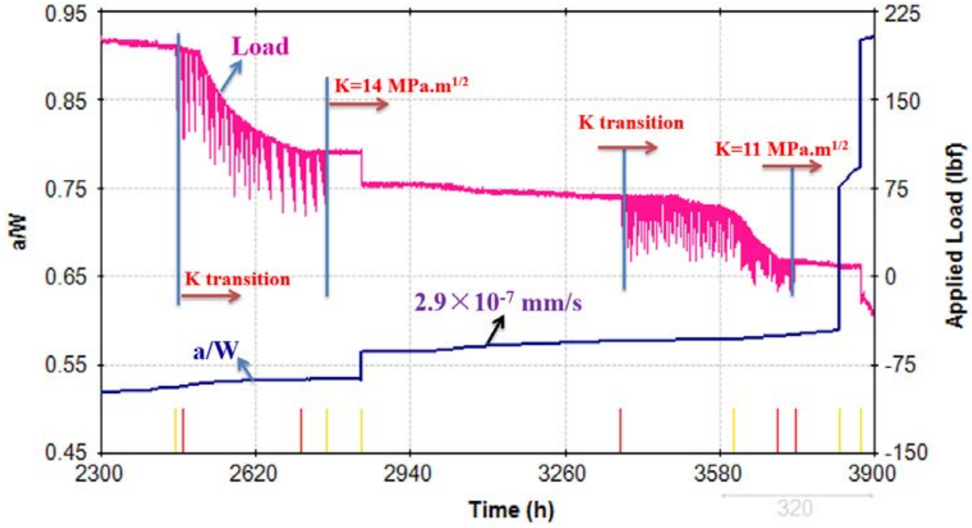

Figure 3-42: *a/W* and applied load of RCT-3 in 288 ^{o}C water containing 2 ppm O_2 during *K* transition from 18 to 11 MPa·m$^{1/2}$.

Fracture surface analysis

The sample was opened and the fracture surface was observed with SEM. Figure 3-43 shows a portion of the fracture surface and a section of the opposite sides of the specimen. The images show that the crack is in plane and follows the side grooves.

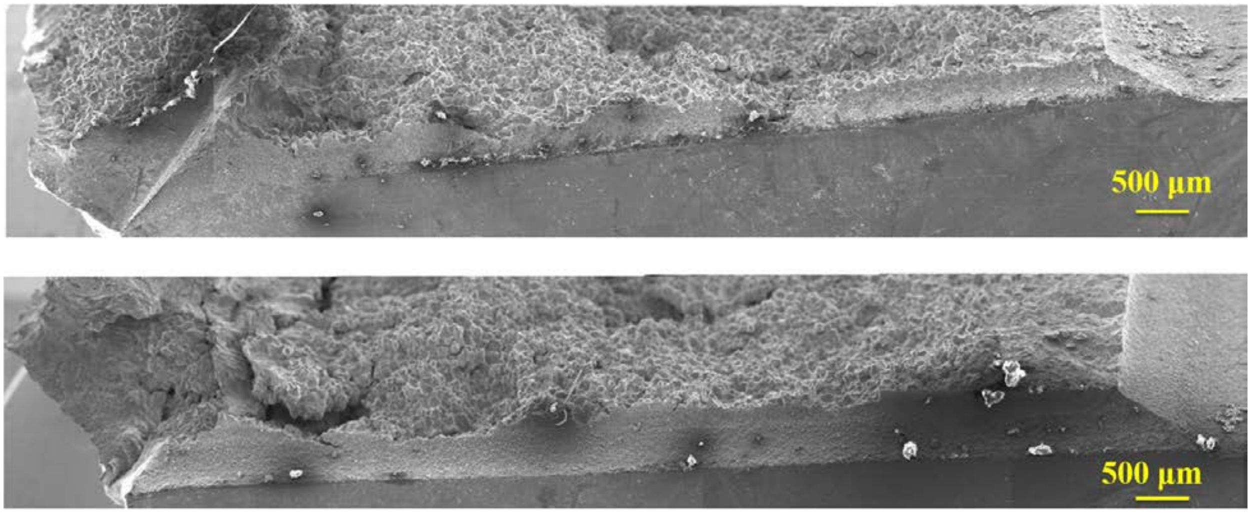

Figure 3-43: Side view images of fracture surfaces of RCT-3.

Figure 3-44 shows the plane view image of fracture surface. The fracture surface is intergranular except for the pre-cracked and the post-test fracture regions, which are due to cyclic loading and mechanical overloading at room temperature respectively. The large crack on the left side was due to the post-test loading procedure. It should be noted that there is a ligament between the upper part and the lower part in the IGSCC region. The enlarged images from the starting and ending parts of the boundary show that the two parts of IGSCC region are not on the same plane and the interface between them is a transgranular ligament that is almost perpendicular to the fracture surface. Such an ligament would not crack open until the opening of the main crack is larger than the distance between the two crack propagating planes. So, the main crack front should be beyond the crack front at the interface. The could explain why DCPD underestimated the crack length. The jumps in *a/W* were probably was caused by the sudden opening of the interface.

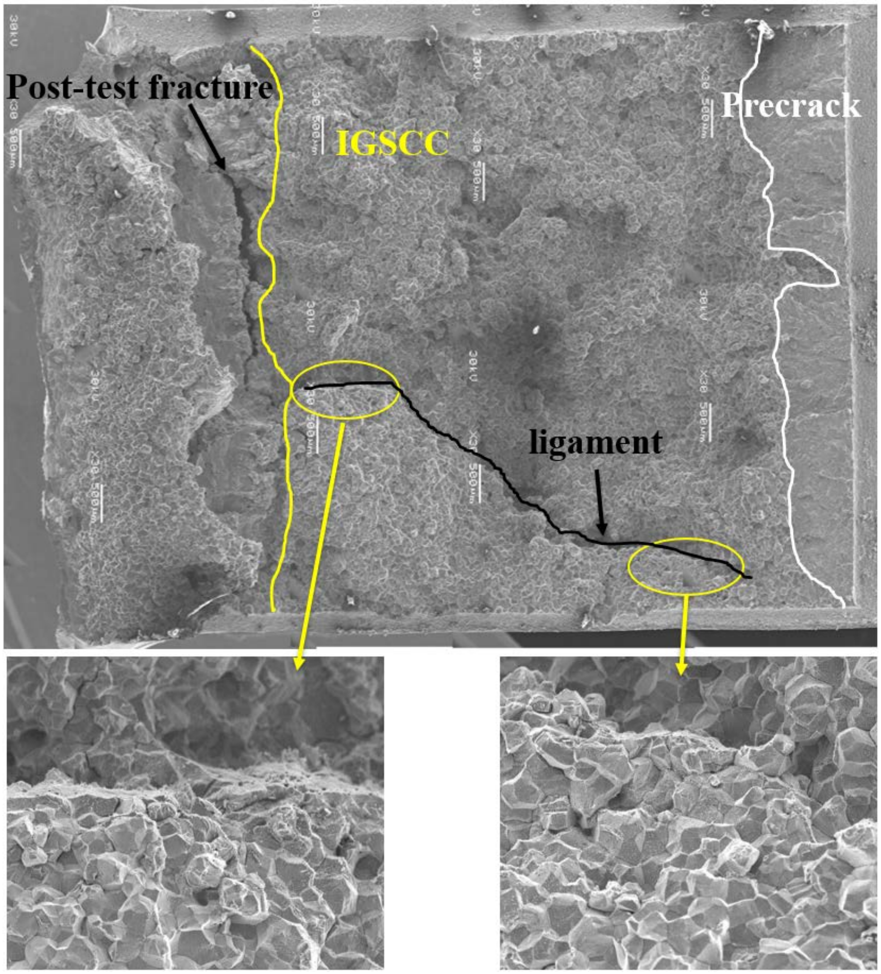

Figure 3-44: Fracture surface of RCT-3.

<u>DCPD Estimation and Actual CGR</u>

The crack lengths measured by DCPD and SEM are listed in Table 3-19. The post-cracking correction factor is the ratio between the real length (by SEM) and the length measured by DCPD. For the pre-crack region, the length measured by DCPD is close to the real length. However, DCPD under estimated the crack length significantly for the IGSCC region (even with the pre-test correction factor). Therefore, the CGRs measured by DCPD were adjusted with the post-cracking correction factors listed in Table 3-19. Meanwhile, the *K* values were also recalculated with the applied load and the corrected crack length. The *K* validity was checked using the corrected *K* values and the yield strength of this sample as measured by a matching tensile experiment: 421.3 MPa at 288 ^{o}C (Table 3-9). The results were listed previously in Table 3-22. It should be mentioned that this sample has been aggressively annealed and showed strain hardening during the tensile test of the same heat treatment condition. So, adjustment of the yield stress by ΔYS/3 for K validity check would be over stringent.

Table 3-19: Results of crack length measurements and correction factor for RCT-3.

	Pre-Crack	IGSCC
Length by DCPD (mm)	0.725	2.157
Length by SEM (mm)	0.856	6.018
Correction factor	1.18	2.79

RCT-4: PIA 550ºC:5 hr

Precracking

Figure 3-45 shows the *a/W* and corrosion potential of RCT-4 during precracking stage. The precracking steps were started when the corrosion potential of sample stabilized. Haversine waveform was started at a nominal K_{max} of 18 MPa·m$^{1/2}$ with R of 0.6 and f of 0.5 Hz. The crack growth rate stabilized at 1.5×10^{-5} mm/s. Then f was decreased to 0.1 Hz, which caused CGR to decrease. Thereafter, the waveform frequency was gradually decreased to 0.001. CGR further decreased during these steps. The waveform was switched to trapezoid and then maintained at constant *K* of 18 MPa·m$^{1/2}$. The outlet conductivity was maintained around 0.1 µS/cm throughout the test. The CGRs on the graph have been corrected after the fracture surface was analyzed.

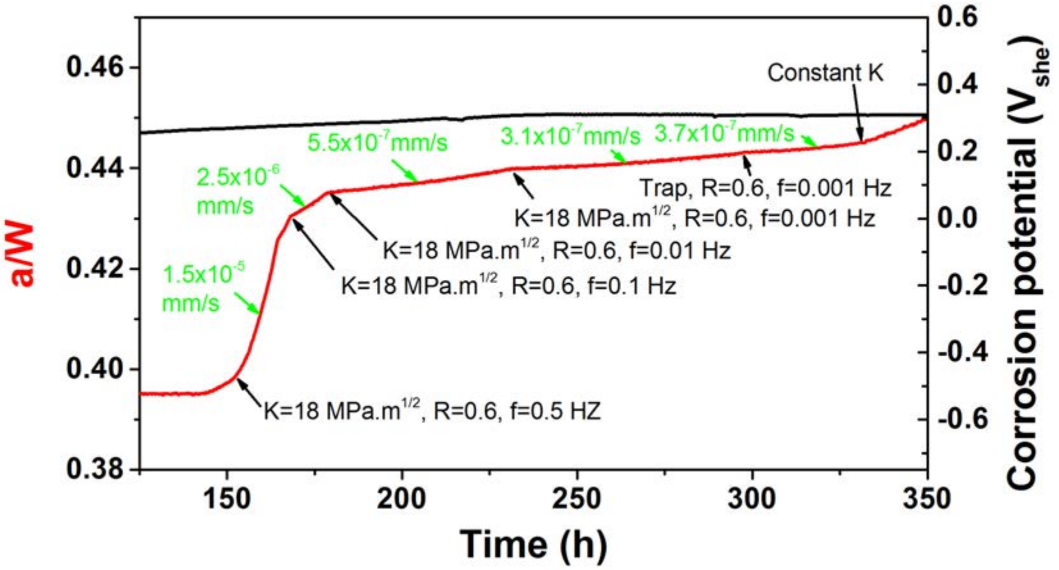

Figure 3-45: *a/W* and corrosion potential of RCT-4 in 288 °C water containing 2 ppm O_2 during precracking stage.

Changing environment

The effect of hydrogen environment was studied at a constant K of 18 MPa·m$^{1/2}$. As shown in Figure 3-46, the CGR stabilized at 1.1×10^{-6} mm/s in NWC first. Then the environment was switched to HWC and the CGR decreased to 9.7×10^{-9} mm/s. Thereafter, the environment was switched back to NWC and the CGR increased back to 9.7×10^{-7} mm/s after a lag. The CGRs in NWC were very consistent with each other. An anticipatory correction factor (CF) of 2.5 was applied in the DCPD program.

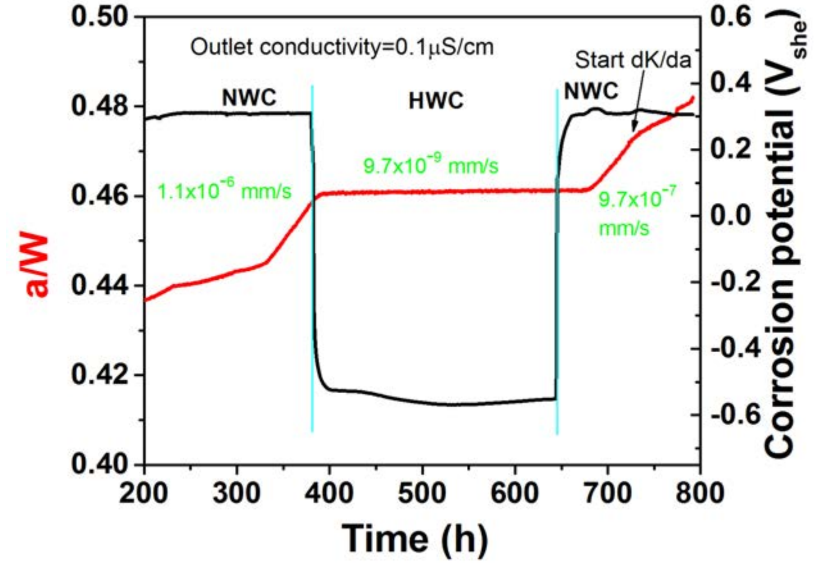

Figure 3-46: *a/W* and corrosion potential of RCT-4 in 288 ^{o}C water at a nominal *K* of 18 MPa·m$^{1/2}$ during the environment change.

Decreasing *K*

Three *K* (18, 14 and 11 MPa·m$^{1/2}$) values were used to study the K dependence of CGR. As shown in Figure 3-47, the CGR dropped to 2.9×10^{-7} mm/s as the nominal *K* value was decreased from 18 to 14 MPa·m$^{1/2}$. Then *K* was further dropped to 11 MPa•m$^{1/2}$ and the CGR changed slightly.

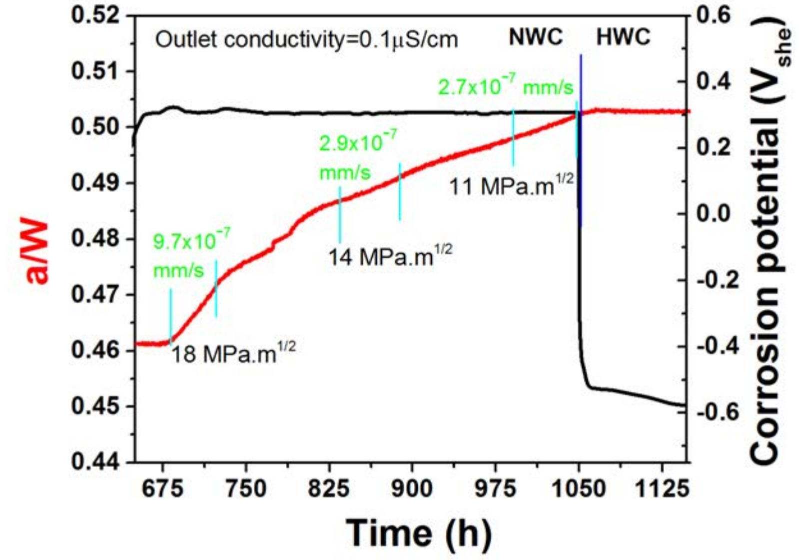

Figure 3-47: *a/W* and corrosion potential of RCT-4 in 288 ^{o}C water at a nominal *K* of 18 MPa·m$^{1/2}$ during the *K* change.

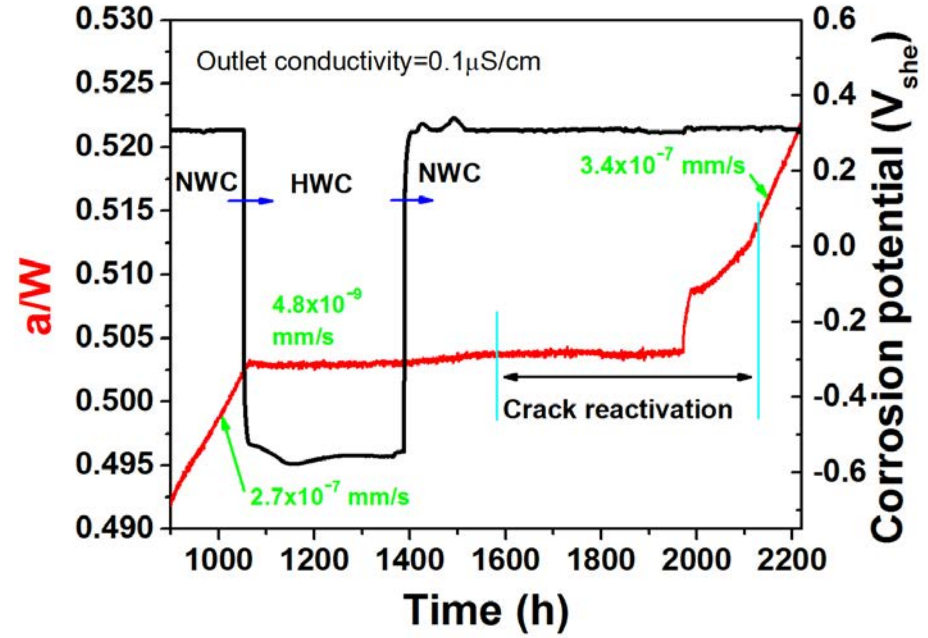

Figure 3-48: *a/W* and corrosion potential of RCT-4 in 288 ^oC water at a nominal *K* of 11 MPa·m$^{1/2}$ during the environment change.

<u>Fracture surface analysis</u>

The sample was opened and the fracture surface was observed with SEM. Figure 3-49 shows the plan view of fracture surface. The images show that the crack is in plane and follows the side grooves well. Different regions were marked on Figure 3-49. The precrack region is fully transgranular and the front is quite even. The IGSCC region is fully intergranular although the front is crooked. No significant ligament was observed in the IGSCC region.

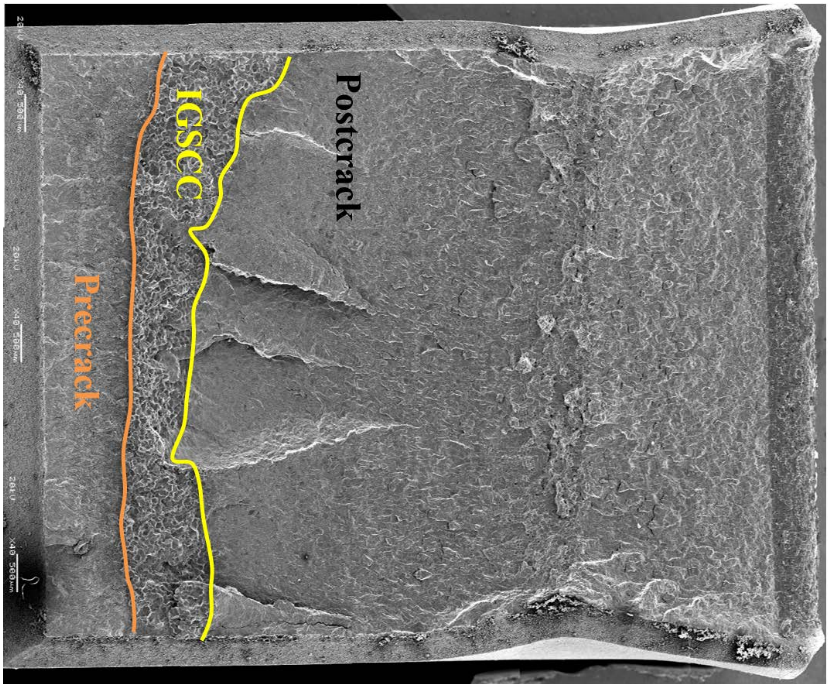

Figure 3-49: Fracture surface of RCT-4.

<u>DCPD Estimation and Actual CGR</u>

The crack lengths measured by DCPD and SEM are listed in Table 3-20. The post-cracking correction factor is the ratio between the real length (by SEM) and the length measured by DCPD. As shown in Table 3-20, DCPD overestimated the IGSCC region a little while it underestimated the precrack region. The CGRs measured by DCPD were adjusted with the post-cracking correction factors listed in Table 3-20. Meanwhile, the *K* values were also recalculated with the applied load and the corrected crack length. The *K* validity was checked using the corrected *K* values and the yield strength of this sample as measured by a matching tensile experiment:483.7 MPa at 288^{o}C (Table 3-9). The results are listed in Table 3-22.

Table 3-20: Results of crack length measurements and correction factor for RCT-4.

	Pre-Crack	IGSCC
Length by DCPD (mm)	0.802	1.234
Length by SEM (mm)	1.103	1.076
Correction factor	1.38	0.87

RCT-1: PIA 500^{o}C:1 hr

Precracking

Figure 3-50 shows the *a/W* and corrosion potential of RCT-1 during precracking stage. Havsine waveform was started at a nominal K_{max} of 20 MPa∙m$^{1/2}$ with R of 0.6 and f of 1 Hz. Then the nominal K_{max} was decreased to 18 MPa∙m$^{1/2}$ with a f of 0.5 Hz. Afterwards, f was gradually decreased to 0.001 Hz and CGR decreased accordingly. The waveform was switched to trapezoid and then maintained at constant *K* of 18 MPa∙m$^{1/2}$. An anticipatory correction factor of 2.5 was applied after switch to constant *K*. The outlet conductivity was maintained around 0.1 µs/cm ever since. The CGRs on the graph have been corrected after the fracture surface was analyzed.

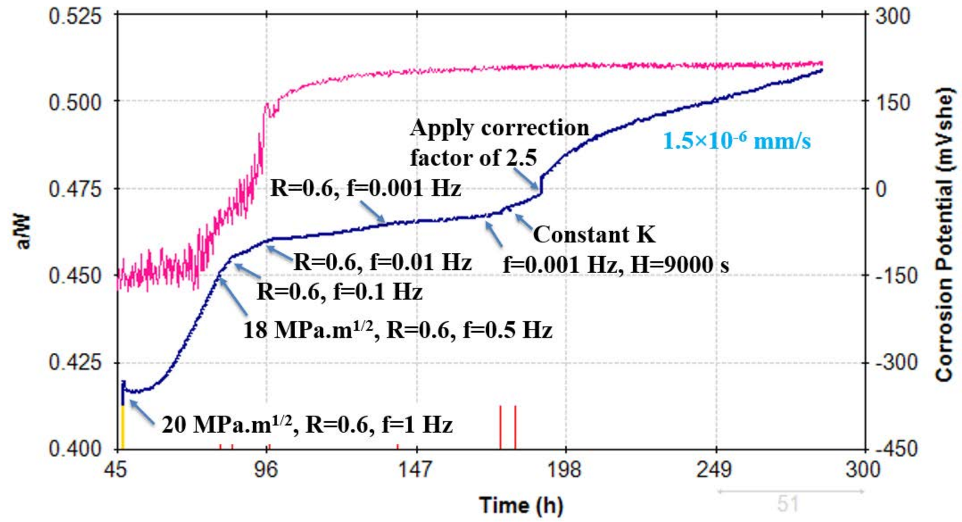

Figure 3-50: *a/W* and corrosion potential of RCT-1 in 288 ^{o}C water containing 2 ppm O_2 during precracking stage.

Changing environment

The effect of hydrogen environment was studied at a constant *K* of 18 MPa∙m$^{1/2}$. As shown in Figure 3-51, the CGR stabilized at 1.5×10^{-6} mm/s in NWC first. Then the environment was switched to HWC. The corrosion potential dropped significantly and the CGR decreased to 9.3×10^{-8} mm/s. Thereafter, the environment was switched back to NWC and the CGR increased up to 2.7×10^{-6} mm/s after a lag.

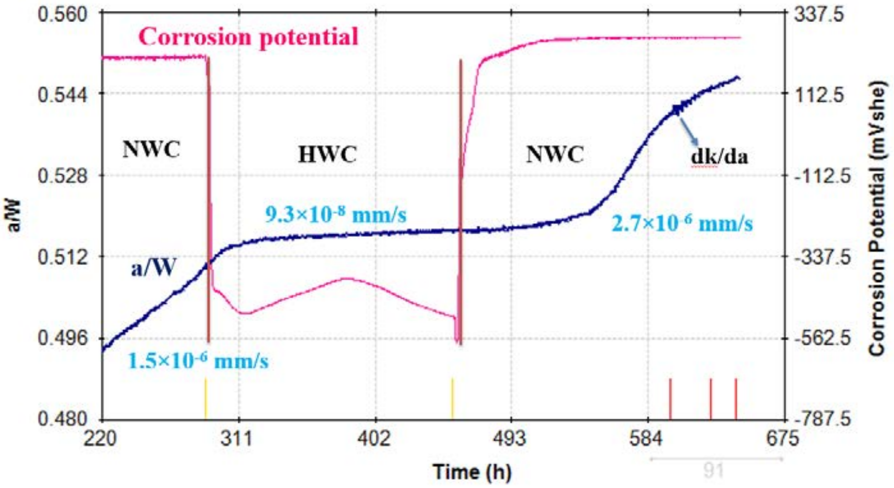

Figure 3-51: *a/W* and corrosion potential of RCT-4 in 288 ^{o}C water at a nominal *K* of 18 MPa•m$^{1/2}$ during the environment change.

<u>Decreasing *K*</u>

Three *K* (18, 14 and 11 MPa•m$^{1/2}$) values were used to study the *K* dependence of CGR. d*K*/d*a* function was used to change the *K* value. Figure 3-52 shows the applied load and *a/W* during the *K* change. The CGR dropped from 2.7×10^{-6} to 8.2×10^{-7} mm/s as the nominal *K* value was decreased from 18 to 14 MPa•m$^{1/2}$. Then *K* was further dropped to 11 MPa•m$^{1/2}$ and the CGR further dropped. The effect of corrosion potential was also studied at nominal *K* of 11 MPa•m$^{1/2}$. As shown in Figure 3-53, right after the *K* was maintained at 11 MPa•m$^{1/2}$, the *a/W* curve fluctuated a little which may be caused by unevenness of the crack front. So trapezoid waveform was started in order to break some small ligaments and switched back to constant *K* afterwards. CGR finally stabilized at 2.8×10^{-7} mm/s. It decreased to 1.8×10^{-8} mm/s after the switch from NWC to HWC.

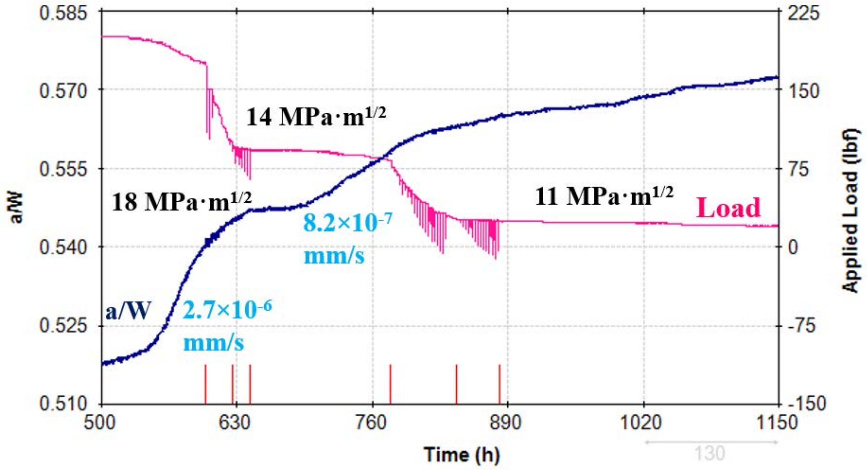

Figure 3-52: *a/W* and applied load of RCT-1 in 288 ^{o}C water containing 2 ppm O_2 during the *K* change.

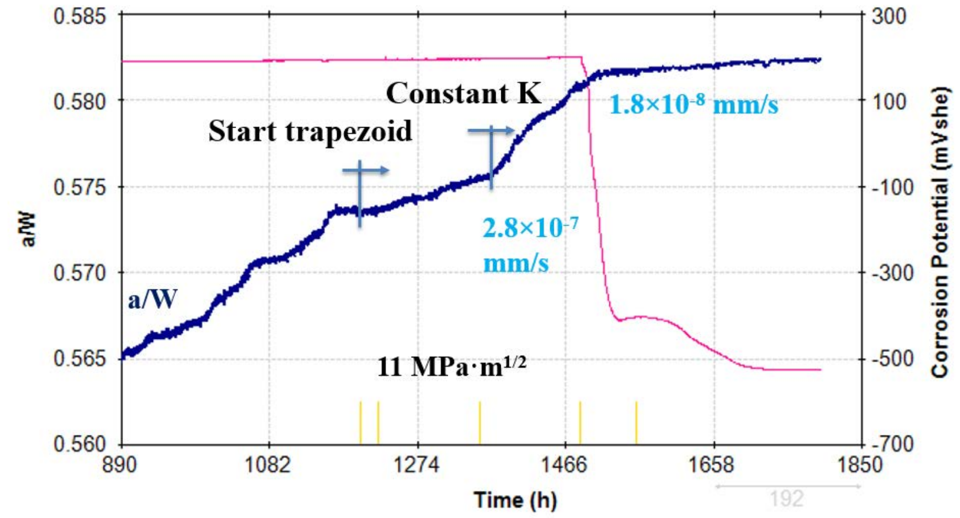

Figure 3-53: *a/W* and corrosion potential of RCT-4 in 288 ^oC water at a nominal *K* of 11 MPa·m$^{1/2}$ during the environment change.

Fracture surface analysis

The sample was opened by fatigue and the fracture surface was analyzed with SEM. Figure 3-54 shows the plan view of fracture surface. The images show that the crack is in plane and follows the side grooves well. Different regions were marked on Figure 3-54. The precrack region is fully transgranular and the front is quite even. The IGSCC region is mainly intergranular. However, the front of IGSCC region is not even as there is a broken ligament near the middle, as shown in the insert.

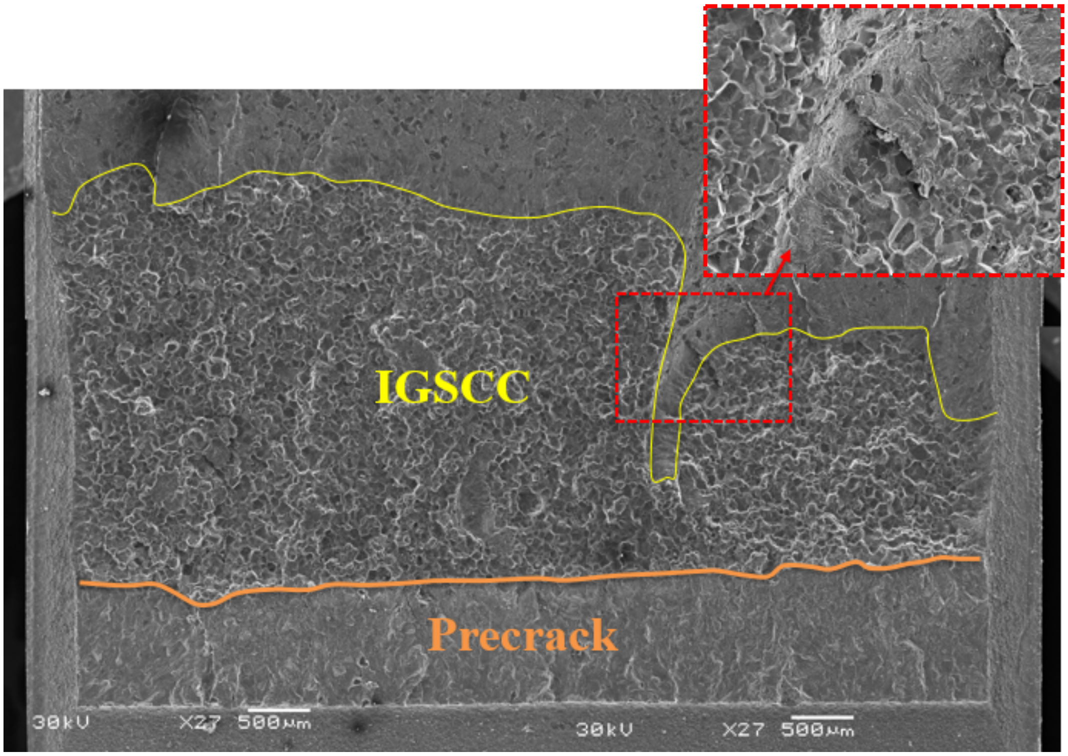

Figure 3-54: Fracture surface of RCT-1.

DCPD Estimation and Actual CGR

The crack lengths measured by DCPD and SEM are listed in Table 3-21. The post-cracking correction factor is the ratio between the real length (by SEM) and the length measured by DCPD. As shown in Table 3-21, DCPD underestimated both the IGSCC region and the precrack region. The CGRs measured by DCPD were adjusted with the post-cracking correction factors listed in Table 3-21. Meanwhile, the *K* values were also recalculated with the applied load and the corrected crack length. The *K* validity was checked using the corrected *K* values and the yield strength of this sample as measured by a matching tensile experiment:633.4 MPa at 288 ^{o}C (Table 3-9). The results are listed in Table 3-22.

Table 3-21: Results of crack length measurements and correction factor for RCT-1.

	Pre-Crack	IGSCC
Length by DCPD (mm)	0.831	1.831
Length by SEM (mm)	1.012	2.639
Correction factor	1.22	1.44

Table 3-22: Corrected *K* values and CGRs of RCT samples.

Sample	**Environment**	**Corrected *K* (MPa·m$^{1/2}$)**	**Corrected CGR (mm/s)**	**Δa* (μm)**	**Valid?****	***K* validity, %**		
						E399	ΔYS/2	ΔYS/3
RCT-2 (as-irradiated)	NWC	19.9~19.1	1.8×10^{-6}	753	Y			98
	HWC	19.5~19.8	2.6×10^{-7}	179	Y			104
	NWC	23.3~25.0	3.2×10^{-6}	494	N			143
	NWC	20.1~20.9	6.7×10^{-7}	239	N			128
	NWC	17.0~17.3	9.5×10^{-8}	96	Y			111
	HWC	17.3~17.4	2.3×10^{-8}	18	Y			112
RCT-3 (PIA:550° C:20 hr)	NWC	18.9~19.5	5.9×10^{-7}	269	Y	82		
	HWC	19.5~19.6	1.5×10^{-8}	45	Y	84		
	NWC	19.7~31.3	6.6×10^{-7}	2784	Y	117		
RCT-4 (PIA:550° C:5 hr)	NWC	19.2~19.3	1.1×10^{-6}	182	Y		107	
	HWC	19.3	9.7×10^{-9}	17	Y		107	
	NWC	19.4~19.5	9.7×10^{-7}	141	Y		108	
	NWC	14.6	2.9×10^{-7}	56	Y		81	
	NWC	11.4	2.7×10^{-7}	53	Y		63	
	HWC	11.4	4.8×10^{-9}	4	Y		63	
	NWC	11.3	3.4×10^{-7}	98	Y		63	
RCT-1 (PIA:500° C:1 hr)	NWC	19.5	1.5×10^{-6}	414	Y			110
	HWC	20.0	9.3×10^{-8}	52	Y			113
	NWC	20.6	2.7×10^{-6}	423	Y			119
	NWC	16.7	8.2×10^{-7}	235	Y			101
	NWC	13.9	2.8×10^{-7}	110	Y			89
	HWC	14.1	1.8×10^{-8}	16	Y			90

*The crack growth length for each stage was picked when the CGR stabilized.

**The CGR data is consider valid when the applied K value is less than 120% of the maximum allowable K.

4 DISCUSSION

To better understand the cracking behavior in irradiated austenitic stainless steels, the discussion section of this report is divided into following three sections: role of environment, role of annealing treatment and role of dislocation channeling on cracking behavior. Both crack initiation and crack propagation are addressed.

4.1 *Role of Environment on IASCC*

Since multiple tensile bars for same heat were available at similar damage levels, the role of environment on cracking behavior in alloys irradiated in BOR-60 reactor was studied using the CERT testing method. The primary difference between the three environment conditions is the electrochemical corrosion potential (ECP) of the material which was measured to be 215 mV, -570 mV and -860 mV (vs SHE) for NWC, HWC and PWR environments respectively. The results have previously been published as part of the detailed report on the crack initiation for these materials [14].

4.1.1 Crack Initiation

The effect of environment on crack initiation was studied mainly through CERT tests. While CERT tests pulled to failure include both crack initiation and crack growth, they spend most of their time in the initiation stage as the growth stage in this type of test for irradiated samples is typically very short. Figure 4-1a shows the effect of environment conditions of the cracking behavior of the neutron irradiated CIR alloys in CERT tests in NWC (200 mV_{SHE}), HWC (-590 mV_{SHE}) and PW (-860 mV_{SHE}).

Reduction in the ECP imposed on the material resulted in a reduction in the cracking susceptibility with the material being least susceptible to cracking in primary water (PW) environment. Alloy BR, which is the cold worked type 316 stainless steel alloy, showed low cracking susceptibility in all the environments. Other than this one exception, all the alloys showed an increase in cracking susceptibility at higher ECP levels as measured by % IG fracture. This increase in the % IG indicates that the cracking susceptibility of the material (crack initiation + growth) is highly dependent on the environment to which it is exposed. An increase in the aggressiveness of the environment (higher ECP) results in an increased potential for cracking.

Alloy composition also plays a role in cracking behavior. Although alloys AS and SW are both commercial purity alloys with similar damage levels (AS 5.5 dpa, SW 4.4 dpa) the cracking behavior is different between them. Alloy AS has a higher susceptibility to cracking compared to alloy SW. This can be attributed to the presence of MnS inclusions in alloy AS, which accelerate the crack initiation in this material as observed from the four-point bend test studies on this material.

Alloy SW on the other hand has a lower Mn content and negligible S content which suppresses the formation of MnS inclusions in this material.

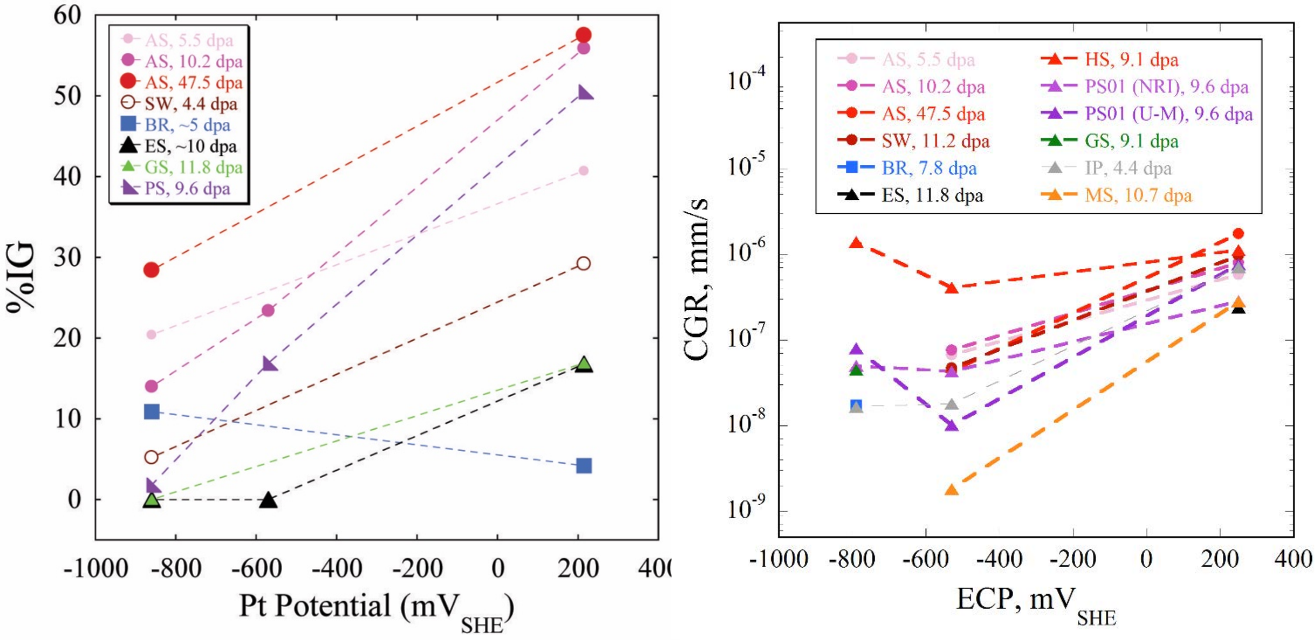

(a) (b)

Figure 4-1: Comparison of a) %IG in CERT tests [14], and b) CGR versus ECP for alloys tested in multiple environmental conditions [14].

From CERT tests, the %IG observed on the fracture surface can be used to quantify the degree of susceptibility to IASCC. However, this parameter includes the contribution from both crack initiation and crack growth. To isolate these two different phenomena, crack morphology provides useful insight. Figure 4-2 shows an example of crack morphology for the 10.2 dpa AS alloy in these three environmental conditions. There is a significant difference in the crack morphology between the environmental conditions. Both NWC and HWC showed limited number of crack nucleation sites, with the crack nucleation being limited to one nucleation site while the primary water conditions showed a large number of crack nucleation sites irrespective of the material condition (dose, cold-work or solute addition). The lower % IG in the PWR environment can be attributed to a lower crack propagation rate in this environment. Even though a large number of cracks are being nucleated on the specimen surface, the environment allows for limited crack propagation and thus the overall susceptibility of the material to IASCC in this environment is low. On the other hand, the crack initiation is limited to one nucleation site in NWC and HWC environments. Subsequently, the crack propagates at a fast rate, resulting in failure of the material in these two environments. Compared to the NWC environment, the lower ECP in HWC environment resulted in a lower crack propagation rate. Thus, the material shows a lower fraction of intergranular failure in this environment compared to NWC environment.

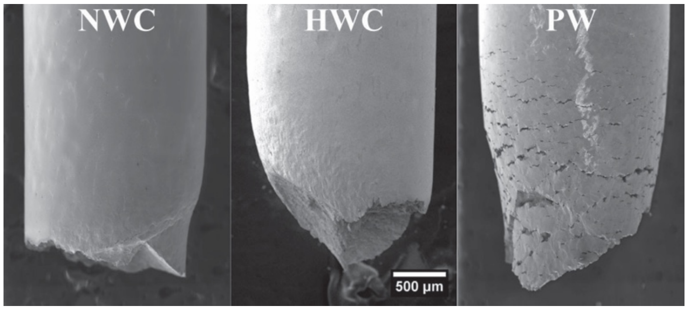

Figure 4-2: Secondary cracking on the gage surface of the 10.2 dpa alloy AS tensile bars tested in NWC, HWC, and PW conditions.

4.1.2 Crack Growth Rate

304L from Barseback 1 BWR

It has been shown in Figure 4-1b [14] decreasing the corrosion potential by switching from NWC to HWC could suppress the CGR of non-irradiated stainless steel significantly (up to two orders of magnitude). The results on neutron-irradiated stainless steel from Jenssen also shows that there is a significant mitigating effect of HWC environment on CGR when the dose is below 7 dpa [1]. One of the samples in ref. [1] was made from the same bulk material as the samples used in this work. The results from that sample can be directly used for comparison. The results of that sample along with the results from this work are plotted in Figure 4-3. The invalid data points from RCT2 were framed in dashed squares. The CGRs of RCT-2 (as irradiated) are very consistent with those of the as irradiated sample from Jenssen in NWC at similar K values.

From Figure 4-3, it can be seen that the HWC environment still has significant effect in mitigating CGR on all the samples, irrespective of the post annealing treatment. The CGRs of RCT-2 (as-irradiated) and RCT-1 (annealed at 500^{o}C for 1 hr) were decreased by a factor of 4~7 and 16 respectively; and those of RCT-4 (annealed at 550^{o}C for 5 hr) and RCT-3 (annealed at 550^{o}C for 20 hr) were reduced by factors in the range 55-100, and 39 respectively in HWC. The mitigating effect of HWC increases after the post irradiation annealing treatment, indicating that the HWC effect may be dependent on the inherent SCC susceptibility of material. Consistent with the observations from this program, the results from ref. [1] also showed that there is little mitigating effect of HWC on samples with doses above 7 dpa where SCC susceptibility is high. Therefore, it is likely that HWC has a smaller mitigating effect on material with higher SCC susceptibility.

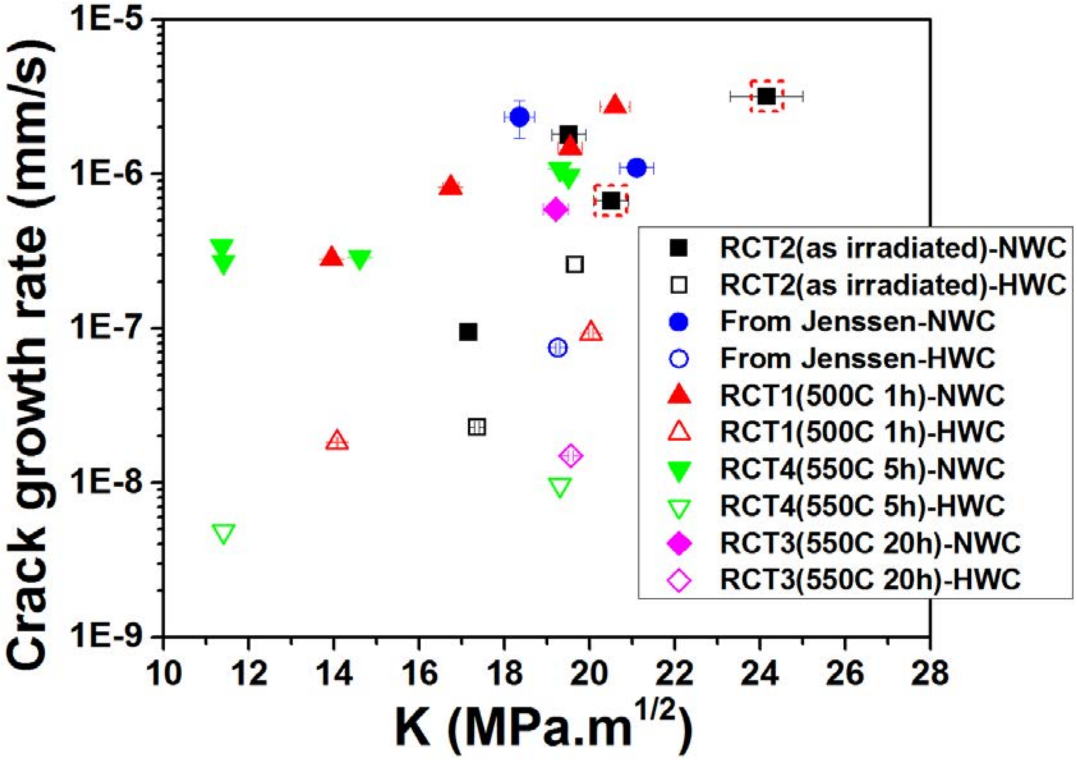

Figure 4-3: CGRs of 304 L SS irradiated to 5.9 dpa in 288 °C water. The red-boxed data points are not considered to be a valid, based on the applied K criteria.

4.2 *Post-irradiation Annealing*

4.2.1 Crack Initiation

Post-irradiation annealing (PIA) treatments have been reported to result in improvement in the cracking behavior of austenitic stainless steels in both proton and neutron irradiated conditions [18, 29-40]. However, due to a multitude of variables involved including the alloy compositions in different studies, a clear understanding of the role of post irradiation annealing is still developing. All of these previous studies focus on the role of PIA on different properties (mechanical and microstructural) and its correlation with the cracking behavior observed in the environment using constant extension rate testing in simulated reactor environment.

With regard to the cracking susceptibility of the material in different annealing conditions, most of the cracking data reported in the literature has been based on the % intergranular fracture observed on the fracture surface. As such, for the sake of comparing to previous PIA results, this value will be utilized for comparing the reduction in IASCC susceptibility after PIA in this study . Following CERT straining to failure, the fracture and gage surfaces were fully examined by SEM; where the separate fracture regions were quantified to determine %IG, %TG, % mixed IG/TG, and % ductile failure, as reported in Table 3-13 and Figure 3-17.

The as-irradiated tensile specimen was observed to have the highest degree of IASCC susceptibility, with 48.4% of the final fracture area consisting a pure intergranular fracture, 28.6% of the region showed a mixed intergranular-transgranular fracture, while only 3.6% showed a pure transgranular failure, and the remaining 19.4% was the final ductile failure of the specimen. As shown in Figure 4-4, the value of 48.4% IG failure is moderate as compared to other PIA studies on 304 stainless steel in the literature [29, 31, 38]. Only one case reported in the literature had a lower %IG fracture of the as-irradiated material: a 304 steel at ~4 dpa [29]. Most other studied alloys had both a higher degree of irradiation damage and %IG fracture in the as-irradiated condition.

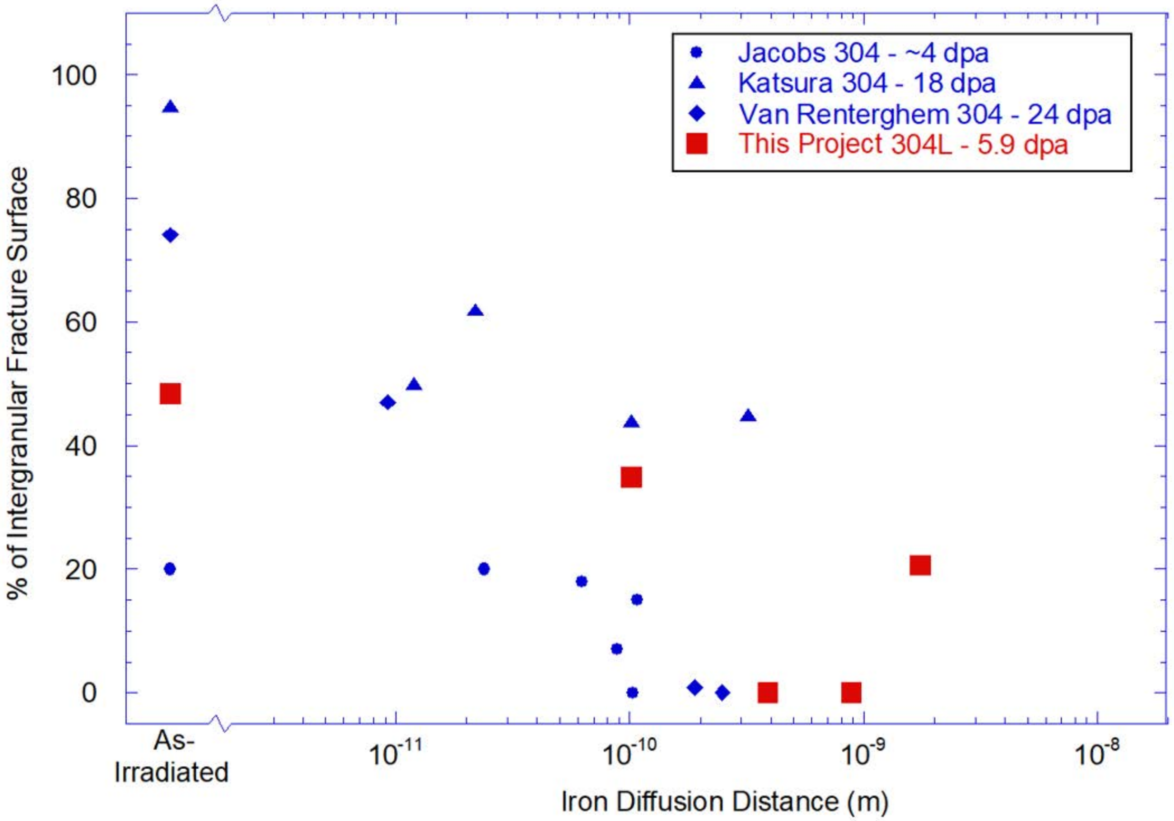

Figure 4-4: Comparison of the measured intergranular fracture area as a percentage of the final fracture area from this project and several neutron-irradiated PIA specimens in the literature.

Annealing at 500°C: 1hr and 550°C:20 hr resulted in a lower percentage of pure intergranular fracture of 34.9% and 20.6% respectively. The degree of mixed mode fracture seemed to vary between the studied conditions while the degree of transgranular fracture was significantly enhanced to ~30% of the fracture area for both examined conditions. It is worth noting that characterizing IASCC susceptibility by %IG produces a higher susceptibility for the 550°C: 20 hr condition than expected based on other results. This tensile specimen initiated two cracks that grew from opposite sides of the tensile specimen slightly off plane from one another. After both cracks progressed through roughly 50% of the cross section, the specimen failed in shear between the two separate crack planes. As such, the final fracture cross section displays two independent crack fronts, which might account for the higher percentage of pure intergranular fracture. Annealing at 550°C for both 1hr and 5hr caused a full mitigation of IASCC susceptibility and exhibited a 100% ductile fracture.

Figure 4-4, shows the change in % of intergranular failure with varying PIA treatments for both this material and several similar alloys reported in the literature [29, 31, 38]. By comparison, many of the other alloys studied in literature display a faster rate of removal of IASCC susceptibility than the 304L alloy studied in this project even taking into account all four PIA conditions. The exact reason for this behavior is not known. A possible exception to this is a 304 alloy at 18 dpa studied by Katsura *et al.* [31]. This material displayed a much higher as-irradiated susceptibility (95% IG), but was seen to stabilize at ~45% intergranular fracture after annealing 500°C for 10 hours. However, due to the lack of extensive annealing treatments, the behavior of this material after annealing at higher temperatures is unknown. With respect to the PIA results on the present program, with the exception of the 550/20 the mitigation of IASCC by PIA effectively follows a similar trend to that reported for the majority of cases in the literature.

4.2.2 Crack Growth Rate

Figure 4-3 shows that the CGRs of the as-irradiated sample (RCT-2) are comparable with those from ref. [1]. The CGR in NWC near K value of 19 $\mathrm{MPa\cdot m^{1/2}}$ decreases slightly with the severity of the annealing treatment (in the order of RCT-2, RCT-1, RCT-4 and RCT-3). The mitigation factors for crack growth in NWC (ratio of CGRs for growth in as-irradiated and in annealed samples) are 1.2, 1.6 and 3 for annealing at 500 °C for 1 h, 550 °C for 5 and 20 h respectively. Such mitigation factors are marginal considering the inherent fluctuation in CGR test. The mitigation factors in for crack growth in HWC are larger, 3, 27 and 17 respectively. The constant extension rate tensile test results also showed that the post-irradiation annealing at 550 °C for 1 and 5 h completely mitigated the IASCC susceptibility while annealing at 550 °C for 20 h significantly reduced the percentage of intergranular fracture area. It seems that the annealing treatments have larger mitigating effects on crack initiation than on crack growth in NWC.

If the IASCC susceptibility of irradiated material is controlled by the irradiated microstructure, then the reduction in IASCC susceptibility should be related to the recovery of the microstructure, i.e. to the removal of dislocation loops, solute clusters and irradiation induced segregations. From Table 3-2 and Figure 3-4, post-irradiation annealing at 550 °C for 20 h significantly reduces the number density of dislocation loops (only 0.4% remains) while the loop size increases. Table 3-3 and 3-4 show that the densities of Ni-Si and Al-Cu clusters decrease while the diameters increase after annealing treatments. . The volume fraction of Ni-Si cluster changes slightly while that of Al-Cu cluster decreases from 0.035% to 0.016% after annealing at 550 °C for 20 h. The element compositions of the clusters change as well due to the difference in diffusivity of element. The Ni-Si ratio increases on annealing as Si diffuses faster than Ni. In a similar manner the Al-Cu ratio decreases due to the faster diffusion of Al.

As to the element segregation, Table 3-5 and Figure 3-10 show that the depletion of Cr and enrichment of Ni and Si at the grain boundary drop significantly, indicating that grain boundary segregation is mostly recovered. It has been reported that elevated Si concentration can result in high crack growth rates and insensitivity to change in corrosion potential [41]. From Table 3-5, the grain boundary Si dropped from 2.48 wt.% to 0.65% and 0.43% after 5 and 20 h at 550 °C, which could explain the increasing mitigation factor by switching to HWC, as shown in Table 4-

1. The highest grain boundary Si concentration of the as-irradiated sample is only 1.2 wt.% from Jenssen's work [1], which is consistent with the fact that the mitigation factor is much higher than that of RCT-2 (Table 4-1).

4.3 *Irradiated Microstructure*

In general, the irradiated microstructure is expected to influence the irradiation hardening, and hence possibly IASCC susceptibility, as a function of the defect density and average size. In this section, we consider accounting for the hardness of the various PIA conditions using the microstructure and the dispersed barrier hardening model.

The relationship between the measured irradiation hardening and the evolution of the irradiated microstructure has been often studied for many decades [42-45]. Most often the irradiated microstructure exists as a distribution of barriers that impede dislocation motion, and can be measured through the dispersed barrier hardening model as given by:

$$\Delta\sigma_{y,i} = \alpha_i M\mu b\sqrt{N_i d_i}\ , \tag{4.1}$$

where $\Delta\sigma_{y,i}$ represents the increase in the yield stress arising from obstacles of density, N_i, and diameter, d_i, and strengthing factor of α_i. M, μ, and b represent the Taylor factor, shear modulus and Burgers vector of the material, respectively. The strengthening factor ranges between 0 and 1, where a value of 1 represents a perfectly hard barrier around which a dislocation must bow.

As multiple irradiation defect types exist in an irradiated material, a method is needed to measure the superposition of multiple defects of varying strengths, sizes, and densities. The most common superposition methods in literature [44] include the linear sum (LS) and root-square-sum (RSS) as shown in Equations 4.2 and 4.3, respectively.

$$\Delta\sigma_{y,LS} = \textstyle\sum_i \Delta\sigma_{y,i} \tag{4.2}$$

$$\Delta\sigma_{y,RSS} = \sqrt{\textstyle\sum_i \left(\Delta\sigma_{y,i}\right)^2} \tag{4.3}$$

The LS method is most often used when the various obstacle types are at dissimilar strengths or if they influence dislocation movement at differing length scales. In these cases, the defects do not influence one another, thus the overall strengthening is simply a sum of each of the individual barrier strengths. In the case of barriers with similar strengths, the RSS method is preferred. When the barriers are of similar strengths then a moving dislocation is unable to distinguish between the two defect types, thus the sum of the areal densities of each defect type must be combined to account for the effective defect spacing [45].

The respective strengthening factors of dislocation loops (α_L), Ni-Si (α_{Ni}), and Al-Cu (α_{Al}) solute clusters were calculated using both the LS and RSS methods given by:

$$\Delta\sigma_{y,LS} = \alpha_L M\mu b\sqrt{N_L d_L} + \alpha_{Ni} M\mu b\sqrt{N_{Ni} d_{Ni}} + \alpha_{Al} M\mu b\sqrt{N_{Al} d_{Al}}\quad , \tag{4.4}$$

$$\left(\Delta\sigma_{y,RSS}\right)^2 = (\alpha_L)^2\left(M\mu b\sqrt{N_L d_L}\right)^2 + (\alpha_{Ni})^2\left(M\mu b\sqrt{N_{Ni} d_{Ni}}\right)^2 + (\alpha_{Al})^2\left(M\mu b\sqrt{N_{Al} d_{Al}}\right)^2. \tag{4.5}$$

For the as-irradiated and PIA conditions of 500°C:1hr, 550°C: 1 and 20 hr, $\Delta\sigma_y$ was calculated as the difference between the measured yield stress and that of the unirradiated 304L condition (211.5

MPa). N and d are the respective number densities and sizes measured at each condition, while the constants are taken as $M = 3.06$ [44], $\mu = 76$ GPa, and $b = 0.255$ nm [33]. After inserting the known quantities into Equations 4.4 and 4.5, a least square fit with an intercept of zero was applied to calculate the unknown strengthening factors for each defect type, as presented in Table 4.1.

Using the linear sum method, the three defect types were found to have relatively similar strengths, though the strength of dislocation loops was calculated to be higher. The RMS method provided values similar to those using the LS, though the calculated strength of the dislocation loops and Ni-Si solute clusters were comparably increased, while the strength of the Al-Cu clusters was near negligible. Unfortunately, there is little existing literature in measuring the strength factors of solute clusters, though prior work by Toyama *et al.* [33] calculated an $\alpha_{Ni} = 0.11$ for solute clusters enriched in nickel and silicon. Furthermore, literature has suggested the strengthening factor of dislocation loops to typically be in the range of 0.2-0.5 [43], [45]. As such, it seems more likely that the RSS method is more applicable in predicting strengthening from the irradiated microstructure for the material studied in this project, as the calculated values are more like those typically found in related literature.

Table 4-1: Calculation of the strengthening factors (α) of the irradiated microstructure following annealing treatments, via both the linear sum and root-square-sum methods.

Calculation Method	Calculated Strengthening Factor (α)		
	Dislocation Loop (α_L)	Ni-Si Clusters (α_{Ni})	Al-Cu Clusters (α_{Al})
Linear Sum (LS)	0.127 ± 0.040	0.025 ± 0.069	0.060 ± 0.074
Root-Square-Sum (RSS)	0.190 ± 0.096	0.089 ± 0.076	0.016 ± 0.091

It is worth noting as well that these calculations assume that the strengthening factor for each defect type remains constant with annealing, and thus the strengthening effect is directly related to the changes in defect density and size. This is likely not the case for solute clusters, as the strengthening for these defects likely arises more from the solute concentrations, thus during annealing although the cluster itself expands in size the solute concentration becomes less. As such it is likely that while an as-irradiated solute cluster may be of a smaller size, it is likely more difficult for moving dislocation to cut through as compared to the larger solute clusters observed after annealing at 550°C: 20 hr, due to the difference in solute concentration. This effect is planned to be investigated in a later, more detailed study.

In general, the irradiated microstructure is expected to influence the irradiation hardening, and hence possibly the IASCC susceptibility, as a function of the densities and average sizes of the various defects and features present in the microstructure. Based on the theoretical hardening in a matrix, these factors can be compared as a function of $\sqrt{Nd}$, where N is the number density of the irradiation defect and d is the average defect size [44]. Figure 4-5 shows the IASCC susceptibility, as measured by the % IG fracture, along with $\sqrt{Nd}$ of the three observed microstructural defects. In Figure 4-5 the dislocation loops, Ni-Si and Al-Cu solute clusters, displayed in orange and the coincident changes in mechanical properties as represented by the changes hardness, yield strength and the reciprocal of ductility at fracture. To facilitate discussion of the effects of annealing, in

Figure 4-5 the changes are plotted against the annealing conditions, represented by the iron diffusion distance calculated for the temperatures and times of the anneals.

Except for the Al-Cu clusters at 550ºC: 5hr, the theoretical impact of the microstructure generally decreases with IASCC susceptibility. However, while the 550ºC: 1 and 5hr conditions have a higher impact from the residual microstructure as compared to the 550ºC: 20hr condition, they displayed a full mitigation of IASCC susceptibility. Previous PIA literature has indicated a clear relation between IASCC initiation susceptibility and the irradiation hardening or yield stress [18], likely in relation to the reduction of the irradiated microstructure. In general, this study has also indicated a general trend between the irradiation hardness and yield stress and the measured IASCC susceptibility, as shown in Figure 4-5, where the mechanical properties are displayed in blue. Once again, this trend is broken by the PIA treatment of 550ºC: 20hr, whereas 550ºC: 1 and 5hr conditions have a higher irradiation hardening, but a reduced susceptibility. It is important to note that the %IG fracture area, is not the only representation of the IASCC susceptibility, but the overall ductility is also relevant. Figure 4-5 displays a comparison between the intergranular fracture and the ductility, as measured by 1/ε, where a good agreement is observed between an increased ductility and decreased IASCC susceptibility. Though once again the 550ºC: 20 hr condition shows a rather high ductility while also having an increased IASCC susceptibility.

The decrease in both the depletion of chromium and enrichment of nickel and silicon grain boundary segregation with annealing is also displayed in Figure 4-5, where the RIS data is plotted in green. With an increase of annealing time and temperature the segregation is increasingly reduced, but the lack of a complete data set makes a full comparison to the IASCC susceptibility difficult.

Overall, it was observed that PIA treatments are successful in reducing the number density of defects in the irradiated microstructure, irradiation hardening, and IASCC susceptibility of 304L stainless steel BWR-irradiated to a dose of 5.9 dpa. While the number density of defects in the irradiated microstructure, radiation-induced segregation, and hardening were all incrementally decreased with increasing annealing time and temperature, IASCC susceptibility was not concomitantly reduced. The 1 h and 5 h anneals at 550°C fully mitigated the initiation of IASCC. However, IGSCC susceptibility apparently returned after the 550°C:20 h anneal. Based on this data, it is suspected that the 550ºC: 20 hr tensile specimen examined is an outlying result as compared to the remaining data. However, there is no valid reason to remove the specimens from the dataset. Instead, further examination is planned to try to understand the cause of the re-emergence of IGSCC in this sample.

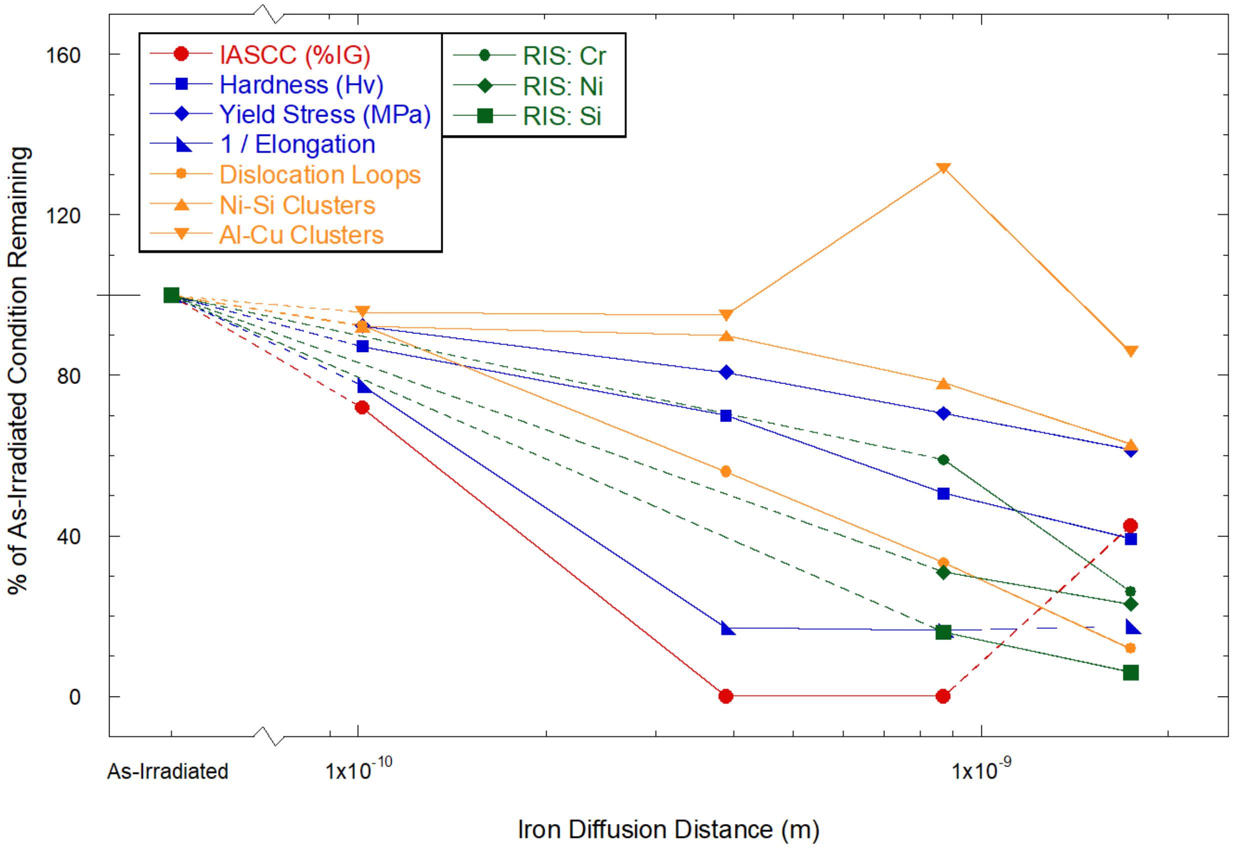

Figure 4-5: Comparison of the IASCC susceptibility to the mechanical properties and irradiated microstructure as a percentage of the as-irradiated condition.

4.4 *Dislocation Channeling in IASCC*

Localized deformation (dislocation channeling) plays a significant role in determining the cracking susceptibility of the material. A direct correlation has been observed between localized deformation and the cracking susceptibility of the material in environment. In this study, an attempt has been made to study the effect of PIA on localized deformation and to correlate it with the observed cracking behavior.

To study the role of channeling in crack initiation behavior, four-point bend tests were carried out on neutron irradiated specimens of alloy AS, ES and KS. The commercial purity alloy AS showed very high susceptibility to IASCC crack initiation in all three damage conditions (5.5 dpa, 10.2 dpa and 47.5 dpa). In all three conditions the cracks were found to initiate at very low stresses (low fractions of the yield stress) as shown in Figure 3-48. Crack initiation was found to always be preceded by the activation of dislocation channels in the material. Upon further straining, the cracks were found to initiate at dislocation channel-grain boundary intersections. An important observation was that with an increase in the damage level in the material, the stress required to initiate a channel and initiate a crack was reduced as shown in Figure 4-6.

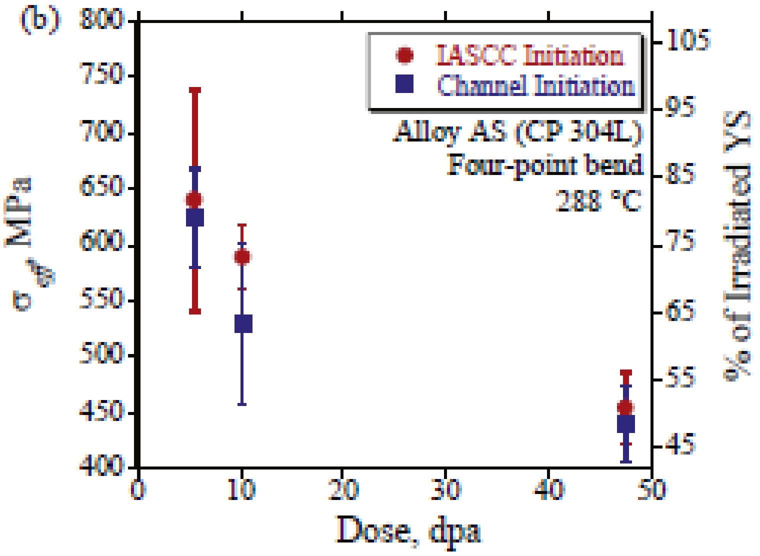

Figure 4-6: Average stress required to cause formation of dislocation channeling and crack initiation in commercial purity austenitic stainless steels as a function of damage level [46].

Furthermore, the majority of the cracking in alloy AS was found to occur at the intersection of dislocation channels with MnS inclusions. MnS inclusions were found to undergo dissolution in the environment resulting in the formation of a cap consisting of the dissolution product. This results in the formation of an aggressive environment below the cap. This environment combined with the intersection of a dislocation channel with the inclusion (thereby causing stress concentration) is believed to be the reason for cracks to initiate at these sites. Similar cracking behavior at MnS inclusions was previously observed by Jiao et al. [47] after proton irradiation of the same heat of material (Alloy AS). They attributed the crack initiation at the MnS inclusions to the cracking of the inclusion to the stress accumulation caused by dislocation channeling. The mechanism of cracking then is that dislocation channels impinge on MnS particles, which then crack MnS particles, possibly preparing them for easier dissolution. Dissolved MnS product provides an aggressive environment for crack initiation/propagation.

Comparison also needs to be made for the difference between the cracking behavior of three different alloy systems: AS (CP304L), ES (HP 304 L), and KS (HP + Ni). The difference between the three alloys lies in the composition. Alloy ES and KS show higher resistance to crack initiation compared to alloy AS, as shown by the higher stresses required to cause cracking in these alloys. While alloy AS failed predominantly at the dislocation channel-inclusion intersection, such behavior was not observed for alloys ES and KS. Both of these alloys failed at the intersection of a dislocation channel with a grain boundary. Furthermore, the higher stress required to cause crack initiation shows that the alloys needed to be deformed to higher strain levels. This could be due to the lack of a microstructural-based stress riser like an inclusion, or perhaps, to the higher stacking fault energy (SFE) for these materials. Higher stacking fault energy (SFE) materials have been found to be more resistant to localized deformation due to easier cross-slip, thus requiring a higher strain to cause crack initiation [48]. Among the alloys ES and KS, alloy KS was found to be most resistant to crack initiation which correlates with the higher stacking fault energy due to the additional nickel content.

For the 304L alloy irradiated in Barseback 1, the change in dislocation channel density for different annealing conditions and at different strain levels is shown in Figure 3-18. The dislocation channel density was unaffected by the annealing at 500^{o}C:1hr and 550^{o}C:1hr, but was reduced following the 550^{o}C:5 hr annealing, and significantly reduced after PIA at 550^{o}C:20 hr. This reduction in the channel density can be attributed to the removal of irradiation induced defects during the annealing treatment, suggesting that the density of dislocation channels is primarily affected by the irradiation-induced defect densities, which agrees with previous work by Jiao *et al.* [6]. In that work, the dislocation loop density was the primary contributor to the development of localized deformation. However, the dislocation channeling behavior for the tensile bar subjected to 550 °C:1hr annealing treatment shows high channel density even though a significant reduction in dislocation loop density was observed. Furthermore, a high recovery of ductility was observed in this condition, indicating the removal of defects during the annealing treatment. As shown in Figures 3-18 and 3-19, the amount of localized deformation does not follow the annealing behavior, indicating that it is not just the channel density that is important, but perhaps other factors such as the stress at the channel-grain boundary intersection.

Localized deformation has been found to greatly influence the crack initiation behavior in austenitic stainless steels, particularly at sites where a discontinuous dislocation channel interacts with the grain boundary. [8,9]. With regard to the deformation behavior in materials given different annealing conditions, it is believed that cracking at the channel-grain boundary intersection requires a threshold stress be exceeded. Due to the reduction in the defect density during annealing treatments, the extent of localized deformation taking place in the material is reduced significantly for more severe annealing treatments. For example, in the case of the as-irradiated state and lower annealing treatments, i.e. 500^{o}C:1hr and 550^{o}C:1hr, a significant portion of the plastic deformation could only be through the formation of dislocation channels, hence the higher density. While for the 550^{o}C:20hr condition most of the plastic strain could be homogeneously accommodated, hence the much lower observed channel density. However, it can be speculated that even for the 500^{o}C:1hr and 550^{o}C:1hr conditions a certain portion of the bulk plastic strain may have been homogeneously distributed. The relative amount of strain carried by the dislocation channels, may reflect on the resultant IASCC susceptibility.

5 CONCLUSION

Crack initiation was studied by both CERT and four-point bend tests. CERT studies on neutron irradiated stainless steel alloys showed that the increase in the corrosion potential of the environment results in an increase in the cracking susceptibility of the alloy. At high potentials, the cracking susceptibility was determined by crack propagation since very few cracks nucleate and the nucleated crack rapidly grows to cause failure. At low potentials, cracking was predominantly controlled by crack initiation resulting in high crack density on the surface of the specimen. Indeed, the apparent relative susceptibility may depend on the comparison used. When measured by %IG on the fracture surface, samples in NWC would be considered to have greater susceptibility. But when measured by surface crack density, samples in PWR PW would be considered to be more susceptible.

Four-point bend tests were conducted to correlate the crack initiation behavior with dislocation channeling. The advantage of these tests is that the growth of cracks was suppressed due to the increasingly compressive stress field normal to the surface. These tests were highly successful in catching crack initiation and linking it to the microstructure and dislocation channels. Depending on the dpa, dislocation channels form at stresses as low as 40% of the bulk yield stress. Cracks always nucleated at dislocation channel-grain boundary intersections either with the formation of the channel or after it. MnS inclusion on the grain boundary were often the site of crack nucleation and their dissolution in NWC is likely a key factor in producing an environment that is conducive to cracking. It was also found that higher dpa resulted in a lower stress to both initiate dislocation channels and cracks.

Post irradiation annealing was found to mitigate the crack initiation susceptibility in 304L irradiated in the Barseback 1 BWR. With one exception, annealing longer time and/or temperature resulted in a decrease in SCC susceptibility. All measures of IGSCC susceptibility (max stress, uniform strain, total strain, %IG) changed monotonically with heat treatment severity. The exception was an increase in IGSCC in the most severely annealed sample, which is not explainable with the resulting microstructure. Close inspection of the microstructure showed that all features (dislocation loops, clusters, RIS) changed smoothly and monotonically with respect to the dgree of annealing and comparison of the microstructures at annealing treatments that bracketed the onset of cracking did not provide sufficient differentiation to allow identification of the feature or features responsible for cracking. Nevertheless, results indicate that an annealing treatment of 550°C for greater than 1 hr was sufficient to eliminate intergranular cracking in BWR NWC.

The crack growth rates of post-irradiation and annealed 304L stainless steel samples (as-irradiated (5.9 dpa), irradiated + annealed (500 ^{o}C:1 h), irradiated + annealed (550 ^{o}C:5 h) and irradiated + annealed (550 ^{o}C:20 h)) have been measured in NWC and HWC environments. The results show that HWC can significantly mitigate the SCC propagation of all the samples. The mitigating effect of HWC increases after the annealing treatment, indicating that it is dependent on the inherent

SCC susceptibility of material. The post-irradiation treatment has limited mitigating effect on the SCC propagation of this material in NWC with a larger effect in HWC, as well as in PWR primary water. The environmental dependence of mitigating effect may be related to the grain boundary Si concentration. It seems that the annealing treatments have larger mitigating effects on crack initiation than on crack growth in NWC. The reduced SCC susceptibility of the annealed sample is consistent with the recovery in the irradiated microstructure (dislocation loop, solute cluster and grain boundary segregation). However, the key microstructural changes that would determine the differences in behavior could not be specifically identified to date.

6 REFERENCES

1. BWRVIP-221: BWR Vessels and Internals Project, Crack Growth in High Fluence BWR Materials – Phase 1: Crack Growth Rate Testing of Types 304L and 316L at Doses Ranging from 3.5 to 13 dpa. EPRI, Palo Alto, CA, 2009. 1019079.
2. N. Soneda, K. Nishida, A. Nomoto, K. Dohi, “Characterization of Solute Atom Distribution in Grain Interior of Neutron-irradiated 304L and 304 Stainless Steels,” presented at TMS 2011, San Diego, CA, 2011.
3. A. Jenssen, Machining and Shipment of Specimens from Heat SW- Documentation of Fabricated Specimens. Technical Note: N-13/210. Studsvik Nuclear AB.
4. J.P. Massoud, P. Dubuisson, P. Scott, V.K. Chamardine, CIR II Program: Description of the Boris 6 and 7 Experiments in the BOR-60 Fast Breeder Reactor. EPRI, Palo Alto, CA, 2005. 1011787.
5. B.W. Arey, D.G. Atteridge, S.M. Bruemmer, Production of Tailored Alloys to Isolate Metallurgical Variables Promoting IASCC, EPRI, Palo Alto, CA, 2007.
6. Z. Jiao, G. Was, “The Role of Irradiated Microstructure in The Localized Deformation of Austenitic Stainless Steels,” J. Nucl. Mater., vol. 407, no. 1, pp. 34–43, 2010.
7. M. McMurtrey, G. Was, L. Patrick, and D. Farkas, “Relationship between Localized Strain and Irradiation Assisted Stress Corrosion Cracking in an Austenitic Alloy,” Mater. Sci. Eng. A, vol. 528, no. 10–11, pp. 3730–3740, 2011.
8. M. McMurtrey, G. Was, B. Cui, I. Robertson, L. Smith, and D. Farkas, “Strain Localization at Dislocation Channel-Grain Boundary Intersections in Irradiated Stainless Steel,” Int. J. Plast., vol. 56, pp. 219–231, 2014.
9. M. McMurtrey and G. Was, “Quantification of Stress and Strain States at Dislocation Channel-Grain Boundary Intersections and their Relation to IASCC in Austenitic Steels,” in Proceedings of 16th International Conference on Environmental Degradation of Materials in Nuclear Power Systems-Water Reactors, NACE International, Houston, TX. 2014.
10. J.T. Busby, G.S. Was, The Use of Proton Irradiation to Determine IASCC Mechanisms in Light Water Reactors: Phase 2: Commercial Alloys, EPRI, Palo Alto, CA, 2005. 1009898.
11. J.T. Busby, G.S. Was, The Use of Proton Irradiation to Determine IASCC Mechanisms in Light Water Reactors: Solute Addition Alloys, EPRI, Palo Alto, CA, 2003, 1007440.
12. J.C. Heap, Thermal Stresses in Concentrically Heated Hollow Cylinders, Argonne National Laboratory, Argonne, IL, 1960.
13. T.S. Byun, N. Hashimoto, “Strain Hardening and Long-range Internal Stress in The Localized Deformation of Irradiated Polycrystalline Metals”, J. Nucl. Mater., vol. 354 pp. 123-130, 2006
14. G.S. Was, Y. Ashida, K.J. Stephenson, A. Flick, P.L. Andresen, Identifying Mechanisms and Mitigation Strategies for Irradiation Assisted Stress Corrosion Cracking of Austenitic Steels in LWR Core Components, EPRI, Palo Alto, CA, 2014. 3002003105.
15. ASTM Standard E399-09, “Standard Test Method for Linear-Elastic Plane-Strain Fracture Toughness K_{Ic} of Metallic Materials”, ASTM International, Philadelphia, PA. 2009.

16. G.S. Was, K.J Stephenson, “Program on Technology Innovation: Establishment on the Capability to Determine IASCC Initiation from Four-point Bend Tests Conducted in a Boiling Water Reactor Normal Water Chemistry Environment”, EPRI, Palo Alto, CA. 2016. 3002007972.
17. M.D. McMurtrey, “The Relation Between Irradiation Assisted Stress Corrosion Cracking and Dislocation Channeling: The Role of Slip Interaction at the Grain Boundary”, Ph.D Thesis, University of Michigan, 2014.
18. K. Fukuya, M. Nakano, K. Fujii, T. Torimaru, Y. Kitsunai, “Separation of Microstructural and Microchemical Effects in Irradiation Assisted Stress Corrosion Cracking using Post-irradiation Annealing,” J. Nucl. Sci. Technol., vol. 41, no. 12, pp. 1218–1227, 2004.
19. D.J. Edwards, A. Schemer-Kohrn, S. Bruemmer, “Characterization of Neutron-Irradiated 300-Series Stainless Steels”. EPRI, Palo Alto, CA. 2006. 1009896.
20. D.J. Edwards, S.M. Bruemmer, “Characterization of CIR II Irradiated Stainless Steels”, EPRI, Palo Alto, CA, 2008. EP-P19021/C9406.
21. J.T. Busby, M.C. Hash, G.S. Was, “The Relationship between Hardness and Yield Stress in Irradiated Austenitic and Ferritic Steels,” J. Nucl. Mater. vol. 336, pp. 267-278. 2005.
22. M. Gussev, K. Field, J. Busby, “Deformation localization and dislocation channel dynamics in neutron-irradiated austenitic stainless steels,” J. Nucl. Mater., vol. 460, pp. 139–152, 2015.
23. D. Edwards and B. Singh, “Evolution of cleared channels in neutron-irradiated pure copper as a function of tensile strain,” J. Nucl. Mater., vol. 329–333, pp. 1072–1077, 2004.
24. K. Stephenson, G. Was, “Development of a Novel SCC Test for Isolating Crack Initiation in Neutron Irradiated Stainless Steel,” in 17th International Conference on Environmental Degradation, Canadian Nuclear Society, Toronto, Ontario, 2015.
25. T.S. Byun, N. Hashimoto, “Strain Hardening and Long-range Internal Stress in The Localized Deformation of Irradiated Polycrystalline Metals”, J. Nucl. Mater. vol. 354 pp.123. 2006.
26. K.J. Stephenson, G.S. Was, “Crack Initiation Behavior of Neutron Irradiated Model and Commercial Stainless Steels in High Temperature Water,” J. Nucl. Mater. vol. 444, pp. 331. 2014.
27. S. Fyfitch, S. Davidsaver, K. Amberge, “Irradiation-Assisted Stress Corrosion Cracking Initiation Screening Criteria for Stainless Steels in PWR Systems,” in Proceedings of 18th International Conference on Environmental Degradation of Materials in Nuclear Power Systems, TMS, Pittsburgh, PA. 2018.
28. P.L. Andresen, M.M. Morra, “IGSCC of non-sensitized stainless steels in high temperature water”. J. Nucl. Mater., vol. 383: pp. 97-111. 2008.
29. A.J. Jacobs, G.P. Wozadlo, G.M. Gordon, “Low-Temperature Annealing: A Process to Mitigate Irradiation-Assisted Stress Corrosion Cracking”, Corrosion vol. 51 pp. 731-737. NACE International. Houston, TX. 1995.
30. K. Asano, R. Katsura, M. Kodama, S. Nishimura, K. Fukuya, K. Nakata; “Post Irradiation Annealing effects on hardness and intergranular corrosion in Type 304 stainless steels”; in 7th International Symposium on Environmental Degradation of Materials in Nuclear Power Systems-Water Reactors, pp.1033-1042. NACE International, Houston TX. 1995.
31. R. Katsura, Y. Ishiyama, M. Yokota, T. Kato, K. Nakata, K. Fukuya, H. Sakamoto, K. Asano, “Post irradiation Annealing effects on Austenitic stainless steels in IASCC”, Corrosion 98, NACE International, Houston TX. 1998.

32. A.J. Jacobs, S. Dumbill, “Effects of Low Temperature Annealing on the microstructure and grain boundary chemistry of irradiated type 304 SS and correlations with IASCC Resistance”, in 7th International Symposium on Environmental Degradation of Materials in Nuclear Power Systems- Water Reactors, pp. 1021-1031. NACE International, Houston TX. 1995.
33. T. Toyama, Y. Nozawa, W. Van Renterghem, Y. Matsukawa, M. Hatakeyama, Y. Nagai, A. Al Mazouzi, S. Van Dyck, “Irradiation-induced Precipitates in a Neutron Irradiated 304 Stainless Steel Studied by Three-dimensional Atom Probe”, J. Nucl. Mater., vol. 418 pp. 62-68. 2011.
34. J.T. Busby, G.S. Was, E.A. Kenik, “Isolating the Effect of Radiation-induced Segregation in Irradiation-assisted Stress Corrosion Cracking of Austenitic Stainless Steels”, J. Nucl. Mater. vol. 302, pp. 20-40. 2002
35. J.T. Busby, M.M. Sowa, G.S. Was, E.P. Simonen “Post-irradiation Annealing of Small Defect Clusters”, Philos. Mag., vol. 85, pp. 609-617, 2005.
36. J.T. Busby, G.S. Was, E.A. Kenik “Post-Irradiation Annealing of Dislocation Microstructure and Radiation-Induced Segregation in Proton-Irradiated Stainless Steels,” in Mat. Res. Soc. Symp. Proc. Vol 540. Materials Research Society, Warrendale, PA, 1998.
37. W. Van Renterghem, M.J. Konstantinovic, M. Vankeerberghen; “Evolution of the Radiation-induced Defect Structure in 316 Type Stainless Steel after Post-irradiation Annealing” J. Nucl. Mater. vol. 452 pp. 158-165. 2014.
38. W. Van Renterghem, A. Al Mazouzi, S. Van Dyck; “Influence of Post Irradiation Annealing on the Mechanical Properties and Defect Structure of AISI 304 Steel”, J. Nucl. Mater. vol. 413 pp. 95-102. 2011
39. K.V. Tsay, O.P. Maksimkin, L.G. Turubarova, O.V. Rofman, F.A. Garner; “Microstructural Defect Evolution in Neutron–Irradiated 12Cr18Ni9Ti Stainless Steel during Subsequent Isochronous Annealing”, J. Nucl. Mater. vol. 439 pp.148-158. 2013.
40. J.T. Busby, M.M Sowa, G.S. Was, E.A. Kenik; “The Role of Fine Defect Clusters in Irradiation Assisted Stress Corrosion Cracking of Proton Irradiated 304 Stainless Steels,” J. ASTM Intl. vol.1 pp. 1-14. 2004.
41. P. Andresen, M. Morra, “Effects of Si on SCC of Irradiated and Unirradiated Stainless Steels and Nickel Alloys,” Proceedings of 12th International Conference on Environmental Degradation of Materials in Nuclear Power Systems, TMS, Pittsburgh, PA. 2005.
42. A. Seeger, “On the theory of radiation damage and radiation hardening,” in Proceedings of 2nd United Nations International Conference on the Peaceful Uses of Atomic Energy, Volume 6. vol. 48, no. 12, p. 250. United Nations, New York City, NY. 1958
43. G. Odette, G. Lucas, “Recent progress in understanding reactor pressure vessel steel embrittlement,” Radiat. Eff. Defects Solids, vol. 144, no. 1–4, pp. 189–231, 1998.
44. G. Was, “Fundamentals of Radiation Materials Science: Metals and Alloys”. Springer, Berlin, 2007.
45. F. Bergner, C. Pareige, M. Hernández-Mayoral, L. Malerba, and C. Heintze, “Application of a Three-feature Dispersed-barrier Hardening Model to Neutron-irradiated Fe – Cr Model Alloys,” J. Nucl. Mater., vol. 448, no. 1–3, pp. 96–102, 2014.
46. K. J. Stephenson, G.S. Was; “The Role of Dislocation Channeling in IASCC Initiation of Neutron Irradiated Stainless Steel”; J. Nucl. Mater. vol. 481 pp. 214-225. 2016
47. Z. Jiao, G.S. Was, J.T. Busby; “The Role of Localized Deformation in IASCC of Proton Irradiated Austenitic Stainless Steels”; Proceedings of 13th International Conference on

Environmental Degradation of Materials in Nuclear Power Systems, Canadian Nuclear Society, Toronto, Ontario, 2007.

48. Z. Jiao, G.S. Was; “Localized Deformation and IASCC Initiation in Austenitic Stainless Steels”; J. Nucl. Mater. Vol. 382 pp. 203-209. 2009.